The Dissertation Committee for Dominik Fabian Ebi certifies that this is the approved version of the following dissertation

Boundary Layer Flashback of Swirl Flames

Committee:

Noel T. Clemens, Supervisor

Ofodike A. Ezekoye

Laxminarayan Raja

Venkat Raman

Philip L. Varghese

Boundary Layer Flashback of Swirl Flames

by

Dominik Fabian Ebi, Dipl.-Ing.

DISSERTATION

Presented to the Faculty of the Graduate School of

The University of Texas at Austin

in Partial Fulfillment

of the Requirements

for the Degree of

DOCTOR OF PHILOSOPHY

The University of Texas at Austin

May 2016

Acknowledgements

First and foremost, I would like to thank my advisor Prof. Noel T. Clemens for providing me with the opportunity to work on this project. It has been an exceptional learning experience under his guidance and with his support. I am very grateful for the freedom he provided me with and the trust he put in my work. I am particularly thankful for the many opportunities he gave me to present my work at conferences, for introducing me to many others in the field and for supporting my involvement in side-projects beyond the research towards my Ph.D. I also want to thank Prof. Ofodike A. Ezekoye, Prof. Laxminarayan Raja, Prof. Venkat Raman and Prof. Philip L. Varghese for serving on my dissertation committee and for reviewing this work.

I have had the privilege to work alongside great fellow graduate students and post-docs. I want to thank my lab-mates Dr. Ross Burns, Dr. Chris Combs, Benton Greene, Heath Reising, Mohammed Saleem, Rakesh Ranjan, Tim Haller, Serdar Seckin and Dr. Okjoo Park and Dr. Leon Vanstone for making countless hours in dark labs and small cubicles enjoyable, for their support and the many great technical and non-technical discussions. I also want to thank George Sammy and Yasvanth Poondla, who contributed to this project as undergraduate researchers in our lab. I particularly want to thank Dr. Woutijn Baars, Dr. Jérôme Sicard and Andrés Cánchero for the many motivational conversations and for refreshing breaks.

I am grateful to the staff of the Department of Aerospace Engineering an Engineering Mechanics for their support. In particular, I want to thank Dr. Jeremy Jagodzinski for constantly working on keeping our lab a great place to work in, Donna Soward and Geetha Rajagopal for all their administrative support, Joe Pokluda and Pablo Cortez for their help in the machine and electronics shop, and Scott Messec for all the prompt IT support. The financial resources for this project have been provided by the U.S. Department of Energy under grant DEFC2611-FE0007107.

Last but not least, I want to thank my family for their love and endless support throughout the years. Danke für alles!

Boundary Layer Flashback of Swirl Flames

Dominik Fabian Ebi, Ph.D.

The University of Texas at Austin, 2016

Supervisor: Noel T. Clemens

Flame flashback in the boundary layer of swirling flows is investigated experimentally in a model swirl combustor. The model combustor features a mixing tube with an axial swirler and an attached center body. The findings provide novel insight into the mechanism facilitating boundary layer flashback of swirl flames. Turbulent, lean-premixed flames of methane and hydrogen are studied at atmospheric pressure and bulk flow velocities up to 5 m/s. Hydrogen contents range from 0% to 95% and equivalence ratios range from 0.4 to 1. The focus in the present work is on the upstream flame propagation inside the mixing tube. Stereoscopic particle image velocimetry (PIV) is applied at kilohertz-rate to provide the time-resolved, three-component velocity field. The flame front is detected simultaneously based on the acquired Mie scattering images. Simultaneous high-speed chemiluminescence imaging provides the overall flame shape and global propagation direction.

In addition to the planar measurements, a technique capable of detecting the instantaneous, time-resolved, 3D flame front topography is developed and applied successfully. Oil droplets, which vaporize in the preheat zone of the flame, serve as the

marker for the flame front. The droplets are illuminated with a laser and imaged from four different views followed by a tomographic reconstruction to obtain the volumetric particle field. The velocity field in the unburnt gas is measured using tomographic PIV. The resulting data include the simultaneous 3D flame front and volumetric velocity field at 5 kHz.

Flashback is found to occur in the form of large-scale, convex-shaped flame tongues, which swirl in the bulk flow direction as they propagate in the negative axial direction along the center body wall. Gas dilatation associated with the heat release imposes a blockage effect on the approach flow, which causes a 3D deflection of streamlines. As a result, a region of negative axial velocity forms along the leading side of the flame tongues, which facilitates flashback. These regions of negative axial velocity, already observed in previous studies, are shown to be the result of a predominantly swirling fluid motion as opposed to boundary layer separation or flow recirculation. The effect of hydrogen addition on flashback is investigated. Flashback occurs at significantly leaner conditions for hydrogen-rich flames, but the mechanism driving flashback is found to be independent of the hydrogen content for the conditions investigated in the present work. Quantitative differences in the flame-flow interaction between methane and hydrogen-rich flashbacks are discussed in detail.

Table of Contents

List of Tables

List of Figures

Chapter 1: Introduction

1.1 Motivation

The successful design of future lean-premixed and fuel-flexible gas turbine combustors requires an improved fundamental understanding of static and dynamic combustion instabilities [1,2]. Static instabilities refer to instances when the flame is not anchored at its intended location in the combustion chamber any more. Such instabilities include flame flashback and blowout. Dynamic instabilities due to the coupling between the heat release rate and acoustic pressure fluctuations can cause a mechanical failure of the combustor or trigger a static instability [3]. Currently employed combustors, which are designed to run on natural gas, are challenged by the desire to operate them with hydrogen blends, which differ substantially in their chemical, transport and thermal properties [1]. For instance, the gasification of coal, biomass or some other feedstock produces a synthetic gas (syngas) primarily containing hydrogen and carbon monoxide. Combusting syngas in an integrated gasification combined cycle (IGCC) offers advantages with regards to emission control and carbon dioxide capturing.

One of the key technical barriers in the development of combustors suited for operating on hydrogen-rich gas mixtures is preventing flame flashback. Flashback refers to the undesired upstream propagation of the flame from the combustion chamber into the premix section. The premix nozzles are not designed to withstand the heat load due to a flame. Sustained upstream flame propagation and flame anchoring in the preheat section

is hence a serious safety risk [2]. An example practical combustor design, which features five individual premix sections with a central fuel tube and a single axial swirler, is shown in Figure 1.1. The damage to the center body seen in Figure 1.1b was caused by flame flashback.

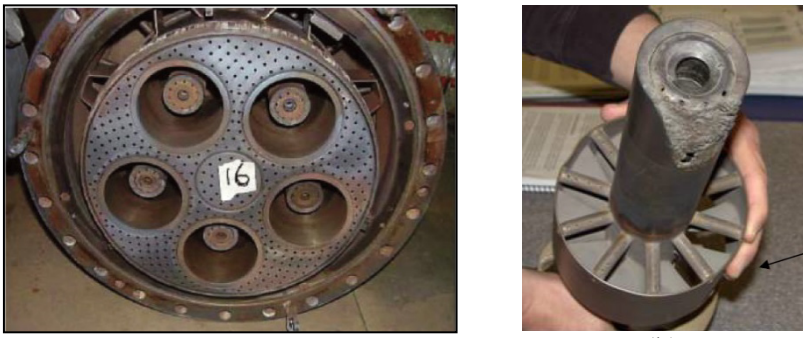

(a) (b)

Figure 1.1: Internals of a premix burner design. (a) Combustion chamber with five individual premix sections. (b) Damage to the central fuel tube due to flashback.

1.2 Review

The primary objective of the present work is to investigate the physics of boundary layer flashback of swirl flames. The current understanding of this phenomenon is reviewed in Section 1.2.1. High-speed laser diagnostic techniques are applied to study the upstream flame propagation during flashback. The employed planar techniques, which are described in Section 2.2, are well established and not reviewed separately here. As part of the present work, a technique to simultaneously reconstruct the three-dimensional topography of turbulent flames and measure the volumetric velocity field has been developed. Previous works on volumetric measurement techniques applied to reacting flows are reviewed in Section 1.2.2.

1.2.1 Flame flashback

A flame front propagates at a characteristic flame speed in a premixture of fuel and oxidizer. The traditional view has been that flashback occurs if the flame speed exceeds the flow velocity. In a laminar, quasi-1D flow the flame speed is governed by the thermo-chemical properties of the mixture [4]. In laminar 2D flows, the flame speed may be altered due to aerodynamic straining, flame curvature and flow/flame unsteadiness, collectively referred to as stretch effects [5]. For a positively stretched flame, the flame speed is increased for mixtures with Lewis number $Le << 1$ and if the deficient reactant has a higher diffusivity (such as in lean H_2-air mixtures).

In practical combustors, the flow field is turbulent. Turbulence wrinkles the flame front and increases the speed at which it propagates. For an ideal (statistically planar and freely propagating) turbulent flame front, a relationship for the turbulent flame speed s_T of the form

$$\frac{s_T}{s_L^0} = f\left(\frac{u'}{s_L^0}, \frac{L}{\delta_L^0}, Ma_T\right) \tag{1.1}$$

is expected to hold for the, where s_L^0 is the unstretched laminar flame speed, u' the r.m.s.-velocity fluctuations, L the integral scale and δ_L^0 the laminar flame thickness [6]. Stretch effects are found to play an important role even at moderate and high turbulence levels [7,8]. The sensitivity of a turbulent flame to stretch effects enters the correlation through the non-dimensional turbulent Markstein number Ma_T.

The concept of a turbulent flame speed in the form of Eq. (1.1) assumes that the heat release has a negligible effect on the flame propagation. However, heat release may wrinkle a flame front owing to a hydrodynamic instability (Darrius-Landau instability) associated with the density ratio across the flame [4]. Evidence exists showing that this instability has a non-negligible effect on the local flamelet structure by increasing the wrinkling and hence the flame speed for weakly turbulent flames, but its importance at moderate and high turbulence levels is still unclear [8,9]. Furthermore, the heat release may affect the overall approach flow velocity field and hence the propagation of the flame front if some constraint (confinement) limits the expansion of the burnt gas. The following review on flame flashback shows that for flame propagation close to a wall or in a swirling flow, the effect of heat release on the approach flow plays an important role.

The systematic investigation of flashback started with the work by Lewis and von Elbe, who studied flashback in Bunsen-flame type burners [10,11]. In such non-swirling pipe or channel flows, flashback is led by the upstream flame propagation in the boundary layer given that the centerline velocity exceeds the flame speed and that the premixture of fuel and air is homogenous (no wall-normal equivalence ratio stratification). Boundary layer flashback in non-swirling flows is schematically shown in Figure 1.2a. The model proposed by Lewis and von Elbe predicting flashback limits is shown in Figure 1.3. A laminar boundary layer profile is assumed. The solid red line marks the flame front, which propagates normal to itself at the laminar flame speed s_L. The flame speed decreases close to the wall as sketched in Figure 1.3b (red line) due to

heat loss to the wall and radical recombination at the wall before it is quenched at a distance δ_q. The flame has a convex shape due the decreasing flame speed with the most upstream portion being offset from the wall by so-called penetration distance δ_q, [12]. Flow velocity and flame speed are balanced if the velocity gradient at the wall matches the critical gradient $g_c = {}^{s_L}/_{\delta_p}$ as shown by the velocity profile (2) in Figure 1.3b. The model suggests that flashback occurs if the velocity gradient is smaller than the critical gradient as indicated by the profile (1). Following the work by Lewis and von Elbe, the focus of research on flashback has then been on measuring critical gradients for a wide range of fuels, fuel-air-ratios inlet temperatures and pressures for laminar and turbulent flows [12–16]. More recently the effect of additional parameters such as the burner rim or wall temperature, wall material and confinement on the critical gradient have been determined [17–22].

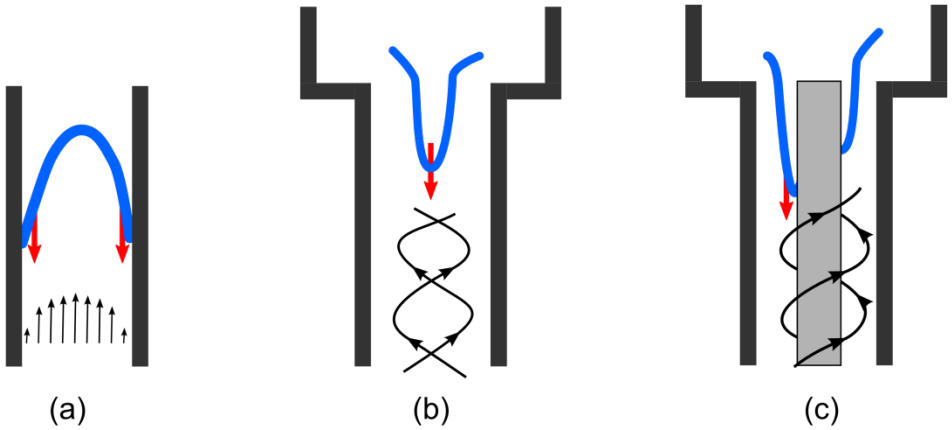

Figure 1.2: Three types of flashback. (a) Boundary layer flashback in (non-swirling) pipe or channel flows, (b) flashback in the core of a swirling flow, and (c) boundary layer flashback in a swirling flow.

Whereas the derived empirical correlations for critical gradients are valuable from a practical perspective, the critical gradient model is fundamentally flawed because it assumes an isothermal flow and hence no coupling between flame propagation and velocity field. More recent studies have shown that the flame front strongly modifies the approach flow both in laminar [23,24] and turbulent flows [24,25]. In turbulent flows, high-speed laser diagnostics and direct numerical simulation have shown that boundary layer flashback in channel flows is facilitated by small-scale flame bulges, which intermittently form inside low-momentum streaks of the turbulent boundary layer [24,25]. These bulges, which are associated with a local pressure peak at the convex flame tip, cause local pockets of reverse flow upstream of the flame front. The reverse flow pockets are found to reach above the quenching distance. The formation, counter-propagation and break-up process of the flame bulges leads to a net upstream propagation of the flame tip and hence flashback. Clearly, the effect the flame front has on the approach flow plays an important role for flame propagation along a wall. A model for the flame shape and propagation velocity of a turbulent boundary layer flashback has been proposed [26]. In this model, the turbulent flame speed is viewed as the speed at which the flame propagates relative to the undisturbed approach flow sufficiently far upstream of the flame brush. The effect of heat release on the approach flow is incorporated into the correlation for the turbulent speed in form of the density ratio across the flame.

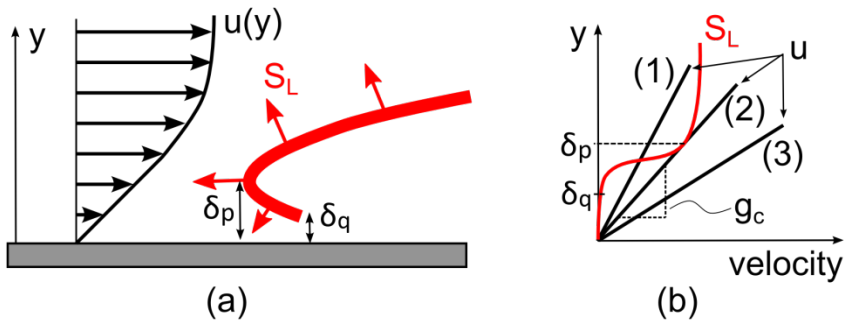

Figure 1.3: Critical gradient model for boundary layer flashback. (a) Velocity profile and flame front. (b) Wall-normal variation of flame speed and flow velocity for a situation corresponding to (1) flashback, (2) critical gradient, (3) blow-out. Adapted from [10].

In practical combustors, swirl flows are typically employed for enhanced mixing and flame anchoring purposes. The dynamics and stability of swirl combustors has been studied extensively [3]. Combustion instabilities may initiate a flashback process by providing, for instance, a momentary local low-momentum region or equivalence ratio stratification, which allows a portion of the flame to penetrate into the mixing tube. The danger for the combustor hardware lies in the sustained upstream flame propagation and flame anchoring inside the premix section [2]. Flashback in swirling flows may either occur in the core of the swirl flow (Figure 1.2b) or along a wall in the boundary layer (Figure 1.2c).

In swirl combustors without a central fuel tube (center body) in the mixing tube, the flame anchoring in the combustion chamber is achieved by a vortex-breakdown, which is triggered by the sudden expansion between the mixing tube and the combustion chamber. The two common types of vortex-breakdown at moderate and high Reynolds

numbers are the spiral type and bubble type breakdown [27–30]. Both types feature a stagnation point on the vortex axis. Flow recirculation downstream of the stagnation point only occurs in the bubble type breakdown. Despite extensive research over several decades, the phenomenon of vortex-breakdown remains controversial in isothermal and reacting flows, and still lacks a generally accepted mechanism explaining its occurrence and features [30].

Flashback in swirl combustors without center body tends to occur in the form of upstream flame propagation in the core of the tube along the vortex axis [31–40]. The flame base has been found to propagate upstream in a precessing motion about the tube axis [31,35]. High-speed measurements of the velocity field revealed a region of negative axial velocity in the vicinity of the upstream propagating flame base, which has been interpreted as a vortex-breakdown bubble of recirculating fluid [31,41,42]. Flashback in the core of swirling flows was henceforth referred to as flashback due to combustion-induced vortex-breakdown (CIVB) [31]. A model for the mechanism causing CIVB was derived based on a 2D unsteady RANS simulation by analyzing the magnitude of the different terms in the vorticity transport equation [41,43,44]. The model suggests that the cause for CIVB is the production of negative azimuthal vorticity due to baroclinic torque, which induces a negative axial velocity on the tube axis. The model further suggests that volume expansionhinders flashback as it produces positive azimuthal vorticity. The model is related to a model by Ashurst [45], which aims at predicting the significant increase in flame propagation speed of laminar flames propagating along a vortex axis.

The speed of laminar flames propagating along a vortex axis increases with an increase in azimuthal velocity and density ratio across the flame front. A number of models have been derived to predict the increase in flame speed, but a generally accepted theory has not yet evolved [46].

The third configuration concerns flashback of swirl flames along a wall, which by geometry combines aspects of boundary layer flashback and flashback along a vortex axis. In swirl combustors featuring a mixing tube with center body, flashback typically occurs along the center body wall [47–51]; however, boundary layer flashback has also been observed along the mixing tube outer-wall in hydrogen-air swirl flames [52]. Flashback along the center body wall has been attributed to CIVB based on the finding of regions of negative axial velocity upstream of the flame base [48–50,53]. The negative axial velocity regions have been interpreted as boundary layer separation where the recirculating fluid pulls the flame upstream [48]. A scaling law predicting the flashback limit as a function of the laminar flame speed was suggested [48]. The potential importance of the flame temperature, and hence the density ratio, as opposed to the flame speed, was suggested based on a study investigating swirl flame boundary layer flashback in a configuration with a conical center body [54]. It was observed that the flame statically creeps upstream along the conically shaped center body with an increase in density ratio and increase in flame speed but downstream with a *decrease* in density ratio and increase in flame speed .

A model based on the modification of the axial pressure gradient along the center body wall due to the low-density burnt gas has been proposed to explain the observed region of negative axial velocity [48]. Subsequent measurements of the static pressure on the center body wall during flashback revealed a pressure increase in the burnt gas [51]. A theoretical model predicting an adverse axial pressure gradient for a rotationally symmetric, axially propagating flame was derived by extending the flame-back-pressure theory [46] to include confinement and a center body [51]. In a similar extension of the original flame-back-pressure theory, a theoretical model predicting the pressure difference between unburnt and burnt gas in a purely swirling flame was developed [55]. Large eddy simulations of swirl flame boundary layer flashback were conducted to test computational models [56].

1.2.2 Volumetric measurement techniques for reacting flows

A number of different techniques to obtain three-dimensional information in reacting flows have been developed including multiple light sheets [57–59], time-space reconstruction [60], a scanning light sheet [61–64], light field technology with a plenoptic camera [65], stereo imaging of optically thick flames [66,67] and computed tomography (CT). The following review focuses on techniques utilizing CT as it forms the basis for an approach developed as part of the present work. In CT, the chemiluminescence is frequently utilized as the marker for the flame front and quantity to be reconstructed [68–75]. Either contributions from all excited radicals are collected or filters are used to

isolate emission from OH* or CH*. CT of flame luminescence has been conducted with a single camera to obtain the mean or phase-averaged flame shape [69,70,75]. However, to obtain an instantaneous flame surface, several simultaneous views are required; for example, seven and eight cameras have been used in [74] and [71], respectively. Alternatively, five cameras plus mirrors where used in [68] to project two views onto each camera sensor and hence obtain ten views. All studies successful in determining instantaneous flame surfaces have worked with low speed cameras owing to rather long exposure times necessary to integrate sufficient luminescence signal as well as the high cost of using a large number of high-speed cameras (particularly because high-speed cameras may have to be equipped with an intensifier for sufficient signal). CT based on flame luminescence requires the mitigation of any background interference due to reflections [76]. Only unconfined flames have therefore been investigated so far. Instead of utilizing the flame luminescence, Upton et al. performed CT based on the scattering from oil droplets that were densely seeded into the flow and vaporize in the preheat zone of the flame [77]. The oil droplets were illuminated with a custom made flash lamp and imaged from twelve views (six cameras together with a mirror array).

Mie scattering from oil droplets or particles illuminated by planar laser sheets is a common technique to detect flame fronts. Particle images of droplets, which vaporize at a particular isotherm in temperature typically corresponding to a location in the preheat zone of the flame, provide a sharp interface between unburnt and burnt gases [58,64,78–90]. In the case of solid particles, the flame front may be detected based on the gradient

in particle number density across the flame front due to the decrease in gas density, which has been found to agree well with the location of maximum heat release as obtained by CH-LIF or the product of formaldehyde and OH-LIF signals [91–93]. Alternatively, a recently developed technique using thermographic phosphor particles to simultaneously measure gas velocity and gas temperature [94–96] may in the future be used to detect flame fronts in reacting flows. Depending on the suitable temperature range associated with the utilized phosphor, the flame front may be defined by either an isotherm in the measured temperature field or as the location where the luminescence signal, obtained by exciting the phosphor, disappears.

Upton et al. [77] densely seeded the flow with oil droplets and reconstructed the continuous distribution of the scattering intensity to obtain the flame topography. If, instead, the flow is sparsely seeded with oil droplets, the velocity field may be simultaneously measured by means of tomographic PIV [97,98]. Tomographic PIV allows the measurement of the instantaneous volumetric velocity field and has only recently started to be applied to problems in the field of combustion including turbulent jet flames [71,99–102], IC engines [103], Bunsen flames [104] and premixed low-swirl flames [105].

Performing tomographic PIV at kilohertz repetition rates is particularly appealing to advance the understanding of turbulent flow-flame interactions as it provides volumetric insight with spatial and temporal coherence. High-speed tomographic PIV has been applied to study unsteady pressure fields as summarized in [106], to study

fundamental mechanisms in turbulent shear flows [107–110] and to investigate turbulent jet flames [100–102]. High-speed tomographic PIV at kHz rate has so far been limited to thin volumes on the order of 5 mm [98] due to small pulse energies available with typically employed diode-pumped solid-state lasers. The advantage of performing time-resolved velocity field measurements from a diagnostic point-of-view is that the velocity field obtained in a first iteration can be used to improve the initial tomographic reconstruction of the particle field [111]. A cross-correlation is then performed on the improved particle field to obtain an improved velocity field.

If PIV is performed in a volume that contains regions without particles then those regions in the particle field need to be masked to prevent any false contribution to the cross-correlation within that region or at the interface. If such regions translate and deform, then an algorithmic mask is needed that adapts to the moving object at every time step. Algorithmic masking techniques for volumetric PIV have so far been developed for optically thick objects in the flow based on the visual hull method [112] or based on textured surfaces [113,114].

1.3 Scope of the present investigation

Despite recent progress, many aspects of flashback are not yet understood. Given that practical combustors generally employ swirling flows for flame stabilization and mixing purposes, the focus in the present work is on flashback of swirl flames. Many swirl combustor designs feature a mixing section with a center body. In such

configurations, the upstream flame propagation during flashback tends to occur along the center body wall. The goal of this work is therefore to investigate *boundary layer flashback* of swirl flames. Advanced laser diagnostic techniques are applied to study the phenomenon experimentally. A new model swirl combustor with a mixing tube featuring a center body has been built for that purpose, which allows triggering flashbacks in a controlled manner and provides the optical access needed for diagnostic techniques. The combustor is described in Chapter 2.

The mechanism facilitating swirl flame boundary layer flashback is still unclear. Flashback has traditionally been investigated by measuring flashback limits as a function of various parameters such as fuel type, fuel-air-ratio, bulk flow, velocity, inlet temperature, pressure and, in the case of boundary layer flashback, wall material and temperature. For boundary layer flashback in non-swirling flows, correlations exist spanning a wide range of parameters. Such correlations are widely applicable since the flow field of non-swirling turbulent pipe and channel flows is well defined. In contrast, flashback limits of swirl flames tend to be burner specific since the flow field at the mixing section exit strongly depends on the geometrical details of the burner and the way swirl has been generated. The flow-field is not self-similar as a function of Reynolds number. Extracting universal, quantitative trends is difficult since any change in parameters, e.g. pressure, modifies the underlying flow field in a way not known *a priori.* Fundamentally understanding swirl flame flashback based on simple flashback-limit measurements has therefore not proven successful so far. Instead, recent investigations

increasingly focused on the upstream flame propagation during flashback events, enabled by the availability of high-speed diagnostic techniques and advanced numerical tools, to better understand the mechanism facilitating flashback. The present work investigates flashback by studying the upstream flame propagation for the same reason.

Previous studies have revealed that a strong coupling between flame propagation and the velocity field exists in all types of flashback. The key to advance the understanding of flashback hence appears to lie in the improved understanding of the flow-flame interaction during the onset and the upstream flame propagation. High-speed laser diagnostic techniques, which provide the velocity field and the flame front location, are therefore desired and applied in this work.

Only one previous experimental study investigated in detail the upstream flame propagation of boundary layer flashback in swirl flames [48]. The measurements were limited to measuring the two-component velocity field (radial and axial component) and to measurements in the unburnt gas. The azimuthal velocity, which potentially plays an important role in the mechanism facilitating flashback, has not been measured previously. In addition, interpreting the two-component velocity field is in several ways ambiguous in a highly three-dimensional flow-flame interaction, for instance because a differentiation between a stagnation region and purely swirling flow is not possible. Finally, the study was limited to methane-air flames; the effect of hydrogen was not investigated.

The first objective of this study is therefore to measure all three components of the planar velocity field and to conduct these measurements both in the unburnt and burnt gas regions. High-speed stereoscopic PIV is best suited since it provides the velocity field with both spatial and temporal coherence. In the current study, the inner structure of the flame is not important for understanding the flow-flame interaction on the integral scale. Hence, techniques extracting the flame front based on the Mie scattering images, which are readily available as part of the PIV measurements, are adequate. These techniques provide sufficiently accurate information on the flame front location with the advantage of being comparatively easy to implement and avoiding the need for additional expensive hardware capable of operating at kHz-rate. Stereoscopic PIV and planar flame front detection based on Mie scattering images are well established techniques, but a number of challenges associated with applying them in the current configuration had to be solved to obtain accurate, time-resolved data close to the center body wall. The details of the applied planar diagnostic techniques are described in Chapter 2.

Given the three-dimensional nature of the phenomenon, simultaneous knowledge of the 3D flame topography and the volumetric velocity field is desired. As summarized in Section 1.2.2, none of the existing techniques are capable of providing this simultaneous information at kHz-rate under the challenging conditions associated with conducting the measurements through a curved window close to a wall. Therefore, a technique not previously demonstrated successfully has been developed and validated. The technique to obtain the 3D flame topography is based on the tomographic

reconstruction of particles seeded in the flow and is combined with tomographic PIV to obtain the volumetric velocity field. The setup, data reduction and validation are covered in Chapter 3.

The primary objective of the work is then to utilize the novel information on the flame propagation and velocity fields to improve the understanding of boundary layer flashback in swirl flames. The focus in Chapter 4 is on the global flame structure and the propagation direction. In addition, the planar and volumetric velocity fields of the unburnt gas is investigated in detail to complete the understanding how the propagating flame front modifies the approach flow. The question is addressed how the flame propagation direction and the modified approach flow differ among the different flashback configurations (i.e. boundary layer flashback in swirling versus non-swirling flows), which is currently unclear.

Chapter 5 then analyzes an extensive dataset consisting of the planar three-component velocity field both in the unburnt and burnt gases for H_2/CH_4-flames ranging from 0 to 75% hydrogen. The objective of this chapter is to advance the understanding of the mechanism driving flashback and the effect of hydrogen on the mechanism.

The investigated flow rates in the present work are limited to a bulk flow velocity of 5 m/s, which is dictated by the available hardware (lasers and cameras) and the need for time-resolved measurements to advance the understanding of the mechanism facilitating the upstream flame propagation. Furthermore, the measurements are conducted at atmospheric pressure and ambient inlet temperatures. The work is valuable

because the understanding of swirl flame flashback is limited even at atmospheric pressure and it advances the fundamental knowledge of flame propagation in swirling flows in general. However, the investigated conditions are significantly different from the operating points of actual gas turbine combustors. The present work is nonetheless also valuable in that regard because it provides the thorough understanding of flashback at atmospheric pressure needed to better prepare for and decide on the focus of significantly more expensive and time-consuming high-pressure experiments. Experiments at elevated pressure have been started, but are not discussed in this thesis and instead are included in the outlook in Chapter 6.

Chapter 2: Experimental Setup

2.1 Swirl combustor: Design and Control

A new model swirl combustor has been designed and built to investigate flashback in a practical geometry. The swirl combustor features an axial swirler with attached bluff body (center body) as shown in Figure 2.1 allowing the investigation of boundary layer flashback of swirl flames. Images of the swirl combustor are included in Appendix D.

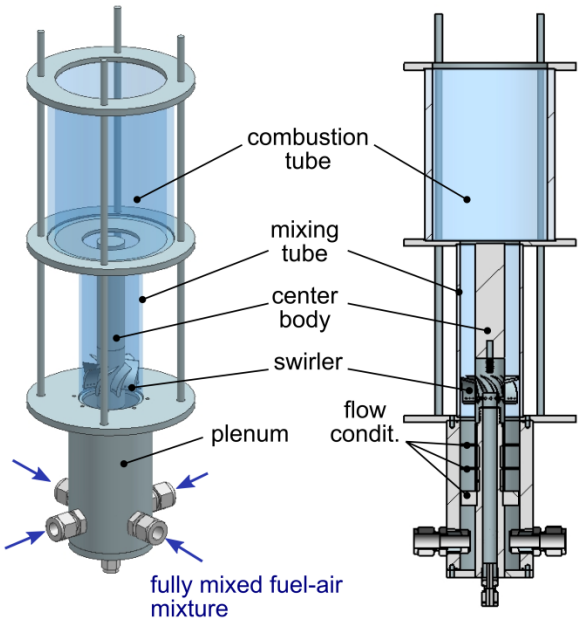

Figure 2.1: Model swirl combustor.

The burner was operated in a fully-premixed mode in this work in which the reactants are mixed before entering the plenum. The fuel and air streams are passed

through a custom-made static mixing pipe for that purpose, which houses a set of plates obstructing the flow path and inducing large-scale turbulence for intense mixing. A flashback arrestor (Witt Gas RF 85-10) between mixing pipe and plenum prevented any flame from propagating into the mixing pipe. The fuel-air mixture entered the plenum through four symmetrically arranged ports. A combination of a honeycomb section and wire-mesh elements inside the plenum ensured a clean inflow to the mixing tube.

Swirl was introduced with a single axial swirler consisting of eight vanes (Figure 2.2). The stainless-steel swirler was manufactured by selective-laser-melting. Each vane features six ports (three on each side), which may be used to inject fuel to operate the burner in a partially-premixed mode (technical premixing) where fuel-air mixing occurs in the mixing tube section of the combustor as opposed to a separate mixing pipe upstream of the plenum. No fuel was injected through these ports in this work as described previously. The vane trailing-edges were at an angle of 60° relative to the tube axis. The swirl number is approximately $S \approx 0.9$ based on a numerical simulation of the flow field and is calculated as the ratio of axial to circumferential momentum flux based on time and space averaged radial profiles in a plane 10 mm upstream of the mixing tube exit. The hub diameter of the swirler is 25.4 mm. A stainless-steel center body, of equal diameter to the swirler hub, was attached to the swirler, ending flush with the end of the mixing tube.

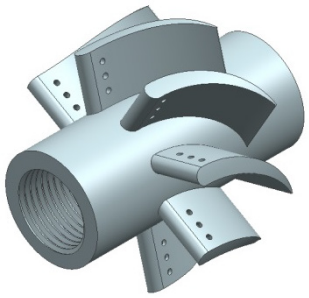

Figure 2.2: Solid model of the axial swirler.

To achieve accurate measurements inside the mixing tube employing the laser diagnostic techniques described in Section 2.2 and Chapter 3, a transparent tube with highest optical homogeneity was required. Standard quartz tubing, even with high optical homogeneity (e.g. standard MIL-G-174-B, grade A), inevitably has lengthwise striations due to its manufacturing process (electric fusion). These lengthwise striations were found to cause significant localized distortion in the crosswise direction [115]. After initial testing, the mixing tube was replaced by a synthetic silica tube (Heraeus Suprasil 310) with highest optical homogeneity (i.e. no striations in any direction) owing to a contact-less manufacturing process (flame hydrolysis). The mixing tube has a length of 150 mm and an inner and outer diameter of 52 mm and 56 mm, respectively. The combustion chamber consisted of a quartz tube with a length of 150 mm and an inner diameter of 100 mm.

Methane-air and hydrogen-methane-air mixtures were used as a fuel. Air und fuel mass flows were controlled using fast laminar-flow-element mass flow controllers (Alicat MCR series). The mass flows were controlled, monitored and recorded via a RS232

connection with a modified version of the Alicat LabView Device Driver. Flashback experiments started with a stable flame in the combustion chamber. The sudden expansion at the exit of the mixing tube caused vortex-breakdown, which, together with the wake of the center body, led to a region of low axial velocity in the core of the combustion chamber. This low velocity region held the conically-shaped flame in place downstream of the center body. The distance between center body and flame base under stable conditions was about 10 mm, depending on flow rate and equivalence ratio. Flashback was then initiated either by slowly increasing the equivalence ratio until the flashback limit was reached (investigation of onset of flashback, Section 5.2) or by a step-change in equivalence ratio to a pre-defined value. For the dataset discussed in Chapter 4 the step-change in equivalence ratio was achieved by a sudden change in the primary fuel flow rate. In the case of the dataset discussed in Chapter 5, the flame was ignited with the final fuel mass flow rates but an excess in air. Flashback was subsequently triggered by a sudden decrease in air mass flow rate. The PD control settings were tuned such that the sudden changes in mass flow rate were fast enough for the flame to propagate into constant equivalence ratio conditions in the measurement domain inside the mixing tube, which was tested by monitoring the increase in flame luminescence correlated with the arrival of the richer fuel-air-mixture.

The time from ignition to flashback was typically about 10 seconds to keep the thermal load on the combustor low. The center body was heated by both the incident laser sheet (Section 2.2) and the presence of the flame. Thermocouples were mounted inside

the center body to monitor its temperature. The short time that the heat load was experienced by the center body led to a wall temperature of less than 100°C for all runs discussed in Chapter 4. Varying center body temperatures below 100°C have been found to have neither a noticeable effect on global flame speeds nor on the flame propagation direction. Any conclusions drawn in Chapter 4 are hence for wall temperatures below 100°C. All flashbacks investigated in Chapter 5 were triggered once the center body wall temperature about 5 mm upstream of the mixing tube exit reached 80°C as a result of the combined heat load of the incident laser sheet and the stable flame in the combustion chamber.

2.2 Planar laser diagnostics

The interaction between the velocity field and the flame front is of primary interest to improve the understanding of flashback. High-speed Mie scattering imaging in a radial-axial plane served both to measure the velocity field and to detect the flame front location in this work (Section 2.2.1). Stereoscopic particle image velocimetry (PIV) was applied to measure the planar three-component velocity field (Section 2.2.2). The flame front was detected either based on oil droplets that vaporize in the preheat zone of the flame or based on the change in particle number density of solid particles (Section 2.2.3). The flashback duration was a few hundred milliseconds. All techniques were hence applied at kilohertz rate to temporally resolve the upstream flame propagation inside the mixing tube. In addition to the planar techniques described in this section, a technique

was developed to simultaneously reconstruct the 3D flame surface and measure the volumetric velocity field, which is discussed in Chapter 3.

2.2.1 High-speed Mie scattering imaging

The flow was seeded with olive oil droplets of approximately 1 μm diameter for measurements focusing on the velocity field in the unburnt gas (Chapter 4). The droplets were generated with an atomizer (TSI Six-Jet-Atomizer 9306). Measurements investigating both the unburnt and burnt gas velocity fields (Chapter 5) were conducted using alumina particles (Al_2O_3) of comparable size (~1 μm), which sustain flame temperatures. The alumina particles were seeded using a fluidized bed.

The air supply to the atomizer and fluidized-bed, respectively, was monitored with an Alicat mass flow meter connected to the LabView program controlling fuel and main air flow since the amount of seeding air was non-negligible in determining the overall equivalence ratio at which flashback was triggered. The seeded air flow entered the premixed fuel-air-stream upstream of the plenum (downstream of the flashback arrestor).

The particles were illuminated with two high-repetition rate, diode-pumped, frequency-doubled 527 nm Nd:YLF laser (Coherent Evolution-90) operated with about 10 mJ per pulse at a repetition rate of 4 kHz. The two laser beams were combined using a polarizing beam-splitter by rotating the polarization of one beam by 90° using a half-wave plate. Two mirrors upstream of the beam-splitter were used to adjust the near-field

and far-field alignment between the two beams. The beam was expanded and re-collimated with a plano-concave and plano-convex cylindrical lens, respectively, to form a sheet with a width of about 20 mm. A long focal length plano-convex spherical lens was used to focus the sheet.

Beam overlap was ensured and the sheet thickness was measured using a scanning knife edge technique similar to [116]. One mirror was replaced by a flat glass to reduce the laser sheet intensity while operating the lasers at nominal power. A knife edge aligned parallel with the laser sheet was translated in 10 μm increments with a translation stage to progressively block the sheet. The intensity was measured with a power meter (Ophir Nova). An error function was fitted to the measured intensity profile. The laser sheet profile (approximately Gaussian) was then obtained as the derivative of the interpolated error function. The sheet thickness (full-width at $1/e^2$ of the peak intensity) was approximately 1.0 mm.

The particle scattering was imaged with two high-speed CMOS cameras (FASTCAM-ultima APX) operated in forward scattering mode at a framing rate of 8 kHz and a resolution of 256 x 512 pix². The cameras were fitted with Scheimpflug adapters and Nikkor 105 mm lenses operated with an *f*/5.6 aperture. The angle between cameras and light-sheet normal was 30°.

To enable accurate measurements inside the mixing tube close to the center body wall, reflections from the fused silica mixing tube and the center body wall had to be eliminated. This was achieved by bringing in the light sheet from the top as shown in

Figure 2.3. A 2-inch mirror was placed in the hot exhaust gas to reflect the collimated laser sheet along the combustor axis. The mirror was protected by a quartz window mounted to an aluminum plate, which in turn was convectively cooled by a fan positioned outside the exhaust gas. The laser sheet was aligned to graze along the center body, which is a frequently employed strategy for near-wall measurements. A sample Mie scattering image (alumina particles) is shown in Figure 2.4. A portion of the center body wall is seen along the left edge of the image. Reflections off the center body were eliminated entirely provided that no flame is present in the field-of-view. The bright stripe along the right edge of the image corresponds to the fused silica tube wall.

In contrast, reflections did occur when a flame was present in the field-of-view. When a flame propagates along the wall, the light is refracted towards the wall due to the radial density gradient associated with the presence of the flame. To mitigate the occurrence of bright spots on the wall falsifying the cross-correlation in interrogation windows close to the wall, the cameras were rotated into a stereoscopic setup in the z-θ-plane (as opposed to the r-θ-plane) as shown in Figure 2.3 such that the line-of-sight was parallel to the tangent on the center body wall. With this setup, bright spots due to reflections were limited to within 1 to 2 pixels from the wall minimizing the necessary masking in that region and enabling valid velocity vectors to be computed close to the wall. An example with a few bright spots along the wall is shown in Figure 2.7a, which is taken from the same run as Figure 2.4, but now with a flame in the field-of-view.

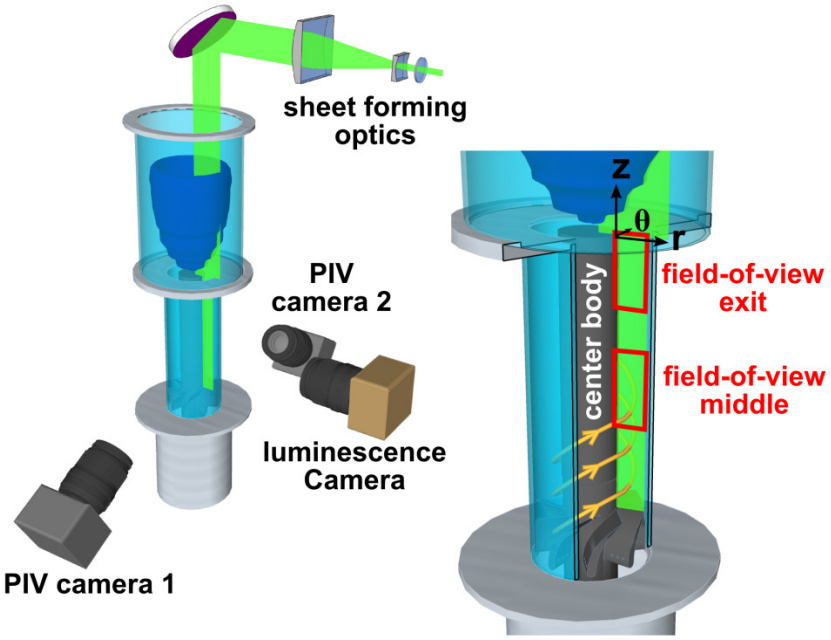

Figure 2.3: Diagnostic setup for simultaneous stereoscopic PIV, planar flame front detection and chemiluminescence imaging.

Measurements were taken in two different fields-of-view. The first field-of-view was positioned in the middle of the mixing tube with its top edge being located 42 mm upstream of the mixing tube exit plane (z = -42 mm). The second field-of-view was positioned with its top edge at the mixing tube exit. Both fields are 13.5 mm wide (to cover the width of the annulus) and 27 mm high with a pixel resolution of about 55 µm/pixel.

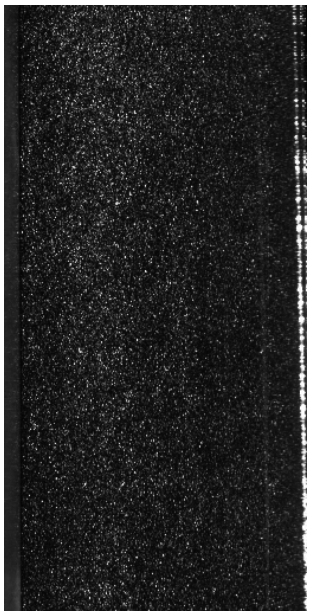

Figure 2.4: Sample particle image.

The swirl combustor design allowed the user to remove the center body for calibration purposes. A calibration target (dot target) was inserted into the mixing tube and mounted on a translation stage outside the tube. The dot target was aligned parallel to the laser sheet and traversed in the sheet-normal direction in 0.4 mm increments. Images were captured at each target position and imported into the LaVision Davis 8.2. software package to obtain the mapping function between sensor plane and physical space. A third-order-polynomial was assumed for the mapping function and was found to successfully capture the strong distortion introduced by imaging through the fused silica tube. The obtained calibration was improved by computing the disparity map and applying the stereoscopic self-calibration routine [117], which effectively removed any bias introduced by a misalignment between the calibration target and the laser sheet. The

disparity map was computed by simultaneously imaging the same particles with each of the two cameras. Each of the two images was then mapped to physical space using the original calibration. The two particle images were then divided into smaller interrogation windows and corresponding interrogation windows were cross-correlated. The computed displacement was the disparity in the location of particle-images between the two cameras and was solely due to a misalignment between the calibration target and the illumination plane. The self-calibration routine virtually rotates and translates the calibration target to minimize the mean disparity over all interrogation windows to obtain the corrected mapping function.

The lasers and cameras were synchronized externally by two pulse generators (SRS DG353). The timing is illustrated in Figure 2.5. The master clock provided an 8 kHz signal to the PIV cameras. The 8 kHz signal was further passed through a frequency divider to trigger the second pulse generator at 4 kHz, which in turn triggered the lasers with a proper delay.

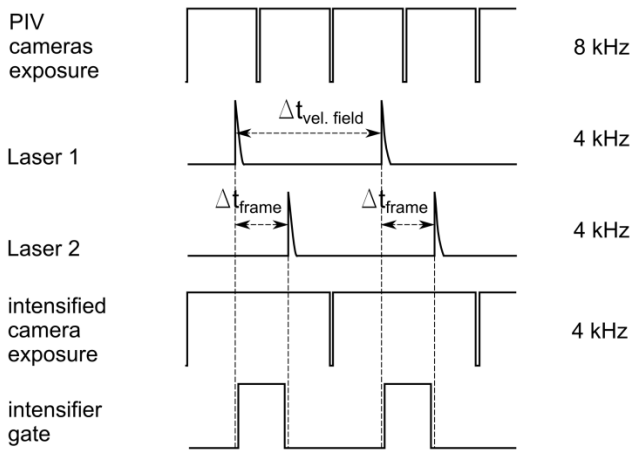

Figure 2.5: Timing diagram for stereoscopic PIV and chemiluminescence imaging.

2.2.2 Stereoscopic PIV

The three-component planar velocity field was computed based on the particle image pairs recorded at 4 kHz as described in Section 2.2.1. The time Δt_{frame} between the laser pulses of Laser 1 and Laser 2 (Figure 2.5) was set to 40 µs and 80 µs for the 5.0 m/s and 2.5 m/s bulk flow velocity case, respectively. The optimal Δt_{frame} is a trade-off between uncertainty in the particle displacement and correlation loss. In the investigated swirl flow the out-of-plane velocity was on the same order as the in-plane velocity. The limiting factor in maximizing Δt_{frame} was out-of-plane correlation loss.

The PIV processing was done with the LaVision software DaVis 8.2. A multi-pass cross-correlation approach with decreasing interrogation window size and window deformation was chosen in this study. The initial and final interrogation window sizes were 64 x 64 pix² and 16 x 16 pix², respectively, with 75% overlap. The cross-correlation was performed over a circular interrogation window with Gaussian weighting. The spatial resolution may be estimated as the interrogation volume within which the particle displacement is computed. With a pixel resolution of 50 µm/pixel, the in-plane interrogation window size was 0.88 x 0.88 mm². The depth of the interrogation volume is determined by the sheet thickness, which was about 1.0 mm (Section 2.2.1). Owing to the circular shape of the interrogation windows and the Gaussian weighting function these numbers are only an estimate for the spatial resolution.

The computed velocity fields contained a small percentage of spurious vectors. Typically, more than 95% of the vectors with a signal-to-noise ratio (ratio between first

and second correlation peak) of 2 were detected. The few spurious vectors were removed with a median filter and the resulting missing vectors were interpolated. No smoothing was applied to the final vector fields. The velocity field was filtered, however, before gradients were computed such as the vorticity or divergence field.

The mean stereo reconstruction error was typically 0.1 to 0.2 pixel. The uncertainty associated with the random error was computed using the correlation statistics approach, which provides the most accurate uncertainty estimates among the currently available methods [118,119]. The mean uncertainties (one standard deviation) of the three components in the instantaneous velocity fields are reported in Table 2.1 for a representative 2.5 m/s and 5.0 m/s bulk flow velocity run, respectively. The uncertainties corresponded to about 3% in the core flow of the in-plane velocity components (radial and axial) and about 5% in the out-of-plane velocity component (azimuthal). The relative uncertainty was found to increase in the boundary layer and peak at about 10% in the in-plane velocities and about 15% in the out-of-plane velocity.

In addition to the random error, bias errors may contribute to the total error associated with the stereo-PIV measurements. High-speed PIV measurements are prone to peak-locking owing to the employed high-speed low-resolution cameras [120]. Peak-locking, where the particle-image displacement is biased towards integer pixel displacements, becomes problematic for particle images smaller than 2 pixels in diameter [121]. In the current measurements, typical particle image diameters were 2-3 pixels.

PDFs of the modulus of particle-image pixel displacements indicated a moderate but acceptable level of peak-locking.

	u_{bulk} = 2.5 m/s	u_{bulk} = 5.0 m/s
σ_{u_r}	$0.07\ m/s\ (0.10\ pix)$	$0.16\ m/s\ (0.12\ pix)$
σ_{u_z}	$0.08\ m/s\ (0.12\ pix)$	$0.19\ m/s\ (0.14\ pix)$
σ_{u_θ}	$0.15\ m/s\ (0.22\ pix)$	$0.35\ m/s\ (0.25\ pix)$

Table 2.1: Uncertainty associated with the random error in the stereo-PIV measurements. The mean uncertainties σ_u of the instantaneous velocity fields are reported for the radial, axial and azimuthal velocity component for the 2.5 m/s and 5.0 m/s bulk flow velocity case.

PIV techniques rely on the tracers (seeded droplets or particles) to accurately follow the flow. The micrometer-sized olive oil droplets and alumina particles employed in this work were found to have relaxations times that are two to three orders of magnitude smaller than the smallest time scales in the present turbulent flow and hence in general follow the flow accurately. However, in reacting flows, where strong temperature gradients exist across the flame front, particles experience thermophoresis [122]. The thermophoretic velocity, which is induced in the direction opposite to the local temperature gradient, may be estimated as $u_{t.p.} = 0.5\nu\,\nabla T/T$ [123]. For the flames investigated in the current work the thermophoretic velocity was found to be at most 0.15 m/s, which is on the same order as the uncertainty due to the random error; hence,

thermophoretic effects only played a non-negligible role in regions where the absolute velocity component normal to the flame front was close to zero. In the case of the measurements with oil droplets, only the vectors closest to the flame front were affected owing to the droplets vaporizing in the preheat zone of the flame and the limited spatial resolution. In the case of the measurements with alumina particles, the two to three vectors across the flame front were affected.

Beam steering effects, in which light rays are refracted due to density gradients associated with the heat release, may introduce an additional error. The illuminating laser sheet passed through the flame in the current work and hence experienced some degree of beam steering. Furthermore, the imaged scattered light from alumina particles in the burnt gas passed through the flame front. The severity of beam steering was tested by comparing the disparity map between non-reacting and reacting cases. The disparity map was introduced previously as part of the camera calibration procedure (Section 2.2.1). The calibration does not account for beam-steering effects introduced by the flame and hence severe beam steering leads to an increased disparity. No systematic disparity indicative of a coherent refraction of the laser sheet was found. Furthermore, the fluctuations in local and instantaneous disparity in the reacting cases was found to be on the same level as in the non-reacting cases, which suggests that beam-steering effects are negligible in agreement with previous investigations [124].

The total error associated with the stereo-PIV measurements was further assessed in a similar configuration for the low bulk flow velocity case by measuring the velocity

field (reacting cases) with two independent sets of cameras to obtain a redundant solution. These measurements were part of the validation of the 3D technique discussed in Chapter 3. Since the two camera pairs were calibrated independently and the viewing directions differed, bias errors due to potential deficiencies in the calibration and due to beam steering effects contributed to the measured discrepancy between the two solutions. The discrepancy was assessed by computing the standard deviation of the difference between a solution and the mean of the two solutions. The resulting mean deviation of five different flashback runs range from 0.05 – 0.11 m/s (0.16 – 0.34 pixels) for the in-plane components and 0.09 – 0.13 m/s (0.28 – 0.41 pixels) for the out-of-plane component. These values are comparable to the uncertainties associated with the random error computed with the correlation statistics approach and hence provide further confidence in the accuracy of the stereo-PIV measurements.

2.2.3 Planar flame front detection

A number of different markers exist to detect the two-dimensional location of a flame front by means of planar laser diagnostics. Planar laser Rayleigh scattering thermometry may be used to measure the temperature field. The flame front is then typically defined as the location of the steepest temperature gradient [93]. Planar laser-induced fluorescence (PLIF) allows the detection of important species, which mark different regions in the flame. For instances, OH radicals mark the radical recombination zone whereas CH radicals mark the fuel consumption zone [125]. The product of OH and

CH_2O has been found to mark the location of the heat release [126]. Another frequently applied technique is the detection of the flame front location based on planar-laser Mie scattering images of aerosols seeded into the flow. Either the location where droplets vaporize or where a step-change in the particle number density of solid seeding particles occurs is extracted. Each approach has its strengths and weaknesses and so the best selection is very much dependent on the application and desired information. Inferring the flame front location based on aerosols is best suited for the current work where high-speed measurements of confined flames inside a fused silica tube close to the center body wall are needed to study the flow-flame interaction during flashback. The diagnostic setup for imaging the Mie scattering is described in Section 2.2.1. The flame front extraction based on olive oil droplets and alumina particles is discussed in Section 2.2.3.1 and Section 2.2.3.2, respectively.

2.2.3.1 Evaporating oil droplets

The olive oil droplets seeded into the flow vaporized in the preheat zone serving as a marker for the flame front in Chapter 3 and Chapter 4. The first use of this technique was by *Boyer* [78] and the analytical analyses by *Miles and Gouldin* [79,81], which estimated the iso-surface in temperature corresponding to the location where the oil droplets have vaporized to be about 650 K (with a lower limit of 425 K and an upper limit of 800 K). Both the evaporation of silicon oil [58,64,69,77,80,82–84,88,127–131] and olive oil [85–87,89,90,132] has since been extensively used as a marker in planar

measurements and has proven very valuable for advancing the understanding of both laminar flames and turbulent flames that fall within the flamelet regime. In the current work, measurements employing oil droplets were restricted to the leading portion of propagating flame tongues where the aerosol-based technique is reliable.

The isotherm at which the olive oil used in the present work vaporizes was tested in the current study to better characterize the location of the extracted interface within the flame. A Bunsen flame burner with an internal tube diameter of 16 mm was utilized for that purpose. Stable flames were tested at equivalence ratios of 0.8 and 1.0, and bulk flow velocities of 0.5 m/s and 0.8 m/s. The location of the interface where the droplets evaporate was imaged. Ultra-fine thermocouples (0.075 mm diameter) were then inserted to measure the temperature at that interface location. It was ensured that the thermocouple junction had a negligible influence on the flame front location by imaging the flame luminescence both with and without the thermocouple inserted. Due to the rather low temperature at which the oil droplets evaporate ultra-fine thermocouples are suitable to measure the corresponding temperature. A radiation correction was found to be insignificant at the evaporation temperature. The temperature was measured at five different locations along the Bunsen cone for three different flow and flame conditions yielding a mean temperature of 555 K with a standard deviation of 10 K. This finding compares well with previous studies using olive oil droplets, which stated an evaporation temperature of 570 K [85,86] and is comparable with silicone oil [81]. In conclusion, the

flame fronts presented in Chapter 3 and Chapter 4 mark the preheat zone and are coincident with an isotherm of about 555 K.

As in previous studies, the flame front is defined as the interface between regions with droplets (unburnt gas) and regions without droplets (burnt gas). A sample particle image with the superimposed extracted flame front of a hydrogen-methane-air flashback is shown in Figure 2.6. A series of image processing steps was implemented in a Matlab routine to automate the flame front detection. First, a binary image discriminating between regions with and without droplets was obtained based on an intensity threshold in 8 x 8 pix² interrogation windows with 75% overlap. Second, a morphological opening was performed both on the binary image and the inverted binary image to eliminate spurious patches in the unburnt and burnt gas regions. Third, the binary image was filtered with an averaging filter to avoid artificial high-frequency wrinkles due to the discrete nature of the particle pattern. The final binary image is taken as an algorithmic mask for the velocity field computation described in Section 2.2.2. The uncertainty associated with the automated detection of the flame front was estimated by computing the mean deviation between the solutions obtained from each of the two cameras, which was about 0.1 mm. This accuracy was sufficiently small for any conclusion drawn in Chapter 4 based on the approximate location of the preheat zone.

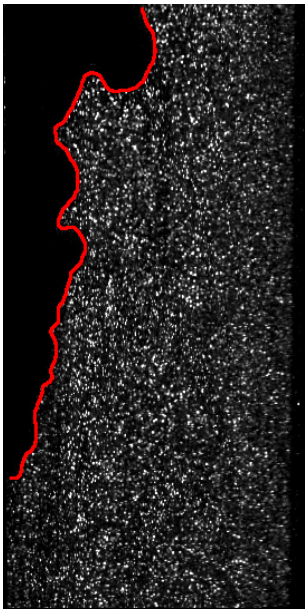

Figure 2.6: Flame front (red line) detection based on evaporating olive oil droplets. Hydrogen-methane-air flame (95% hydrogen by vol., $\phi = 0.4$).

2.2.3.2 Step-change in particle number density

For experiments conducted using alumina particles to measure both the unburnt and burnt gas velocity fields, the location of the flame front was detected based on the step-change in particle number density associated with the gas density gradient across the flame [91,92]. The change in particle number density is well defined across premixed flame fronts and has been shown to correlate well with the position of the maximum heat release in the thin flame regime [93].

A raw sample image of a hydrogen-methane-air flame flashback is shown in Figure 2.7a. A portion of the center body wall is seen along the left edge. The bright

stripe along the right edge originates from the fused silica tube wall. The low-seeding density region (dark) corresponds to burnt gas. The vertical striations are due to moderate beam steering effects. The dewarped and masked image, which was the basis for the flame front detection routine, is shown in Figure 2.7b. First, the Mie scattering images were filtered with a Gaussian kernel with a standard deviation of 3 pixels (Figure 2.7c). The histogram of the filtered intensities has a binary distribution as shown in Figure 2.8 where the left peak corresponds to burnt gas (low seeding density) and the right peak corresponds to unburnt gas (high seeding density). The minimum between the two peaks was taken as the intensity threshold discriminating between burnt gas and unburnt gas. This threshold was evaluated for each image individually. The corresponding binary image is shown in Figure 2.7d. The flame front extracted from the binary image is shown as a yellow line in Figure 2.7e. The flame front was filtered with a circular averaging filter with a 3 pixel radius to remove artificial high-frequency wrinkles due to the discrete nature of the particles. The resulting filtered flame front is superimposed as a blue line.

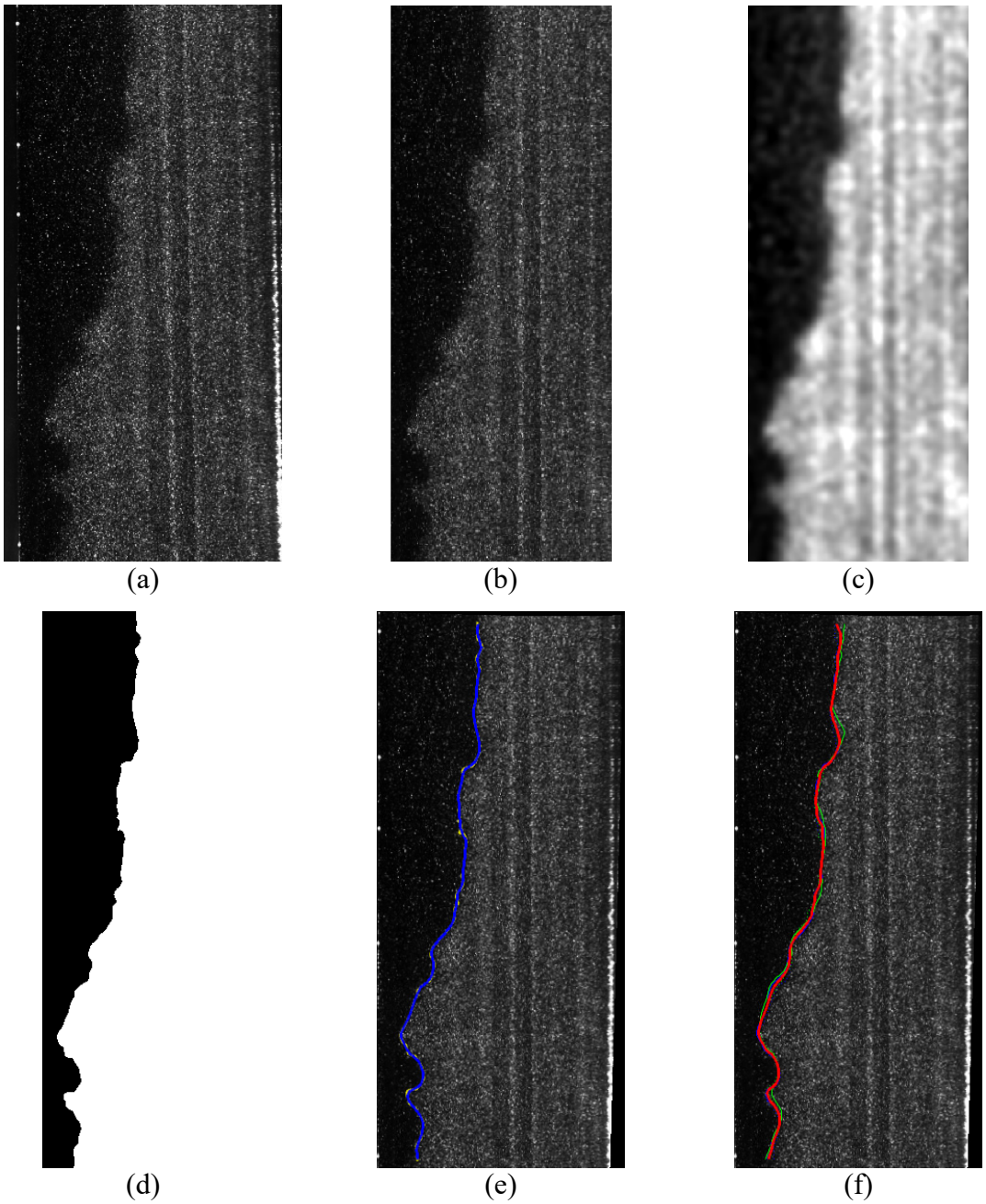

Figure 2.7: Planar flame front detection based on solid seeding particle number density. (a) Raw image (b) Dewarped and masked image (c) Filtered image (d) Binarized image (e) Unfiltered (yellow) and filtered (blue) flame front superimposed on dewarped image (f) Extracted flame fronts from Frame1/Camera1 (blue, solid), F2C1 (blue, dotted), F1C2 (green, solid), F2C2 (green, dotted) and mean flame front location (red, solid). Hydrogen-methane-air flame (25% hydrogen by vol., $\phi = 0.7$).

Each velocity field was computed based on four particle images (two cameras with two frames per camera recorded Δt_{frame} apart). Hence, four image frames were available at each time step to extract the flame front location, which are shown as blue and green solid and dotted lines in Figure 2.7f. If the calibration was perfect and the particle image intensities imaged by the two cameras identical, the flame front extracted from frame 1 of camera 1 and camera 2 would coincide exactly. In practice, slight deviations in the extracted flame front location existed. Furthermore, due to the finite propagation of the flame during the time Δt_{frame} between frame 1 and frame 2, the flame front extracted based on frames 2 of camera 1 and 2 was shifted. The magnitude of the shift depends on lab-frame-of-reference flame propagation speed and was typically about 1-2 pixels. In this work, the mean of the four extracted flame front locations was taken as the final flame front, which is shown as a red solid line in Figure 2.7. The uncertainty, defined as the mean distance between the mean flame front location and any of the four individual flame front locations, ranges between 2 and 3 pixels (0.12 to 0.18 mm) with a standard deviation ranging between 1 to 2 pixels for different runs.

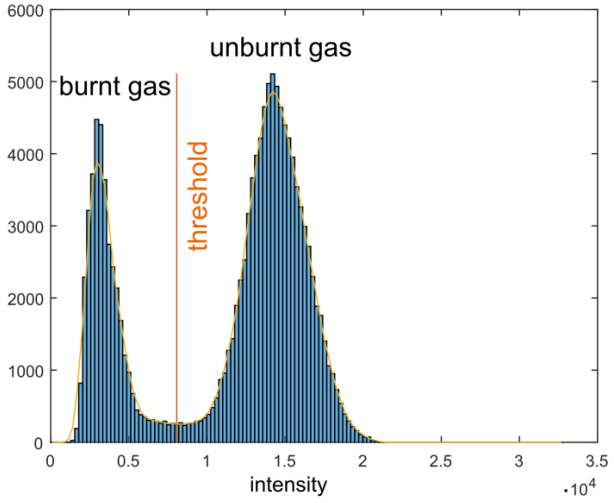

Figure 2.8: Histogram of filtered intensities corresponding to the image shown in Figure 2.7d.

2.3 Chemiluminescence imaging

The time-resolved flame luminescence was recorded simultaneously with all velocity measurements. In the first part of the work (Chapter 3 and Chapter 4), the luminescence was imaged with the intensified high-speed CMOS camera Photron FASTCAM-ultima APX-i2 at 4 kHz with a resolution of 512 x 512 pix². The camera was fitted with a Nikkor 105 mm lens with an f/2.8 aperture. No filter focused on the emission of one particular excited molecule was employed. The quantum efficiency and luminous gain of the fiber-coupled intensifier-camera system was sufficiently high to time the gain gate such that the luminescence was recorded between the two laser pulses for the Mie scattering images for best agreement between chemiluminescence images and velocity field data. The timing is shown in Figure 2.5. High-quality chemiluminescence images were acquired even for faint premixed, high-hydrogen content flames (Section 4.3).

The camera was set up such that the luminescence was viewed perpendicular to the laser sheet as shown in Figure 2.3. Information on how the flame propagates in and out of the laser sheet was hence available, which enabled an unambiguous interpretation of the planar velocity field and its location relative to a flame tongue.

In the second part of the work (Chapter 5), the APX-i2 was not available and so an external high-speed intensifier (Hamamatsu V6887U) lens-coupled to a regular Photron APX high-speed camera was used instead. The luminous gain of the Hamamatsu intensifier was lower and the phosphor decay time longer compared to the intensified APX-i2 system. The gain gate had to be positioned after the second laser pulse to increase the exposure time and achieve sufficient signal intensity. The resulting luminescence images were of lower quality due to smearing and a lower signal-to-noise ratio. Nonetheless, the images still provided the position of the flame in relation to the laser sheet, which was crucial to correctly interpret the instantaneous flow-flame interaction.

Chapter 3: Simultaneous 3D Flame Front Detection and Volumetric Velocity Field Measurement Technique: Setup, Procedure and Validation

Boundary layer flashback of swirl flames is a transient phenomenon characterized by a highly three-dimensional flow-flame interaction. Simultaneous, instantaneous, time-resolved volumetric measurements of the velocity field and flame topography were hence desired to investigate the phenomenon. None of the existing techniques summarized in Section 1.2.2 was suited for the current application as discussed in Section 1.3. An approach based on the tomographic reconstruction of the volumetric particle field has been developed and demonstrated successfully as part of this work. The diagnostic setup and data processing are described in Section 3.1 and Section 3.2, respectively. The reconstructed flame surface topography is validated in Section 3.3. The volumetric velocity field is validated in Section 3.4. The suitability of the technique with regards to studying flashback is assessed in Section 3.5. The content of this chapter has been reported in [133] .

3.1 Diagnostic setup

High-speed Mie scattering imaging from an aerosol seeded into the flow and illuminated with a laser is utilized to determine the three-dimensional flame topography and to measure the volumetric velocity field in the unburnt gas. The scattering is recorded from four different views, which provides sufficient information for a tomographic reconstruction of the three-dimensional particle field. As described in Section 3.2., the

reconstructed particle field provides the basis for the three-dimensional flame-front detection algorithm as well as tomographic particle image velocimetry (PIV) to obtain the volumetric velocity field.

Olive oil droplets with a diameter of about 1 μm were used as an aerosol in this work, which were seeded into the flow with a six-jet atomizer (TSI-Inc.). The olive oil droplets were illuminated with a high-repetition rate diode-pumped, frequency doubled (527 nm) Nd:YLF laser (Coherent Evolution-90) operated at a repetition rate of 5 kHz providing about 13 mJ/pulse. The laser beam was expanded into a collimated sheet with a height of about 30 mm by a set of cylindrical lenses. The large natural beam divergence of the employed laser system ($M^2 = 25$) was sufficient to provide a thick sheet with a thickness of about 17 mm (FWHM) at the probe volume location. However, a fairly constant and sufficiently high signal-to-noise ratio in the reconstructed three-dimensional particle field was only achieved in a region where the laser fluence available to illuminate the droplets was constant to within about 10% of the peak value corresponding to an effective thickness of about 4.5 mm; therefore, the sheet was clipped at that thickness by a set of knife edges. The thick sheet entered the mixing tube from the side and was retro-reflected in order to increase the laser fluence and homogenize the particle image intensities over the four cameras. Retro-reflection helped balance the scattering among the cameras because each camera received an equal amount of forward and backward scattering. The cylindrical fused silica mixing tube acts as a negative lens and thus required a positive cylindrical lens to compensate for the effect before retro-reflecting the

sheet as shown in Figure 3.1. A second set of knife edges was used to ensure overlap and to clip the outer regions of the sheet.

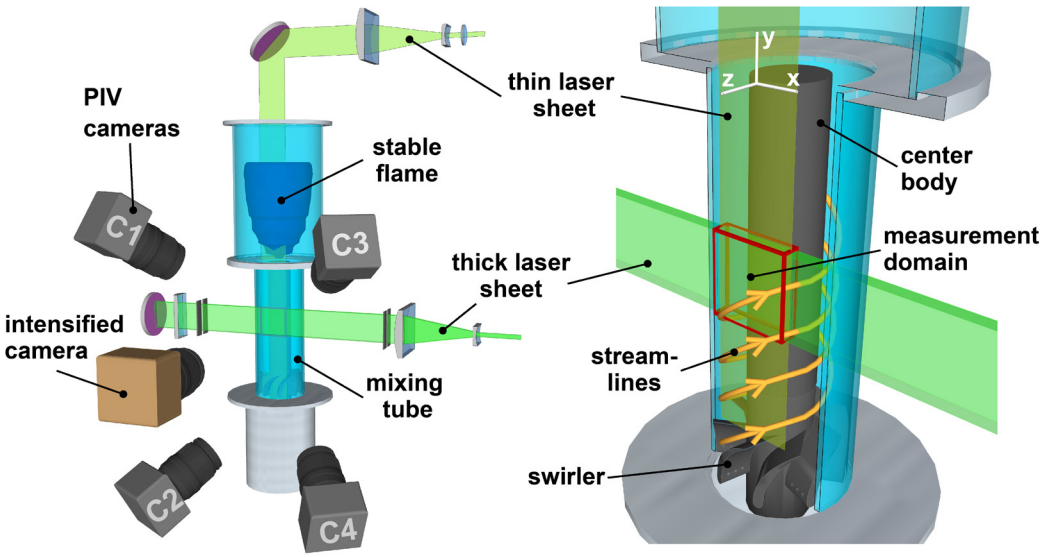

Figure 3.1: Diagnostic setup for the 3D flame front detection and tomographic PIV. An image of the diagnostic setup is included in Appendix D.

The measurements were conducted in a volume close to the center body wall about half way between the swirler and mixing tube exit. The thick sheet entered the mixing tube with a gap between it and the center body of about 0.8 mm to reduce background illumination, which primarily results from secondary scattering off the center body wall when illuminating the droplets. The scattered light intensity off the center body is not isotropic and depends on the polarization of the incoming light. A half-wave-plate was placed in the beam path to rotate the polarization and achieve a balance in the background illumination in the four camera views.

The volumetric results are validated against planar flame fronts and planar three-component velocity fields obtained by means of stereoscopic PIV. For that purpose, a second Coherent Evolution 90 laser was simultaneously used to illuminate the droplets in a thin sheet. A collimated 30 mm wide sheet was formed with a pair of cylindrical lenses. A long focal length spherical lens was used to focus the laser sheet to about 1.2 mm in thickness. This laser sheet thickness was needed to reduce the correlation loss to an acceptable level, which results from the large out-of-plane particle motion as a result of the long Δt between the laser pulses (which is dictated by the available hardware). The validation laser sheet entered the mixing tube from the top, as shown in Figure 3.1, and was positioned at one of two z-locations within the measurement volume. One location is in the center of the volume illuminated by the thick sheet ($z = 0$ mm) as shown in red in Figure 3.2; the second, shown in green, is towards the back edge of the volume close to the center body wall ($z = -2$ mm).

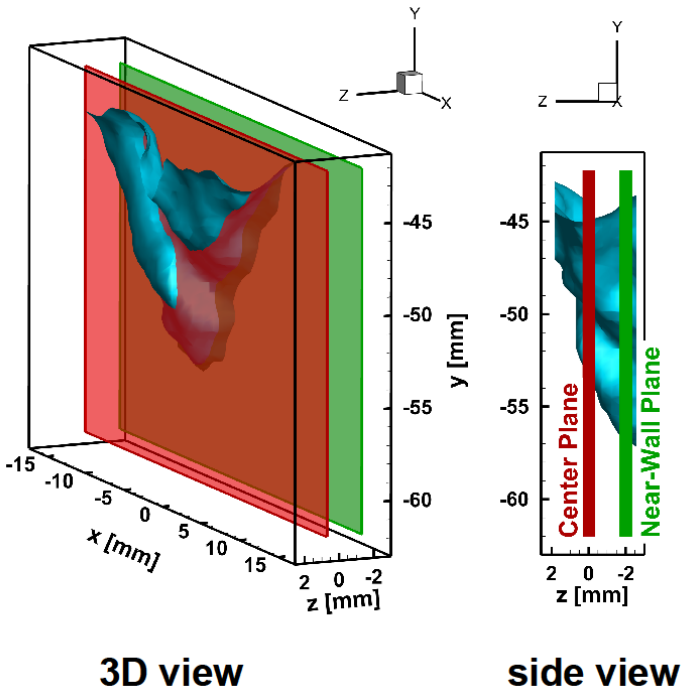

Figure 3.2: Locations of flame front and velocity field validation planes.

The Mie scattering was recorded with four high-speed CMOS cameras (Photron FASTCAM-ultima APX) operated at 10 kHz, which limits the resolution to 256 x 512 pix². The cameras were fitted with Scheimpflug adapters and Nikkor 105 mm lenses set to an aperture of f/8. The small aperture provided the depth-of-field needed for the particles to be in focus in the entire illuminated volume. The cameras were oriented in a diagonal cross-like arrangement with a total camera angle of about 60°, which is optimal for the tomographic reconstruction [98]. The field-of-view for each camera is about 30 x 15 mm² with pixel resolutions within 3% of 64 µm/pix. The cameras were calibrated by removing the center body and traversing a dot target through the

measurement volume. The calibration for the tomographic reconstruction was improved by applying the volume self-calibration routine [134]. The mapping errors should be below 0.3 pix for a good tomographic reconstruction [134] with typical values around 0.1 pix [98]. The remaining disparity in the present work is about 0.08 pix for all planes except those close to the curved fused silica mixing tube walls where the disparity increases up to about 0.15 pix due to an increase in distortion.

The four cameras were operated at twice the frequency compared to the lasers to quasi-simultaneously record both, the Mie scattering resulting from the droplet illumination by the thick sheet as well as from the illumination by the thin sheet. The timing is illustrated in Figure 3.3. A master clock (SRS DG353 pulse generator) provided external synchronization to all four cameras operating at 10 kHz. The 10 kHz signal was passed through a frequency divider to trigger a second SRS box at 5 kHz, which in turn triggered the lasers. Laser 1, which provided the thick sheet for the volume diagnostics, fired with a delay of 95 μs such that frame 1 in each of the cameras captured the corresponding Mie scattering. Laser 2, which provided the thin sheet for the planar reference measurement, fired with a delay of 105 μs, placing the pulse at the beginning of camera frame 2. The small time delay of 10 μs between the pulses of laser 1 and laser 2 introduced a small bias error when comparing the resulting flame front locations and velocity fields. However, with peak velocities smaller than 5 m/s, droplets move by less than 0.05 mm (0.8 pix) between the acquired images during which time the flame front location and velocity flow field are essentially frozen. The particle displacement of

0.05 mm is significantly smaller than the uncertainty in the extracted flame front location. The displacement is also small when considering the time resolution of the velocity measurement, since the relevant time step for the velocity measurement is the 200 µs between two subsequent pulses of the same laser. PIV essentially provides a velocity field that is averaged over these 200 µs, which is the same for the volumetric and the planar measurement as both lasers run at 5 kHz. The averaging window is merely shifted by 10 µs for the planar measurement compared to the volumetric one.

The particle field illuminated by the thin sheet will provide four individual planar reference flame fronts (one per camera) and two independent planar three-component velocity field solutions (one per camera pair) at each time step for validation purposes.

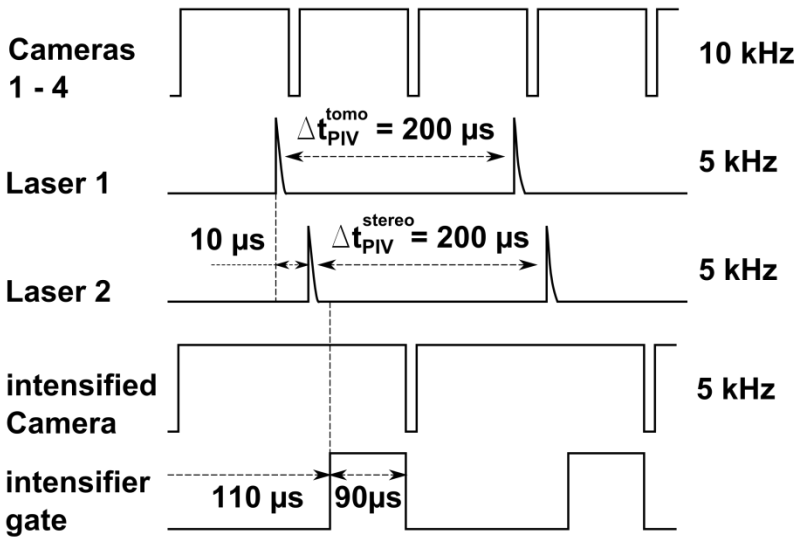

Figure 3.3: Timing diagram for 3D measurement validation.

The flame luminescence is simultaneously imaged with an intensified high-speed CMOS camera (Photron FASTCAM-ultima APX-i2) at a resolution of 512 x 512 pix². The corresponding field-of-view is about 50 x 50 mm² spanning the entire diameter of the mixing tube and reaching above and below the field-of-view for the volumetric and planar flame front detection and velocity measurement. The camera is fitted with a Nikkor 105mm lens with an f/2.8 aperture. The second digital delay generator (SRS DG535) provided the 5 kHz signal to the camera to synchronize it with the lasers. The gain gate was set to start 5 μs after the first pulse of the second laser and ended with the end of the camera frame 90 μs later, as shown in Figure 3.3, which provided a good trade-off in exposure time for sufficient luminescence signal without smearing out the flame fronts.

3.2 Data processing

3.2.1 Flame front extraction

Olive oil droplets were seeded into the flow and subsequently vaporized in the preheat zone serving as the marker for the flame front in this technique. The validity of using evaporating oil droplets to mark the flame front is discussed in Section 2.2.3. The flame front is defined as the interface between regions with droplets (unburnt gas) and regions without droplets (burnt gas).

The overall procedure to extract the three-dimensional flame front includes preprocessing of the particle images captured by the four cameras followed by a

tomographic reconstruction of the three-dimensional particle field. The reconstructed particle field is then improved in two iterations by taking information on the velocity field into account. A set of image processing steps is then applied to the final three-dimensional particle field to detect the void region in the particle field and extract the interface corresponding to the flame topography. Each of these steps is described in detail in the following paragraphs.

A raw particle image from one camera at an instant in time when the flame is in the field-of-view is shown in Figure 3.4a. The raw particle images suffer from high background intensity owing to applying the technique to flames in a confined space close to windows and walls. The background intensity is highest where the center body is in the background, which is the case in the right half of the region occupied by burnt gas in Figure 3.4a. The majority of particle images in the unburnt gas have a peak intensity that is a factor of 1.3 to 2.0 above the local background intensity, which requires image preprocessing to retain as many true particle images as possible while removing background noise efficiently. A sliding average in time with a kernel size of five time steps is subtracted first followed by subtracting a constant intensity value. The constant is evaluated such that the remaining background intensity in regions of burnt gas as seen in Figure 3.4a is removed. The constant differs from camera to camera and is furthermore adjusted among different cameras such that the resulting source densities associated with the image sets from each camera agree well. This procedure ensures that approximately the same number of particles remains in the images corresponding to the four different

views. However, since Mie scattering is anisotropic, this procedure does not ensure that the particle image corresponding to one particular particle is retained in all four camera views as the peak intensity may be above the background-intensity-dependent threshold in one view but below it in another. Consequently, particles missing in some views as well as residual background intensity add to the ghost particle level in the reconstructed particle field. In the tomographic PIV literature, ghost particles refer to artifacts in the reconstructed particle field due to solving a highly underdetermined system based on only a few views. Here we use a broader definition of ghost particles that refers to any particle in the reconstructed field that does not correspond to a true particle in the flow.

An example pre-processed particle image is shown in Figure 3.4b. Black regions correspond to regions where the burnt gas extends over the entire depth illuminated by the thick laser sheet. Regions with a low image source density – a quantity typically measured in particles-per-pixel describing how dense the particle images appear in a recorded image – correspond to regions occupied by both unburnt and burnt gases in the depth direction. Hence, the flame front is within the probe volume in such regions of the recorded image. Since the source density decreases the farther the flame front penetrates into the probe volume in the depth direction and the reconstruction quality increases with a decrease in source density, a more accurate flame surface reconstruction is expected in such situations. In a final step, Gaussian smoothing followed by a sharpening filter is applied to the particle images for noise reduction without increasing the ghost energy.

Ghost energy or ghost intensity refers to the intensity associated with artifacts in the reconstruction process (ghost particles).

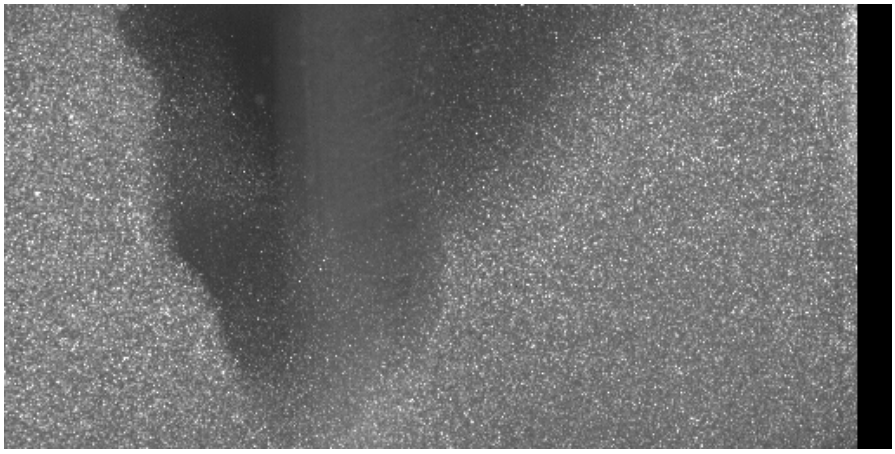

(a)

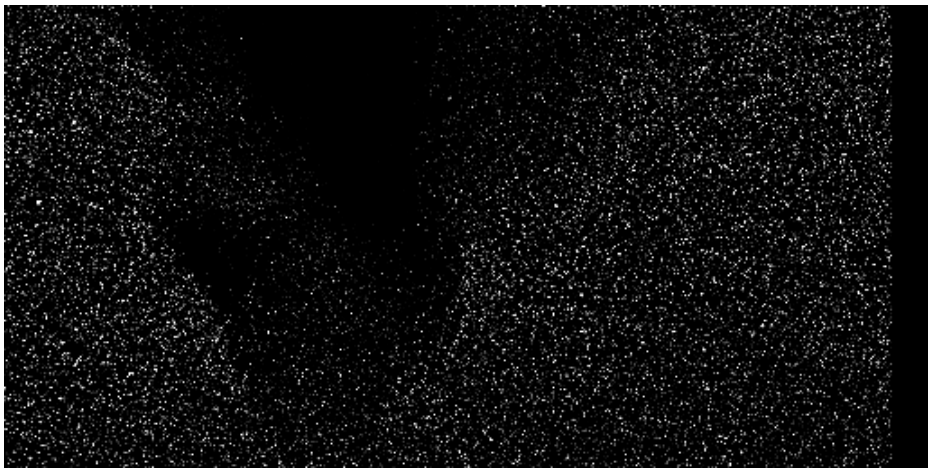

(b)

Figure 3.4: Raw particle image (a) and pre-processed particle image (b).

The tomographic reconstruction to obtain the volumetric voxel-based intensity distribution is performed using the fast-MART (simultaneous multiplicative algebraic

reconstruction, CSMART) algorithm within the LaVision DaVis 8.2. software employing 6 iterations with a sparseness threshold of 0.01 counts. The CSMART algorithm is a more efficient implementation of the sequential MART (SMART) algorithm [97], which takes advantage of the sparsity of the reconstructed volume by not updating voxels below the sparseness threshold [135]. The volumetric intensity distribution is referred to as the volumetric or reconstructed particle field in this work. A metric to assess the reconstruction quality is the reconstruction signal-to-noise ratio SNRR with values greater 2 indicating a high-quality reconstruction [98], [136]. The SNRR in the current experiment varies between 1.7 and 2.3 for the different runs, which is at the lower limit of the acceptable level and a direct result of the low quality raw particle images associated with performing high-speed diagnostics inside a confined space close to walls and windows.

A first solution of the velocity field was obtained (see Section 3.3) based on the initial particle field. The reconstructed particle field was then improved by performing two iterations of Motion-Tracking-Enhancement (MTE) [111], [137]. MTE improves the reconstruction accuracy by taking into account that the particle fields are correlated in time. The correlation is provided by the velocity field, since only true particles follow the velocity field. This method is exploited to reduce the intensity of ghost particles by mapping particles forward and backward in time based on a good initial guess of the velocity field and summing the intensity distributions appropriately. A total of 5 time steps (enhancement objects) are taken into account as part of the MTE processing in this

work. The three-dimensional flame topography detection and the simultaneous volumetric velocity field measurement are therefore linked. In that sense, taking the velocity field into account increases the accuracy of the detected flame front topography. MTE-MART is computationally expensive, but a recently proposed new implementation for time-resolved measurements may be utilized instead in the future, which strongly decreases the computational burden and even increases the reconstruction quality [138].

The DaVis native files containing the reconstructed particle fields were imported into Matlab to perform the void region detection and flame front extraction procedure. The difference between the established planar technique to detect flame fronts based on Mie scattering images and the new volumetric approach presented in this work is the fact that the void region corresponding to burnt gas is not based on actual particle images directly but instead on the reconstructed particle field containing ghost particles.

The flame front detection routine starts with deleting particles below an intensity threshold since ghost particles are characterized by low peak intensities [139]. A number of ghost particles, however, remain and will limit the spatial resolution of the extracted flame topography since regions of burnt gas have to be evaluated on an interrogation volume basis rather than relying on the location of individual particles. In a second step, particles are located in the volume using a three-dimensional regional maxima filter. The particle density is then computed based on a sliding 16 x 16 x 16 voxels^3 interrogation volume with 50% overlap. The volume is binarized by marking regions as unburnt gas if the particle density is equal or larger than six particles per interrogation volume. The size

of the interrogation volume sets a limit in terms of spatial resolution. The optimal interrogation volume size is a trade-off between spatial resolution and the reliability of the automated detection scheme. The result in general contains small erroneous islands indicating burnt gas inside the unburnt gas and vice versa as well as artificial high-frequency noise along the flame front that are eliminated with a set of morphological operations. A three-dimensional morphological erosion with a spherical structuring element of unity radius (interrogation window) followed by a dilation with the same structuring element is performed. This procedure removes artificial high-frequency wrinkles along the flame front while preserving the sharp edges, and also fills the small erroneous islands. The size of the structuring element sets a limit on the size of the small pockets of burnt or unburnt gas that are detectable as well as the small scale features detectable along the flame front. The resulting binary volume marking regions of burnt and unburnt gases is smoothed with a box filter (kernel size of 3) and the flame front is extracted as the 0.5 iso-surface.

The thin-sheet validation measurements provide for four independent planar flame front images, one for each of the four cameras. For each particle image, the particles are mapped to physical space, and then the particle fields are processed with an automated flame front detection scheme. The thin laser sheet illuminating the planar particle field entered the combustor from the top and passed through burnt gas as well as the flame front, which caused vertical striations in the laser sheet due to light refraction as the sheet experiences density gradients. The particle image intensity was hence first

homogenized by dividing the image by a horizontal intensity profile averaged over regions where no flame was present. In previous works, if the vaporization of oil droplets is utilized as a marker for the flame front, the flow is typically densely seeded. A number of metrics, e.g. a local intensity average, are then capable of robustly discriminating between reactants and products and a flame-front extraction based on a threshold is rather straightforward. In the current experiment, the seeding density was low as required for the tomographic reconstruction and the background intensity was high due to reflections off the center body wall. Together, these effects led to filtered particle intensities in the burnt gas being similar to the filtered intensities in the unburnt gas. Furthermore, even the "thin" laser sheet was fairly thick (about 1.2 mm) as discussed previously, which led to the illumination of droplets in the tails of the laser sheet and hence additional smearing of the intensity gradients in parts of the flame front that were characterized by a large out-of-plane gradient. Even though the tails of the laser sheet illuminated particles, high peak intensities were only obtained in the central part of the laser sheet. Regions of unburnt gas were therefore identified based on a weighted correlation between peak particle intensity (obtained by a sliding maximum filter) and average intensity (obtained by a sliding average filter), which was found to reliably detect the flame front in the vast majority of cases (assessed by comparing the four individual solutions). However, the uncertainty in the extracted flame front was still significantly higher compared to experiments optimized for detecting the planar flame front based on densely seeded flows as discussed in Sections 4.2 and 4.3.

A set of morphological operations comparable to the volumetric case was then applied to remove erroneous islands inside the burnt and unburnt gases. The final flame front extracted from the binary image was filtered to remove the high-frequency noise. The spatial grid based on which the four planar flame fronts were evaluated differed slightly as dictated by the individual mapping functions corresponding to each of the four cameras. The final four flame fronts were therefore linearly interpolated to a fixed spatial grid with a pixel resolution of 0.1 mm for comparison. Slices through the three-dimensional flame topography were interpolated to the same spatial grid for validation.

3.2.2 Velocity field measurement

The volumetric velocity field was determined by performing tomographic PIV. The image pre-processing and tomographic reconstruction has been discussed as part of the flame-front detection routine in Section 3.2. Each successive pair of reconstructed intensity distributions obtained every 200 µs was cross-correlated (time-series mode), which led to particle displacements of about $9 - 18$ voxels with a mean of about 14 voxels. The void region corresponding to burnt gas, which was obtained in Matlab for each time step as part of the flame front detection routine, was used as an algorithmic mask for the PIV processing by switching on the mask flag for the corresponding voxels in the DaVis native data structure and then writing it back to a file to be imported into DaVis. The remaining PIV processing was conducted in DaVis using version 8.2. The cross-correlation was performed with an initial interrogation volume size of

64 x 64 x 64 pix³ and a final size of 32 x 32 x 32 pix³ with 75% overlap. Spurious vectors in intermediate vector fields were detected by the universal outlier detection scheme [140]. The time-resolved nature of the processed velocity field was utilized to perform a final outlier detection in a 5 x 5 x 5 vector neighborhood in space and a 3-vector neighborhood in time. No spatial smoothing was applied to the final vector field.

For the validation measurements, stereoscopic PIV was applied to obtain two independent planar three-component reference velocity fields. The processing was set up to match the tomographic PIV measurement in terms of the in-plane spatial resolution by choosing a final interrogation window size of 32 x 32 pix² and an overlap of 75%. A comparable outlier detection scheme was employed again taking advantage of the correlation in time in a final step. The final vectors were located at slightly different physical locations between the two independent planar velocity fields depending on the exact camera location and mapping functions. The velocity vectors were linearly interpolated to a common fixed spatial grid for comparison. The fixed grid had a constant vector spacing of 0.5 mm. The tomographic PIV solution was interpolated to the same spatial grid for validation.

3.3 Flame front validation

The 3D flame topography is first qualitatively compared to simultaneously acquired chemiluminescence images (Section 3.3.1). Quantitative validation is achieved by comparing the reconstructed flame topography to simultaneously detected 2D flame

fronts based on planar Mie scattering images in two different slices through the volume (Sections 3.3.2 and 3.3.3).

3.3.1 Qualitative comparison to chemiluminescence images

The reconstructed three-dimensional flame front was first qualitatively compared to simultaneously-recorded chemiluminescence images. Figure 3.5 shows luminescence images and reconstructed flame topographies at three instants in time taken from a movie sequence of a flame swirling upstream inside the mixing tube during a flashback event. Note that the luminescence is line-of-sight integrated; hence, the flame may appear to be inside the field-of-view in the luminescence image even though it is in fact behind or in front of the volume within which the three-dimensional flame front is reconstructed. An example for such a situation is seen in the luminescence image in Figure 3.5a, where a second flame tongue swirling around the center body appears inside the field-of-view in the bottom-left corner. In comparison, only the centrally-located flame tongue is present in the reconstructed topography. However, the second flame tongue seen in the luminescence is still behind and has yet to swirl into the volume within which the flame is reconstructed. Also, note that the large central region where no flame surface is seen in the reconstructed topography corresponds to a portion of the flame that extends in front of the reconstructed volume.

With the line-of-sight versus finite depth-of-field difference in mind, the quality of the reconstructed flame topography may be examined. In Figure 3.5a, the overall shape

of the flame front as well as a detailed structure – the bulge on the right edge of the flame – are captured well. The leading flame tongue continues to swirl upstream when a secondary flame tongue appears in the field-of-view 60 frames (or twelve milliseconds) later as shown in Figure 3.5b. The recessed region between the leading flame tongue on the right and the secondary flame tongue on the left forms in Figure 3.5b and is well captured in the reconstructed topography. Note that this recess has a width of about 1.5 mm, but seems to be quite well resolved. The secondary flame tongue is subsequently convected downstream as shown in Figure 3.5c. The three-dimensional reconstruction is able to capture the rather pointy shape of the flame at this instant in time as well as the bulge in the top left part of the flame tongue.

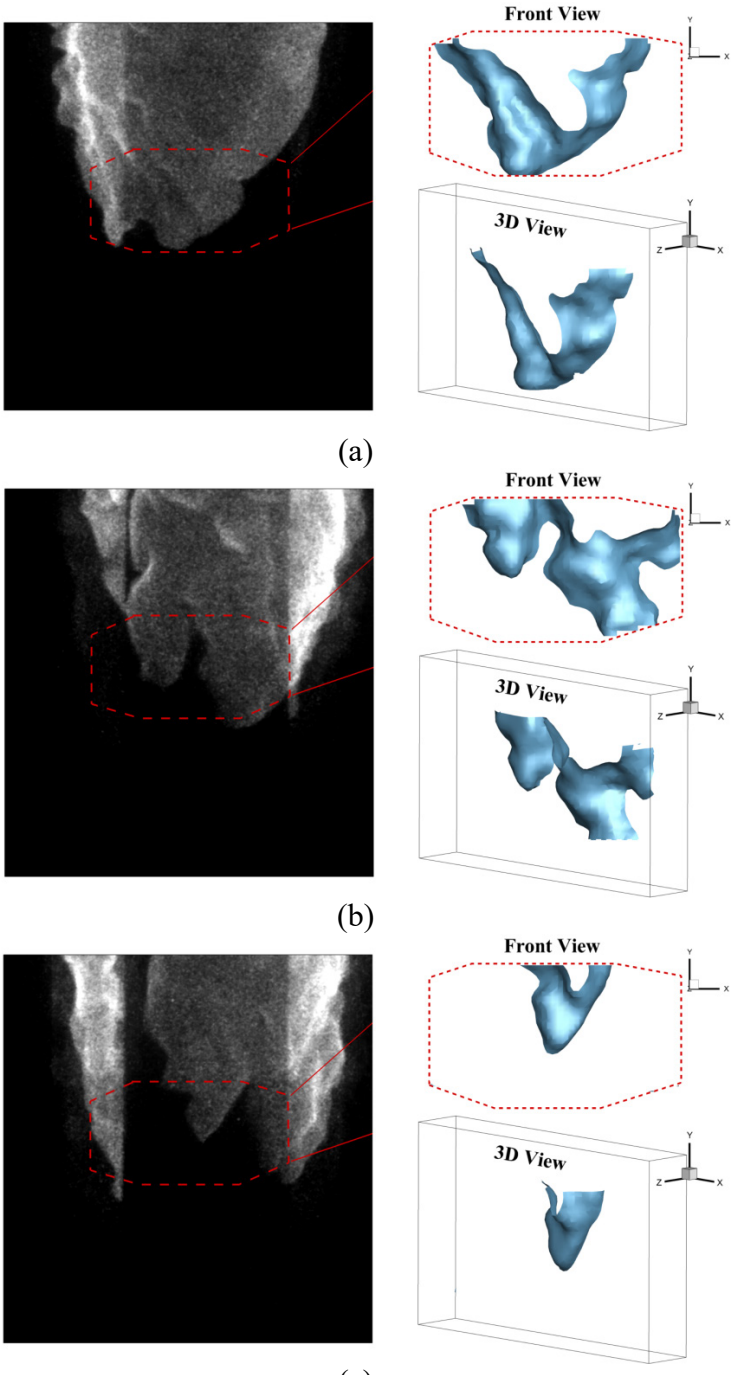

Figure 3.5: Comparison between flame luminescence (left, line-of-sight) and reconstructed 3D flame front (right, front view and 3D-view) at three instants in time taken from a movie sequence of a flashback event. (a) $t = t_0 + 10.2$ ms, (b) $t = t_0 + 22.2$ ms, (c) $t = t_0 + 25.6$ ms.

3.3.2 Quantitative assessment in center plane

The accuracy of the volumetric flame topography detection technique is assessed quantitatively in this work by comparing slices through the obtained three-dimensional flame front to the simultaneously-acquired planar flame fronts. Four independent solutions for the planar flame front are obtained in the current work as each of the four cameras provides an independent particle image. This approach is suited as validation because the marker for the flame front in the planar reference measurements is the same as the marker employed for the three-dimensional flame front detection, i.e. the location where the same droplets seeded into the flow vaporize.

In a first set of runs (Run 1-3) the thin sheet is placed in the center of the thick sheet in the z-direction – subsequently termed "center plane" – as shown in red in Figure 3.2. The true thin sheet location, however, may shift from time step to time step due to refraction as a result of the strong density gradients across the flame front (beam steering). To test the severity of beam steering, the stereo self-calibration algorithm was applied to a sliding interval of 50 images [117]. The resulting disparity maps suggest a translation of the calibration plane in the out-of-plane direction (corresponding to a shift of the laser sheet) that differs by as much as several tenths of a millimeter compared to the corrected calibration of the non-reacting reference case. The shift may even be larger for individual time instants since the disparity maps are an average of 50 time steps. As a result, the obtained calibration, which provides the mapping between camera sensor plane and physical space, has a varying degree of accuracy depending on the instantaneous true

laser sheet position. At each time step, the four particle images (one from each camera) were mapped to physical space using the camera-specific calibrations in order to extract and compare the planar flame fronts. The uncertainty associated with the planar flame front solutions will be acknowledged in the form of error bars when validating the three-dimensional flame surface.

Figure 3.6a shows the four flame fronts which were independently extracted from the particle images of each of the four cameras in red tones and blue tones at one instant in time of Run 1. The discrepancy between the four solutions may partially be attributed to imperfect mapping functions due to beam steering effects as discussed previously. In addition, differences may be a result of the challenges associated with the automated flame front extraction based on the low signal-to-noise ratio particle images as discussed in Section 3.2. Shown in green is the most-probable planar flame front location which is taken as the reference flame front for validation purposes. The deviation (Euclidian norm) of each of the individual flame fronts from the most-probable flame front is evaluated for all points and all time steps. The corresponding PDFs for Run 1 are shown in Figure 3.7. The particle image quality is significantly better for cameras 2 and 4 than for cameras 1 and 3, which results in longer tails in the PDFs for the latter two cameras. Whereas deviations up to about 1 mm result from imperfect mapping functions as well as challenges in the automated extraction of flame fronts, deviations above 1 mm can solely be attributed to spurious portions in the detected flame fronts. For cameras 2 and 4, the amount of spurious flame front elements is less than 1% leading to a mean deviation of

about 0.2 mm from the most-probable flame front. In contrast, about 15% to 20% of flame front elements of cameras 1 and 3 are spurious, which leads to a mean deviation of about 0.5 mm. Points on the flame front where one solution deviates by more than 1 mm from another were considered to be unreliable and were not included in the statistical analyses of the accuracy of the three-dimensional flame topography. By excluding such spurious flame front elements the mean deviation of flame fronts detected based on images from camera 1 and 3 was reduced to the same level (about 0.2 mm) achieved with cameras 2 and 4.

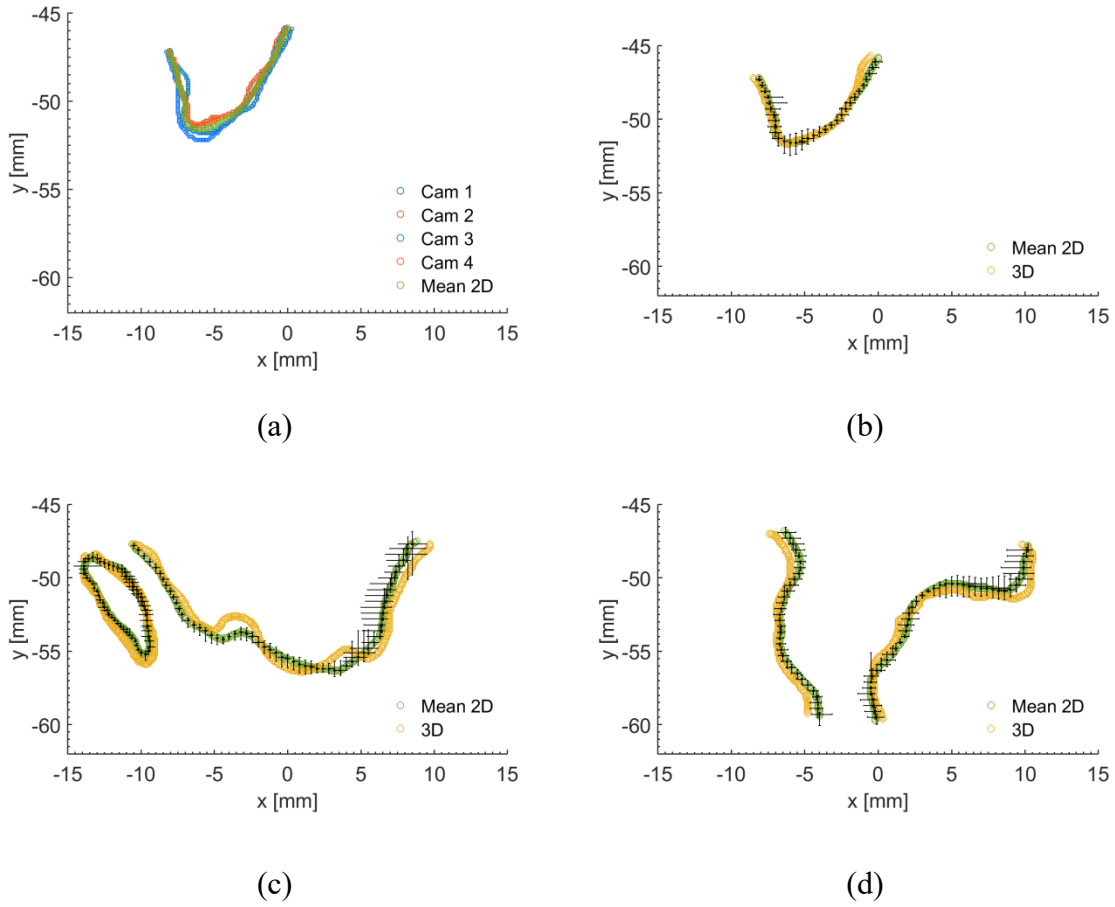

Figure 3.6: Flame topography validation in the center plane: (a) Planar flame fronts extracted from each of the four cameras (blue and red) are shown together with the resulting most-probable location (green). (b) – (d) Slices through the 3D flame front (yellow) are compared to the most-probable planar flame front (green) for different time steps. Error bars indicate uncertainties associated with the planar flame front location.

A slice through the reconstructed three-dimensional flame front is shown in yellow in Figure 3.6b and compared to the most-probable planar flame front at the same instant in time. The reconstructed flame front shows good agreement with only a slight deviation in the top right portion. Error bars are plotted for every fourth point on the planar flame front. The error bars indicate the uncertainties associated with the most-

probable planar flame front. The uncertainty at one point is computed from the Euclidian distances from each of the four individual flame front solutions shown in Figure 3.6a to the most-probable location based on a 95% confidence interval and assuming a t-distribution. An additional uncertainty only implicitly included in the error bars is the positional uncertainty associated with the z-position at which the slice through the three-dimensional flame front is compared to the planar flame front. At one instant in time, the thin laser sheet providing the planar flame front may be shifted due to beam steering in relation to where the slice through the three-dimensional flame front is placed. This uncertainty is implicitly included in the planar flame front because a deviation of the instantaneous laser sheet position from the mean position associated with the camera mapping function will lead to an increased discrepancy between the individual flame fronts and hence an increase in computed uncertainty.

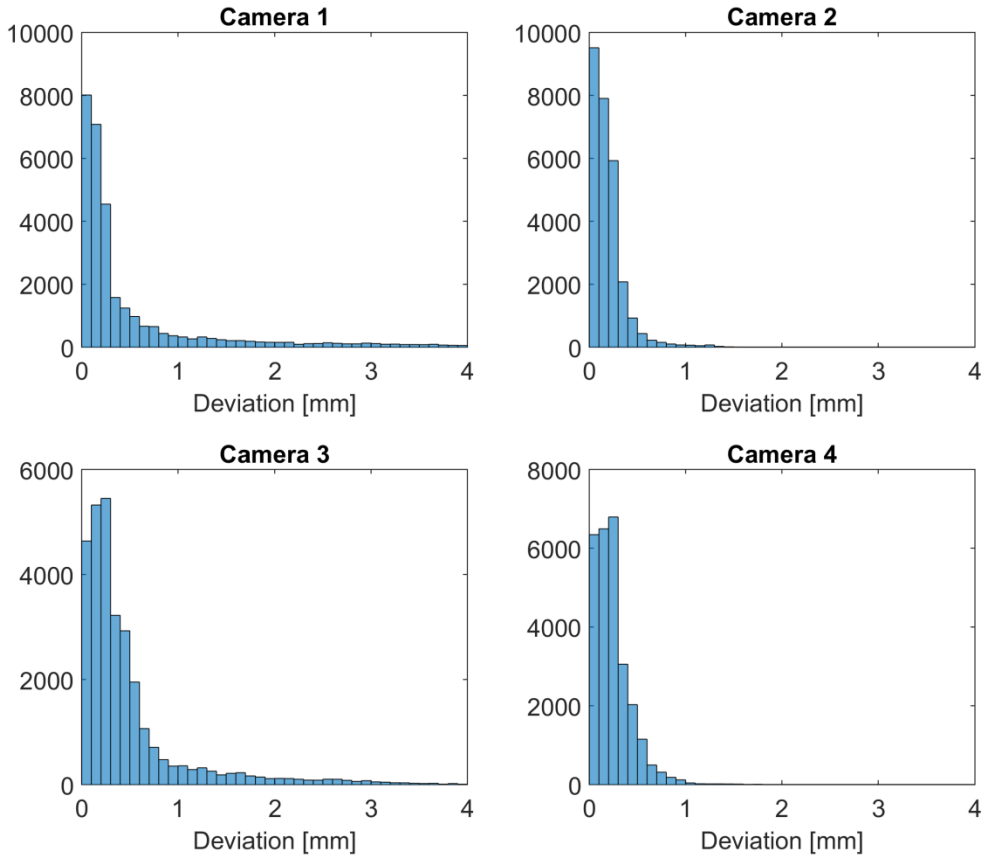

Figure 3.7: Uncertainty associated with planar reference flame front of Run 1: Deviations of individual planar flame fronts from each of the four cameras relative to the most-probable planar flame front.

A more challenging flame topography which appears to feature a detached pocket of ignited gas is shown in Figure 3.6c. The seemingly separated pocket in this planar slice is, however, merely the result of significant out-of-plane flame curvature, which is captured well by the reconstruction technique. In contrast, the reconstruction technique exaggerates the flame bulge on the lower left side of the main flame patch and adds another bulge on the lower right side, which is not seen in the planar solution. The final

example shown in Figure 3.6d is a case where the leading flame tip has propagated far enough upstream to reach beyond the field-of-view. Therefore, despite some discrepancies, overall good qualitative agreement is again achieved with the reconstruction technique.

The accuracy of the three-dimensional flame front reconstruction is assessed quantitatively by defining an error as the distance between each point on the two-dimensional slice through the three-dimensional flame front and its closest point on the previously discussed most-probable planar flame front. PDFs with the resulting error for all three runs conducted with the validation plane location being the center plane are shown in Figure 3.8. All three PDFs have peak counts between 0.2 and 0.3 mm. For Run 1, 95% of the points on the flame front deviate less than 1.2 mm from the planar reference flame front. The mean error of these 95% of points is 0.36 mm. In the case of Run 2 and Run 3, 95% of the points deviate less than 2.2 mm and 1.4 mm, respectively, with corresponding mean errors of 0.44 mm and 0.46 mm. The mean errors are listed in Table 3.1.

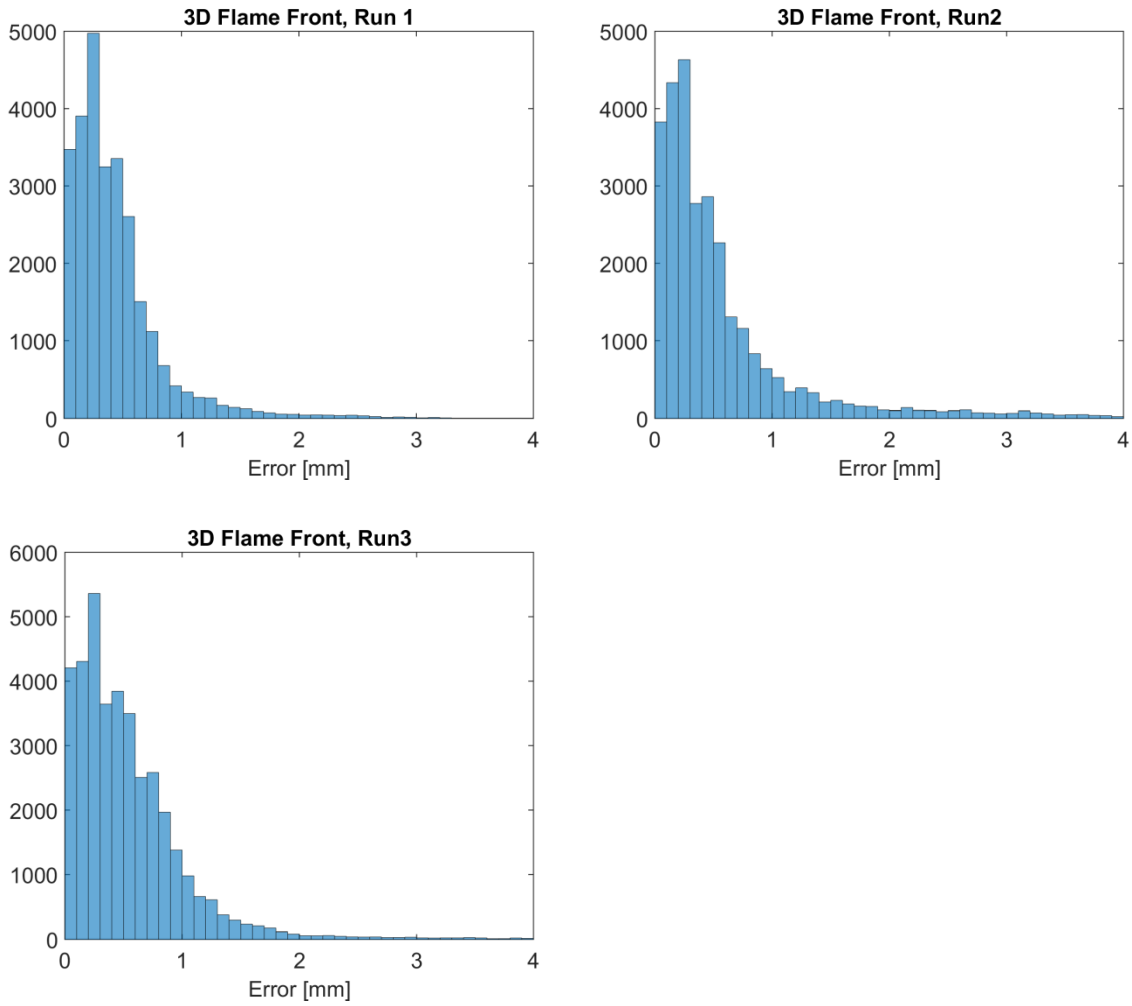

Figure 3.8: PDFs of the error associated with the 3D flame topography taken from all time steps of three separate flashback events (Run 1–3). The error is evaluated in the center plane (see Figure 3.2).

Run	Validation Plane	Mean Error ($d_{95\%}$)	
1	Center	0.36 mm	5.6 voxels
2	Center	0.44 mm	6.9 voxels
3	Center	0.46 mm	7.2 voxels
4	Near-Wall	0.33 mm	5.2 voxels
5	Near-Wall	0.27 mm	4.2 voxels

Table 3.1: Mean error in the location of the reconstructed three-dimensional flame front for 5 different flashback events.

3.3.3 Quantitative assessment in near-wall plane

An additional two runs (Run 4 and 5) were conducted to validate the three-dimensional flame topography in a plane towards the back-edge of the volume close to the center body wall termed “near-wall plane” in Figure 3.2. The reconstructed flame front is again compared to the planar flame front at three instants in time. The chosen time instants correspond to the chemiluminescence images shown in Figure 3.5.

Figure 3.9a and Figure 3.9b highlight again how the discrepancy in the individual planar flame front locations translates into error bars associated with the most-probable planar flame front. The flame front in a slice through the three-dimensional flame topography shown in Figure 3.9b is again in good agreement with the planar solution. The bulge in the planar flame around x = 0 mm and y = -59 mm does not appear in the reconstructed flame front. However, the planar flame front is associated with an increased uncertainty in this region. The complete three-dimensional flame topography at this instant in time is seen in Figure 3.5a.

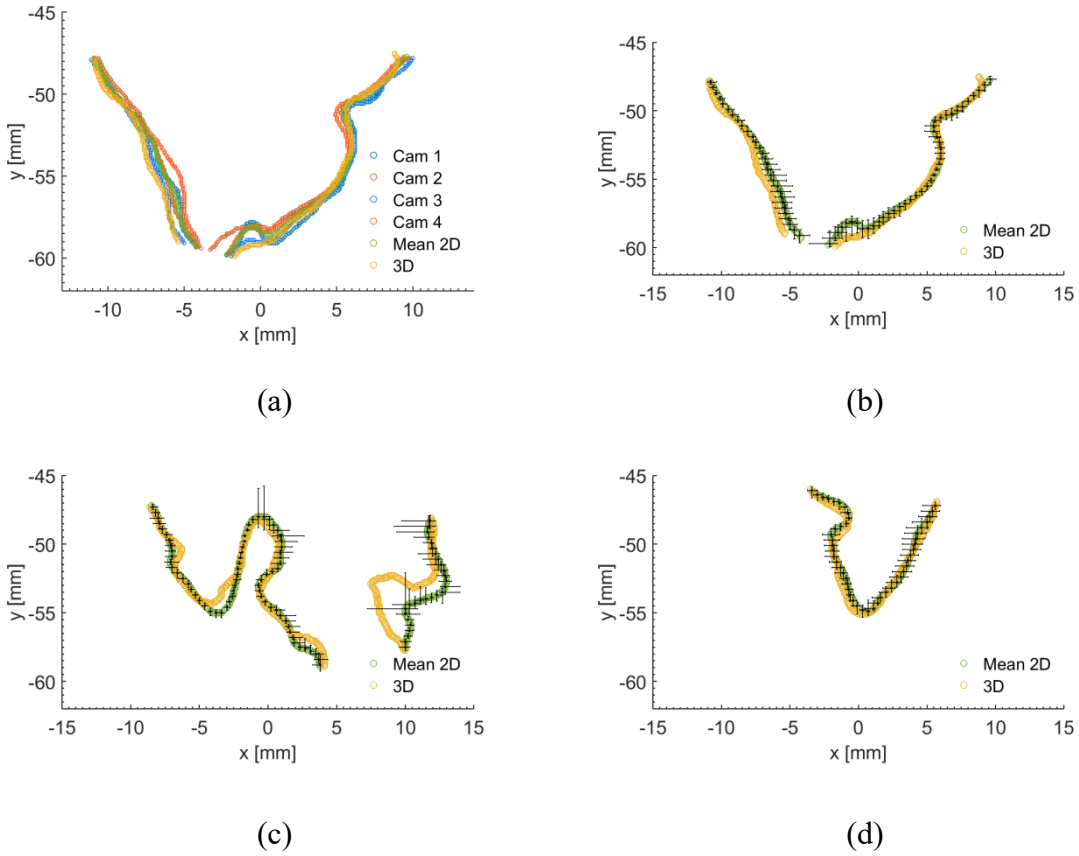

Figure 3.9: Flame topography validation in the near-wall plane: (a) Planar flame fronts extracted from each of the four cameras (blue and red) are shown together with the resulting most-probable location (green). (b) – (d) Slices through 3D flame front (yellow) are compared to most-probable planar flame front (green) for different time steps. Error bars indicate uncertainties associated with the planar flame front location.

A slice through a more convoluted flame topography is seen in Figure 3.9c, which corresponds to the chemiluminescence image and full three-dimensional flame front shown in Figure 3.5b. This comparison confirms the good agreement in location and size of the recess between the two flame tongues already suggested by the qualitative comparison to the flame luminescence image. However, a rather large deviation between

the three-dimensional and planar flame front solutions exists in the right portion of the flame. Interestingly, though, this part of the flame front is also associated with a large uncertainty in the planar solution.

The PDFs showing the quantitative error when evaluated in the near-wall plane are given in Figure 3.10. For Runs 4 and 5, 95% of the points on the flame front have an error of 1.4 mm and 0.8 mm or less, respectively, corresponding to a mean error of 0.33 mm and 0.27 mm, respectively. Note that the flame was inside the field-of-view during fewer time steps in Run 5. The better accuracy in the reconstructed flame front location of Run 5 can be explained by the fact that the flame only covered a small portion of the field-of-view during the majority of the time steps. The reconstruction of the three-dimensional flame topography was found to be more reliable in the center of the field-of-view where the signal-to-noise ratio of ghost particles versus actual particles is lower. Comparing the error in the near-wall plane to the center plane does not show a decrease in accuracy near the wall, which may be explained by the fact that the signal-to-noise ratio in the reconstructed particle field at the z-location of the near-wall plane is comparable to the ratio at the z-location of the center plane (the experiment has been setup for this to be the case).

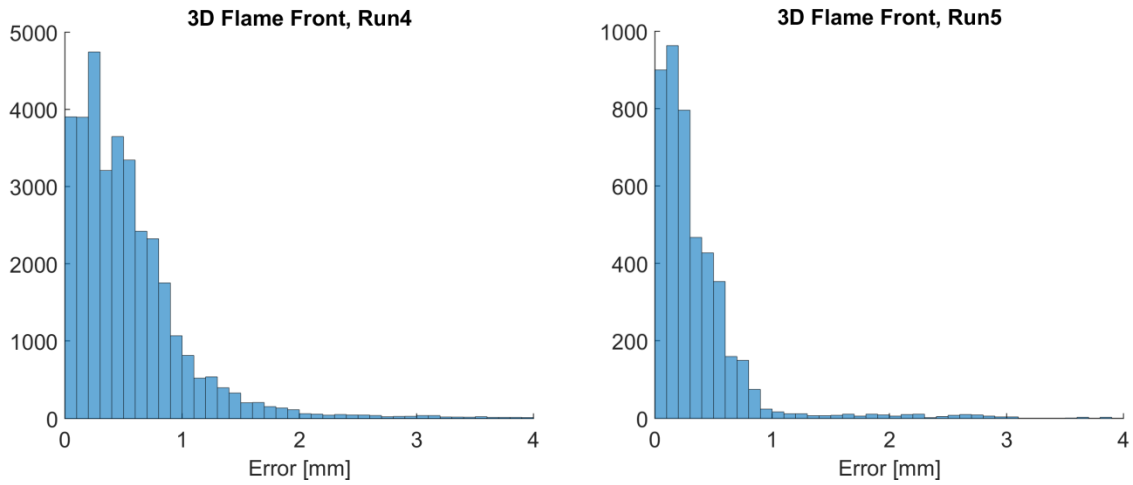

Figure 3.10: PDFs of the error associated with the 3D flame topography taken from all time steps of two separate flashback events (Run 4–5). The error is evaluated in the near-wall plane (see Figure 3.2).

In summary, the slices through the reconstructed three-dimensional flame topography compare well to the simultaneously detected planar flame fronts. The mean error in the center plane as well as the near-wall plane is about 0.4 mm corresponding to about 6 voxels, which is a moderate increase of about a factor of two compared to the mean uncertainty in the extracted planar reference flame front. Note, however, that this rather large uncertainty of the planar reference flame front is a result of the low seeding density needed for a tomographic reconstruction, as well as the challenges associated with flame front detection with high background intensity and noise. Under ideal conditions and for high seeding densities, a planar flame front can be extracted based on Mie scattering images with uncertainties on the order of 1 pixel as demonstrated in previous works [58,78,82–84,88,131,141]. In contrast to the planar approach, the three-

dimensional technique requires a trade-off in seeding density, which needs to be as low as possible for a reliable reconstruction (low ghost particle level), but as high as possible for an increase in spatial resolution to detect small scale features in the three-dimensional flame topography. Since the maximum possible seeding density for the tomographic reconstruction is a function of the depth of the desired volume, the trade-off for the current technique is between spatial resolution and the size of the volume within which the flame front is reconstructed.

The presented technique is based on a marker for the preheat zone of the flame, which has a thickness on the order of a millimeter for the lean, atmospheric methane-air flames investigated in this work. Considering a mean error of about 0.4 mm, the technique is capable of locating the preheat zone of the flame. Certain derived quantities in the study of turbulent combustion (e.g. flame displacement speed) require knowledge of the flame-front curvature. Whereas the current results suggest a good reconstruction of curvature for most portions of the reconstructed flame fronts is achieved, only the in-plane curvature can be assessed quantitatively and further work is needed to validate the accuracy of the full three-dimensional curvature of the flame topography. The current technique is not suited if the precise location of the reaction zone as opposed to the location of the preheat zone is desired or for studies interested in local extinction and re-ignition.

3.4 Velocity field validation

The velocity field is validated as it serves to improve the reconstructed particle field based on which the flame topography is determined. Furthermore, tomographic PIV is not typically applied in confined environments through curved windows close to a wall, and so the accuracy of the derived 3D velocity measurements under the challenging conditions is established next. In analogy to the flame-front validation method, slices through the volumetric velocity field are compared to two independent sets of planar velocity fields in the center plane and the near-wall plane shown in Figure 3.2. Stereoscopic PIV is performed to obtain all three-velocity vectors in the reference planes, which requires particle images from two separate views (two cameras). Consequently, two independent reference solutions are obtained for the velocity field as opposed to the planar reference flame front, which has been obtained for each of the four cameras individually. Details of the PIV processing are described in Section 3.3.

Contour plots of the velocity field of Run 2 (center plane) at one instant in time are shown in Figure 3.11. The top row shows the x-component of velocity with the middle row and the bottom row showing the y- and z-component, respectively. The left column is the result of performing stereoscopic PIV based on image pairs from camera 1 and 3 with the center column showing the results based on camera 2 and 4. The right column presents the tomographic PIV results in a slice through the volume at the location of the center plane. The flame front – marked by a red solid line – is just entering the field-of-view at this instant in time.

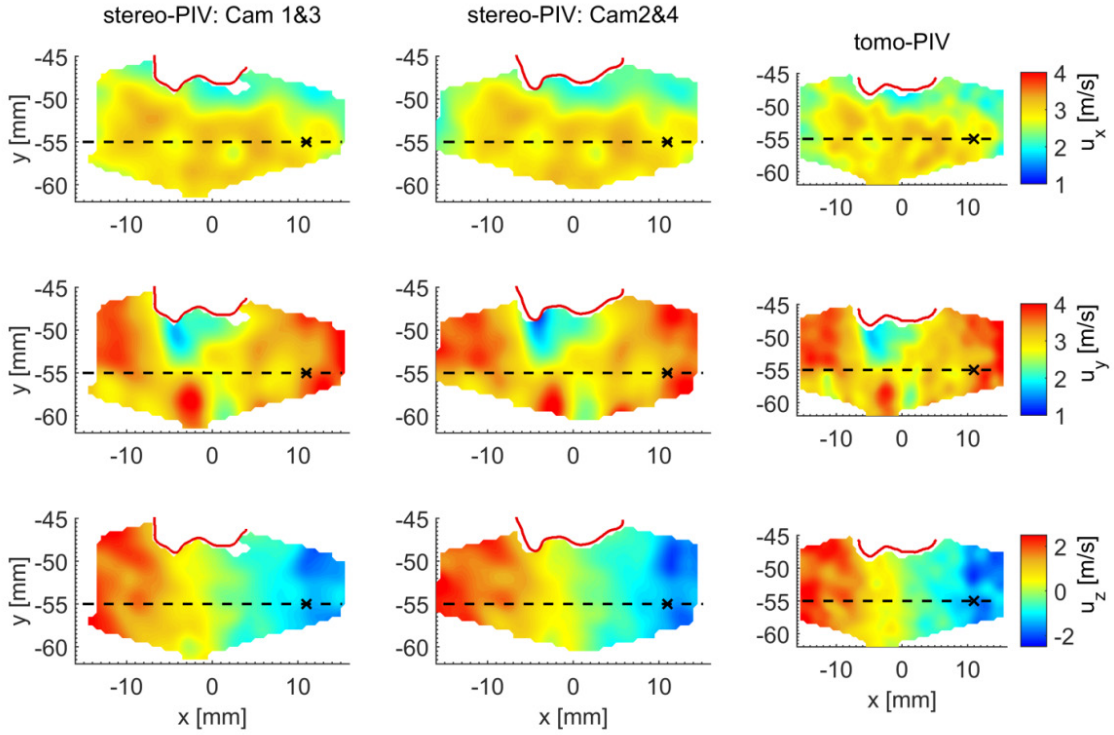

Figure 3.11: Contour plots comparing instantaneous velocity fields (rows correspond to different velocity components). Left column: stereo-PIV (cameras 1 & 3). Center column: stereo-PIV (cameras 2 & 4). Right column: tomographic PIV. Red solid line marks flame front. Black dashed line and cross mark locations for extracted profiles and time series shown in Figure 3.12 and Figure 3.13, respectively.

The two stereoscopic PIV solutions agree well both in terms of magnitudes as well as flow structures seen in all three velocity components justifying their use as a best estimate for the true solution. Note that the fields-of-view for the two camera pairs do not match exactly. The tomographic PIV results show good agreement with the stereoscopic counter parts in terms of magnitude. The majority of flow structures are also captured well. The tomographic PIV solution tends to be noisier, however, which can be

attributed to remaining ghost particles after the two iterations of MTE performed in this work (see Section 3.3. for details). Additional iterations of MTE have been tested and provided no additional improvement.

The y-component of velocity corresponds to the axial velocity in the mixing tube. The presence of the flame deflects the flow ahead of itself leading to a decrease in axial velocity as seen in all three solutions. Since the evaluated plane corresponds to a secant through the annulus, the x-component corresponds to the radial velocity at $x = 0$ mm, with the z-component corresponding to the azimuthal velocity component at this same location. At any other x-location, the x- and z-component of velocity are a combination of radial and azimuthal velocity. The flow swirls from left to right corresponding to a positive z-component in velocity in the left half of the field-of-view and a negative velocity in the right half.

Instantaneous velocity profiles along the dashed lines are shown in Figure 3.12. The two independent stereoscopic PIV results are shown in blue and red, respectively. The tomographic PIV results are shown in orange. The good agreement highlights the accuracy of the tomographic PIV results. Discrepancies primarily occur towards the edges of the field-of-view. However, small-scale outliers may exist as seen in the y-component of velocity at around $x = 0$ mm, which leads to the nosier appearance in the contour plots.

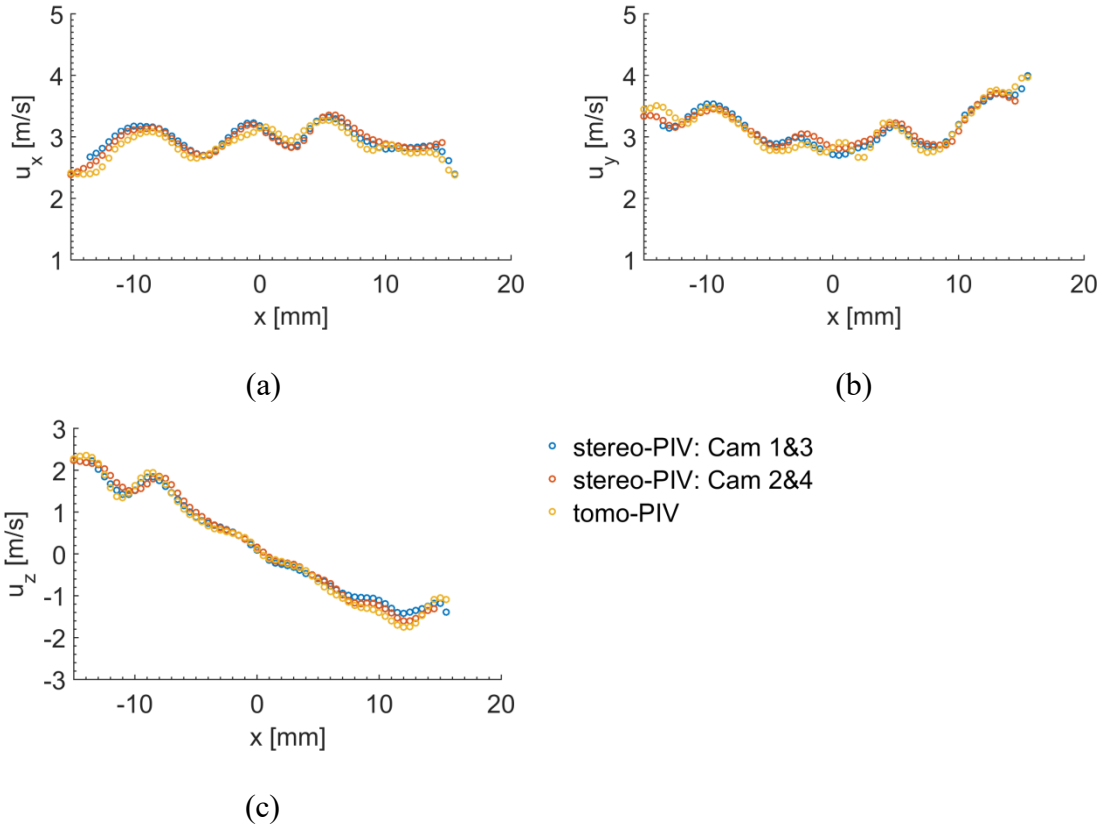

Figure 3.12: Instantaneous velocity profiles of all three velocity components along a line at y = −55 mm, z = −0.4 mm (see dashed line in Figure 3.11).

The current experiments are conducted at a temporal resolution of 5 kHz providing a velocity field every 200 µs. Time traces of velocity at an off-center location marked by the cross in Figure 3.11 are shown in Figure 3.13. Measured velocity fields obtained by means of PIV are inherently filtered in space before being digitized. The filtering is determined by the interrogation window size and weighting. In contrast, temporal filtering in high-speed PIV measurements is not possible before digitization, leading to aliasing for cases in which not all temporal scales are resolved. This is

generally the case at moderate and high Reynolds number flows like the flow studied in this work. Consequently, the temporal velocity field evolution obtained by the two stereoscopic PIV measurements shown in Figure 3.13 cannot be considered as being the true solution. However, they can be utilized as a reference for the tomographic PIV measurement, which probes the flow field at the same temporal resolution and essentially the same instants in time. The volumetric solution again compares favorably with the planar reference measurements in all three velocity components.

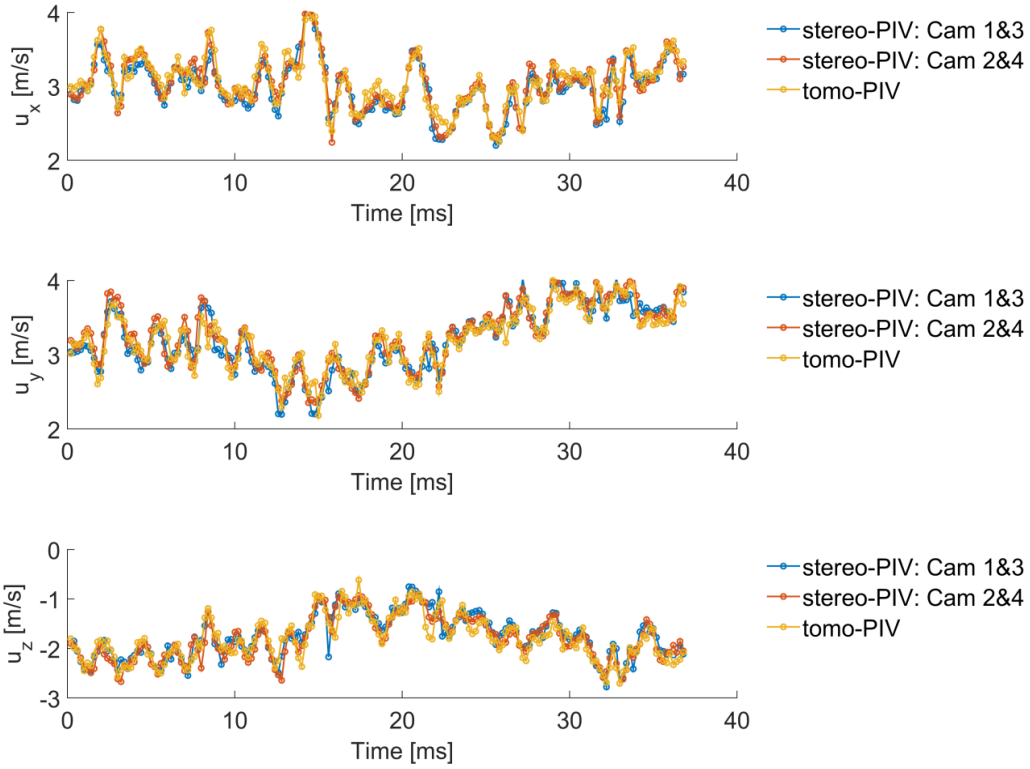

Figure 3.13: Velocity time traces of all three velocity components at point x = −55 mm, y = 11 mm, z = −0.4 mm (see cross in Figure 3.11).

At each grid point, the mean value of the two planar (stereoscopic) PIV solutions is taken as the reference solution to evaluate the accuracy of the tomographic PIV measurements. First, the discrepancy between the two planar solutions is assessed by computing the standard deviation of the difference between a solution and the mean. The resulting mean deviations for all five runs range from 0.16 – 0.25 pixels (0.05 – 0.08 m/s) for the x-component, 0.22 – 0.34 pixels (0.07 – 0.11 m/s) for the y-component and 0.28 – 0.41 pixels (0.09 – 0.13 m/s) for the z-component. The mean uncertainties associated with the random error evaluated using the correlation statistics approach [118] based on a 95% confidence interval are about 0.22, 0.28 and 0.41 pixels for the x-, y-, and z-component, respectively, which agree with the discrepancies between the two independent measurements. In contrast to the comparison between the two independently measured solutions, the presented computed uncertainties using the correlation statistics approach do not include any bias errors (e.g., due to calibration inaccuracies). The same level of uncertainty found in the measurement and the computation may therefore suggest that bias errors are small in the current measurement. The overall magnitude of the uncertainties suggests that the obtained planar velocity fields are a good estimate for the true velocity field solution and the mean value of the two can serve as a reliable reference measurement to validate the volumetric velocity field.

The error associated with the tomographic PIV measurement is defined as the standard deviation of the difference between the velocity field in a slice through the

volume and the mean of the two planar measurements in the corresponding validation plane,

$$\varepsilon_i = \left(\frac{1}{N} \sum_{j=1}^{N} (\delta_{i,j} - \mu_i)^2 \right)^{1/2} \quad with \quad \mu_i = \frac{1}{N} \sum_{j=1}^{N} \delta_{i,j}, \tag{3.1}$$

where $\delta_{i,j}$ is the difference between the tomographic PIV solution and the mean of the two stereoscopic PIV solution associated with velocity component i at grid point and time step j. The sum N is the sum over all grid points and all time steps. The errors associated with all runs and all components are listed in Table 3.2 and range from 0.50 – 0.66 voxels corresponding to 0.16 – 0.21 m/s.

A recent study investigated the accuracy of low-speed tomographic PIV experimentally by a 12-camera system [136]. An error is computed for the velocity magnitude according to

$$\varepsilon = \frac{1}{N} \sum_{j=1}^{N} \left(\frac{1}{\sqrt{2}} \left\| u_{i,j}^{Set1} - u_{i,j}^{Set2} \right\| \right), \tag{3.2}$$

based on two simultaneous uncorrelated measurements (two sets of cameras) following the derivation by [142]. The results show an error of about 0.55 voxels for a four-camera system and a particle density of 0.14 ppp (particles per pixel) with a processing algorithm comparable to the one employed in this work except that no MTE was used. The error decreases to about 0.45 voxels if a six-camera system is used. Simulations predict that employing two iterations of MTE with a four-camera system and taking five enhancement objects (five time-steps) into account increases the quality factor associated

with a measurement with 0.14 ppp to about a level of a six-camera system without MTE [111].

Run	Validation Plane	Mean Error u_x		Mean Error u_y		Mean Error u_z	
		[voxels]	[m/s]	[voxels]	[m/s]	[voxels]	[m/s]
1	Center	0.50	0.16	0.53	0.17	0.56	0.18
2	Center	0.53	0.17	0.53	0.17	0.66	0.21
3	Center	0.56	0.18	0.59	0.19	0.66	0.21
4	Near-Wall	0.53	0.17	0.50	0.16	0.59	0.19
5	Near-Wall	0.59	0.19	0.63	0.20	0.53	0.17

Table 3.2: Mean errors in volumetric velocity field for 5 different flashback events.

Computing the error associated with the current work according to Eq. (3.2), with Set 1 being the velocity field in a slice through the volume of the tomographic PIV measurement and Set 2 being the stereoscopic PIV measurement in the same plane, yields a mean error over all runs of 0.61 voxels (0.20 m/s). This level of error compares well with the investigation by Lynch et al. [136]. The error in the current work using four cameras is about 10% higher when compared to their four-camera system and, taking the previous discussion on the effect of MTE into account, about 25% higher compared to their six-camera-system. The larger errors in the current tomographic PIV measurements can be attributed to the lower signal-to-noise ratio in the raw particle images and consequently in the reconstructed particle field as well as the lower accuracy of the camera calibration. The lower signal-to-noise ratio results from the lower laser fluence available to illuminate the droplets at high-speed as well as the high background

illumination due to the nearby wall facing the cameras. Tomographic PIV requires high precision in the calibration that provides the mapping function between camera sensors and physical space [98]. In the current work, the illuminated droplets are imaged through a fused silica tube, which introduces high distortion particularly towards the edges of the field-of-view; therefore, the remaining disparity, while still sufficiently small, is about a factor of 10 higher compared to the study by Lynch et al.

An additional uncertainty is introduced by the thermophoretic effect for both the planar and the volumetric velocity measurement [122,123]. This effect is limited to the vectors evaluated in the interrogation windows and volumes, respectively, which are closest to the extracted flame front. The second closest vector is outside the influence of the thermophoretic effect owing to the spatial resolution of the measurement technique (vector spacing of 0.5 mm) and the oil droplets evaporating in the preheat zone of the flame. Nonetheless, the thermophoretic velocity, which is about 0.12 m/s for the investigated flame at the location where the oil droplets evaporate, is significant in regions where flame tongues decelerate the flow to small velocities and therefore adds a non-negligible uncertainty to the velocity vectors closest to the flame front in such regions. However, since the purpose of this work is to compare the volumetric technique to the planar technique, and the thermophoretic velocity adds to both, affected vectors may still be included in the validation.

3.5 Implications for flashback study

The presented technique is applied to study the upstream flame propagation of swirl flames inside the mixing tube of a model swirl combustor during flashback events. As an example, the measured flame topography and velocity field are shown at one instant in time in Figure 3.14. The flame surface is rendered in blue. A contour plot of axial velocity (y-component) together with velocity vectors are shown in one x-y-slice through the volume. At its closest point, this slice is offset from the center body wall by about 1.1 mm. The upstream propagating flame tongue deflects the approach flow as indicated by the dark blue region corresponding to low axial velocity. Vortical structures are visualized by iso-surfaces of the λ_2-value and colored by the z-component of vorticity. Elongated vortical structures are seen upstream of the flame tongue. The structures are oriented perpendicular to the streamwise direction and parallel to the back edge of the flame tongue.

The level of uncertainty achieved with the presented technique is suitable for studying flow-flame interactions during flashback events. The mean error of about 0.4 mm associated with the location of the flame surface as marked by the preheat zone is smaller than the flame thickness of about 1 mm for the atmospheric methane-air flame investigated in this study, which is sufficiently small if the location of the flame front in relation to large scale flow structures is of interest.

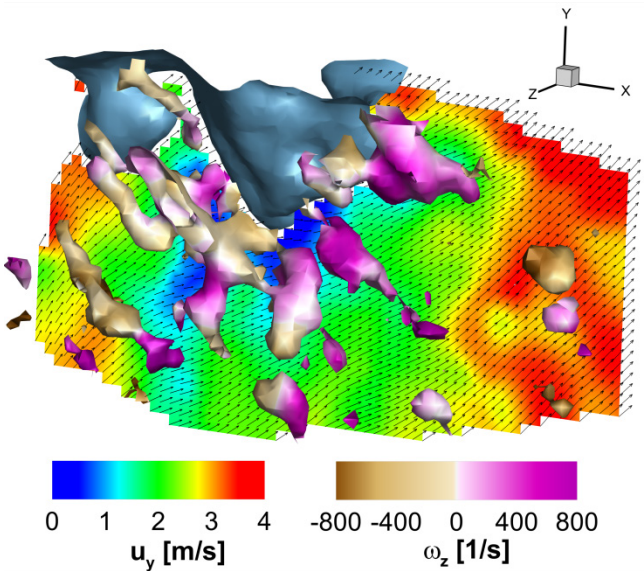

Figure 3.14: Reconstructed 3D flame front (rendered in blue) and velocity field in unburnt gas. Contour shows axial velocity field in one z-plane. 3D vortical structures are visualized by an iso-surface of λ_2 and colored by the z-component of vorticity.

The relative error associated with the volumetric velocity measurement is evaluated by dividing the absolute error at each grid point and each time step by the instantaneous absolute velocity at the same grid point and time step. The resulting errors for the velocity components are about 5-6% for the x-component, 7-10% for the y-component and 15-19% for the z-component. Note that the absolute error is about the same for all components as discussed previously and listed in Table 3.2. The larger relative error associated with the z-component is due to the central portion of the measurement volume having a z-velocity component close to 0 m/s since the measurement volume (thick sheet) is oriented tangential to the streamlines of the swirl flow in this region.

3.6 Summary

A technique to measure simultaneously the three-dimensional flame surface topography and the volumetric velocity field by means of tomographic PIV has been developed and demonstrated successfully. The technique was specifically validated for the upstream flame propagation during flashback events in the mixing tube of the employed model swirl combustor. Flashbacks of a turbulent lean-premixed methane-air swirl flame ($\phi = 0.8$) served as validation cases. The extracted flame surface corresponds to the preheat zone as marked by the vaporization of oil droplets. A number of advantages distinguish this approach from other techniques, which includes the ability for truly volumetric and truly instantaneous measurements even at kHz-rate with just four (non-intensified) cameras. In addition, the simultaneous velocity field measurement in the unburnt gas is possible without the need for additional hardware, which allows studying turbulent flow-flame interactions as opposed to just the flame front propagation. The technique is particularly appealing to study practical flames as it is robust enough to deal with light sheet refraction and image distortion due to (possibly curved) windows and high background intensities due to reflections.

The technique was validated against simultaneous planar measurements in two different slices through the volume. The reliability of the planar reference measurements was tested by conducting four and two redundant measurements for the flame front location and the velocity field, respectively. The mean error in the position of the three-dimensional flame topography was about 0.4 mm, which was smaller than the flame

thickness for the studied flame. Cusps along the flame front as small as 1 to 2 mm were found to be resolved. The mean error associated with the volumetric velocity field was about 0.6 voxels (0.2 m/s), which compares favorably with previous assessments of errors associated with tomographic PIV considering the challenges associated with the current measurement.

Chapter 4: Modes of Upstream Flame Propagation and Coupling between Flame and Approach Flow

The upstream flame propagation during flashback is investigated for a methane-air and a hydrogen-methane-air flame. The experimental conditions are described in Section 4.1. The non-reacting velocity field in the mixing tube is introduced in Section 4.2. The objective of this chapter is first to investigate how the flame propagates upstream qualitatively (Section 4.3). The shape of the flame topography and the propagation direction for two different modes of flame propagation are identified. As highlighted in Section 1.3, the nature of the velocity field ahead of the swirling propagating flame front is not well understood. The second objective is hence to measure how the propagating flame front modifies the approach flow. The results for the two different modes are presented in Section 4.4 and Section 4.5, respectively. Differences and similarities are discussed in Section 4.6. The findings presented in this chapter have been reported in [143].

4.1 Experimental conditions and diagnostic setup

Flashback is investigated at atmospheric pressure and an inlet temperature of about 293 K. In this chapter, flashbacks are primarily investigated at a bulk flow velocity of 2.5 m/s, which is dictated by the hardware (laser and cameras) available for the volumetric measurements. Planar measurements have furthermore been applied to study flashbacks at a bulk flow velocity of 5.0 m/s. Quantitative results in this chapter are based

on detailed measurements of ten methane-air flashbacks at an equivalence ratio of $\phi = 0.8$ ($s_L = 0.26$ m/s) and five hydrogen-methane-air flashbacks with 95% hydrogen by volume and matched laminar flame speed ($\phi = 0.4$). Even though the number of investigated flashbacks is limited due to the transient nature of the problem, all findings reported in this chapter are repeatedly and consistently observed without any contradicting cases. All conclusions are furthermore supported by tens of additional investigated flashbacks in preparation for the data set presented in this chapter, which were studied using similar experimental setups and moderately different conditions (flow rates, equivalence ratios, hydrogen contents).

High-speed chemiluminescence imaging (Section 2.3) is applied to study the qualitative flame propagation. High-speed planar Mie scattering and stereoscopic PIV (Section 2.2) based on olive oil droplets is applied to detect the planar flame front and measure the three-component velocity field in the unburnt gas. The field-of-view is a radial-axial plane located in the middle between swirler and mixing tube exit as shown in Figure 4.1a. The volumetric flame topography reconstruction and velocity field measurement technique presented in Chapter 3 is applied in a secant through the annulus as shown in Figure 4.1b. The back-side of the domain is offset from the center body wall by about 0.8 mm in order to prevent severe reflections off the center body as described in Section 3.1. The only difference between the experimental setup for the validation experiments presented in Chapter 3 and the measurements presented in the subsequent sections is that the field-of-

view for the measurements in this chapter was twice as large with a camera resolution of 512 x 512 pix².

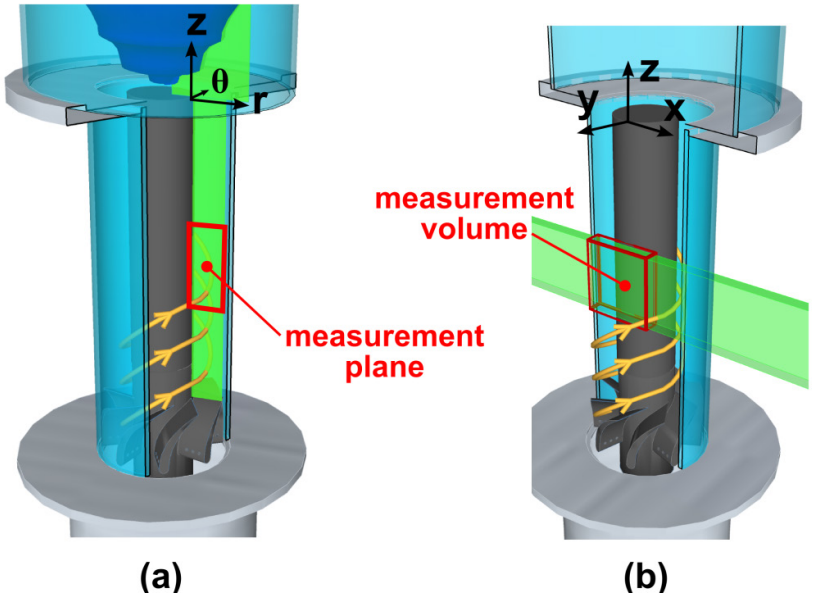

Figure 4.1: Location of the measurement domains for (a) planar and (b) volumetric measurements conducted as part of the data set presented in Chapter 4.

4.2 Non-reacting swirl flow in annular mixing tube

The bulk flow velocities of 2.5 m/s and 5.0 m/s correspond to Reynolds numbers of about Re_h = 4,000 and 8,000, respectively, based on the streamwise centerline velocity in the mixing tube annulus and the height h of the annular gap. The centerline velocity fluctuations are about 0.5 m/s and 1.0 m/s for the lower and higher Re_h, respectively, corresponding to a turbulence intensity of about 10% in each case. The non-reacting radial velocity profiles for each Reynolds number are shown in Figure 4.2. The left axis

corresponds to the location of the center body wall (r = 0 mm); the right axis to the location of the mixing tube wall. Valid velocity data was not obtained close to the outer (mixing tube) wall due to severe image distortion. The swirl flow generated in this particular model combustor is characterized by axial velocities (blue lines) that increase towards the mixing tube wall before falling off in the outer boundary layer (not seen here). The azimuthal velocity (green) peaks at about $r = 3$ mm. The peak value and subsequent fall off is prominent for the higher Re_h case. The axial and azimuthal profiles translate into a local swirl angle, defined as $tan^{-1}(u_\theta/u_z)$ (angle between mixing tube axis and streamwise velocity vector), which is plotted in red. The swirl angle is higher close to the center body wall and decreases towards the mixing tube wall. Hence, the azimuthal momentum relative to the axial momentum is higher close to the center body wall. This effect is stronger in the higher bulk flow velocity case where the swirl angle is about 65° close to the inner wall in comparison to about 55° for the lower velocity case. The radial variation of the swirl angle and the variation of swirl angle with a change in bulk flow velocity but constant swirler geometry may suggest that a fixed global swirl number based on the swirler geometry is not suited for scaling quantities like a global flame propagation speed, in which case the flame predominately experiences the swirl close to the center body wall in this configuration.

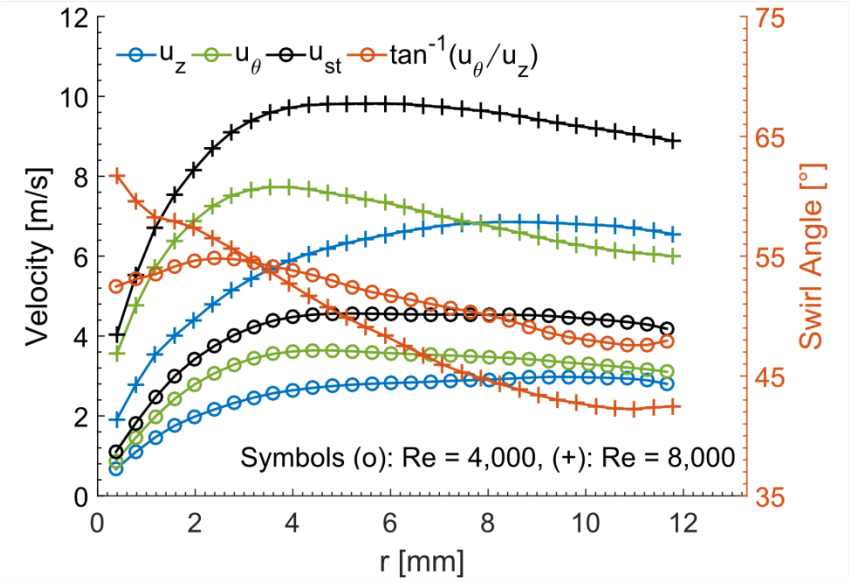

Figure 4.2: Mean non-reacting radial velocity profiles 60 mm upstream of mixing tube axis. Circles denote Re_h = 4,000 and pluses denote Re_h = 8,000 case. Axial velocity (blue), azimuthal velocity (green), streamwise velocity (black) and local swirl angle (red) are shown.

4.3 Qualitative flame shape and propagation direction

The upstream flame propagation during a flashback event is first discussed qualitatively based on high-speed chemiluminescence movies. The luminescence of a CH_4-air flame undergoing flashback at Re_h = 4,000 and ϕ = 0.7 is shown in Figure 4.3 at selected time steps taken from a movie sequence recorded at 2 kHz. The time t_0 in this case corresponds to the instant when an increase in flame luminescence is first detected visually following a step-change in equivalence ratio. This increase in luminescence immediately precedes flashback. The flow swirls in the counter-clockwise direction as indicated by the red arrows. The flame tongue leading the flashback is convected with the

bulk flow in the azimuthal direction as it propagates upstream along the center body wall (indicated by the blue arrows in the first two time steps). We use the term "flame tongue" rather than "flame front" to emphasize that the leading part of the flame is a protuberance or large bulge rather than an azimuthally-uniform flame surface. At $t_0 + 257$ ms, for instance, the flame tongue is on the back side of the center body but no portion of the flame propagates upstream on the front side. The characteristic shape of the leading flame tongues and their swirling motion in the direction of the bulk flow as they propagate upstream holds for all flames and flow rates investigated as part of this work (tens of individual flashback events). Presented chemiluminescence image sequences during flashback in a similar configuration appear to support these observations [47,51].

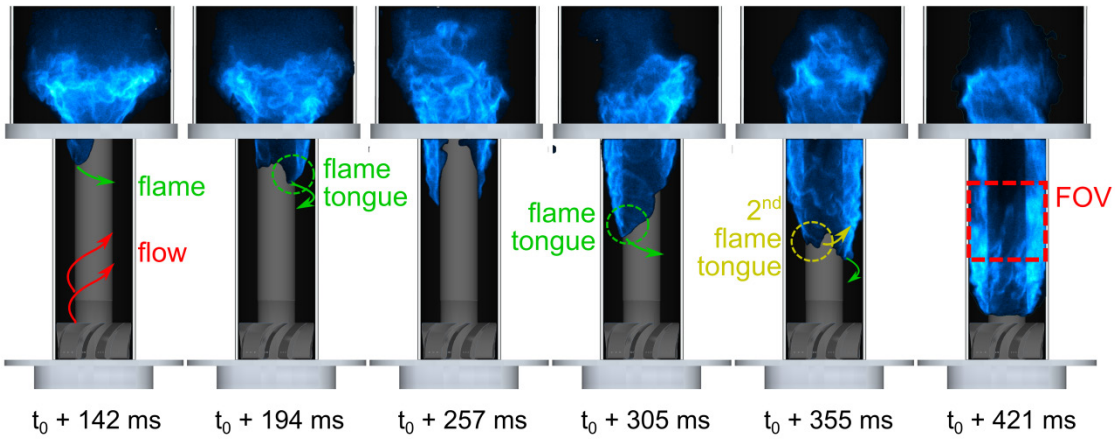

Figure 4.3: Chemiluminescence images at selected time steps of a CH_4-air flame during flashback recorded at 2 kHz.

Additional large flame tongues may form on either side of the leading flame tongue as is seen for example at $t_0 + 355$ ms where the leading flame tongue is on the right side of the center body and a secondary flame tongue has formed and swirls into the field-of-view on the left (circled with a yellow line). However, only one large flame tongue is found to prevail during flashback events under most conditions; either the originally leading one continues to lead the flashback or a newly formed one is taking over. Additional flame tongues are typically washed downstream and only coexist for longer periods of times if they form rather far away from the leading flame tongue in the azimuthal direction, which suggests that conditions are not favorable for upstream flame propagation immediately to the left or right of a leading flame tongue in agreement with the velocity field measurements discussed in Section 4.5.

The shape and propagation direction of flame tongues is investigated in more detail for a CH_4-air flame (Figure 4.4a and Video 1) and an H_2/CH_4-air flame (Figure 4.4b and Video 2). The field-of-view is shown in red in the last time step of Figure 4.3. We focus on a region about half way down the mixing tube to investigate the sustained upstream flame propagation in a region where the flow field is not affected by geometry-dependent mixing tube entry or exit effects. In Figure 4.4a and Figure 4.4b, at time t_1, the leading flame tongue is swirling around the center body into the field-of-view as indicated by the green arrow. The nominal flow direction is indicated by the red arrow. The edges of the center body are outlined by the vertical grey lines. We again refer to the rather large portion of the flame that is leading the flashback as a flame tongue as

indicated for both flames at time t_2. In contrast, we refer to smaller structures along the flame front as flame bulges. Such flame bulges tend to form on the trailing side of the flame tongue. Flame tongues and flame bulges, as defined in this work, may be differentiated quantitatively in terms of their size (width or radius of curvature), which differs by an order-of-magnitude. Flame tongues have a characteristic size on the order of the geometry of the mixing tube (diameter of the center body or 20-30 mm) since they describe the asymmetry of the overall flame front along the circumference of the center body. Instead, flame bulges have a characteristic width on the order of 2 to 3 mm and are hence comparable in size with the measured integral scale of turbulent structures in the investigated flow.

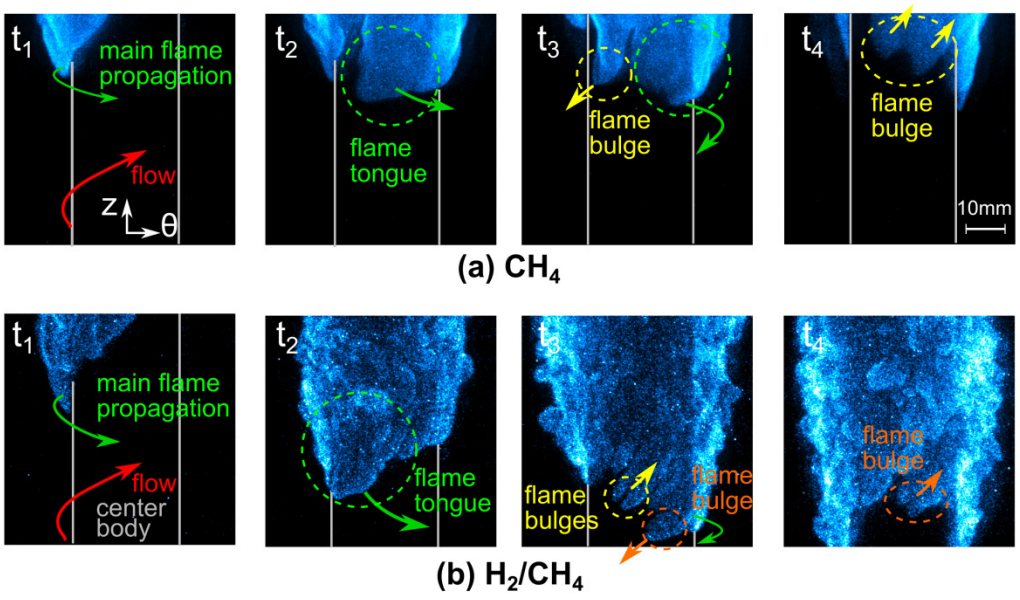

Figure 4.4: Chemiluminescence image sequence showing the upstream flame propagation and flame structure of a CH_4-air flame (a) and a H_2/CH_4-air flame (b) in the field-of-view marked in Figure 4.3. Corresponding movies are Video 1 and Video 2 in Appendix A.

In the case of the methane flame ($\phi = 0.8$), flame bulges form occasionally with an example seen in Figure 4.4a at time step t_3 and highlighted by the yellow dashed circle. This bulge attempts to propagate upstream in the negative streamwise direction as indicated by the yellow arrow and manages to momentarily resist the approach flow – it remains at a fixed location in space for about 3 ms – while the tip of the leading flame tongue continues to swirl upstream (green arrow). However, the bulge then breaks into two smaller bulges – likely due to the arrival of a faster moving flow structure – and is convected downstream as seen 6.25 ms later at time t_4. While the flame bulge fails to initiate sustained upstream flame propagation, the tip of the leading flame tongue continues to swirl upstream as indicated by the green arrows at time steps t_2 and t_3. By time step t_4 it is on the back side of the center body.

The H_2/CH_4-air flame (95% hydrogen by volume, $\phi = 0.4$) shown in Figure 4.4b has the same laminar flame speed but a significantly lower flame temperature as the previously discussed methane flame and features a more convoluted flame surface, which may be attributed to thermo-diffusive effects [5]. The overall shape of the flame during flashback, however, is again characterized by a large flame tongue leading the flashback as seen at times steps t_1 and t_2. The formation of small-scale bulges located on the trailing side of the leading flame tongue and aligned with the nominal streamwise direction are more frequently observed for high-hydrogen content flames compared to the previously discussed methane flames. Furthermore, the bulges are smaller in size and do not just

resist the approach flow (freeze at a fixed location in space), but sometimes even counter-propagate into the approach flow for short distances (~1 mm), which may be attributed to a smaller quenching distance and an increase in flame speed at the tip of these convex shaped bulges owing to local enrichment effects of the deficient reactants. Based on the full movie sequence (Video 2 in Appendix A), the two bulges marked by the yellow circle at time step t_3 are being convected downstream whereas the bulge marked by the orange circle manages to counter-propagate into the approach flow for a short time (~1 ms) and distance. About 11 ms later (time step t_4), this same bulge is seen (again marked by an orange circle), but now broken into two separate bulges and again washed downstream as indicated by the small orange arrow. All the while, the tip of the flame tongue leading the flashback continues to swirl upstream; it is already on the right side of the center body at t_3 (indicated by the green arrow) and on the back side below the bottom edge of the field-of-view at t_4.

The formation and break-up of the small-scale bulges on the trailing side of the leading flame tongue, particularly for the H_2/CH_4-air case, agree well in size and occurrence with the observations reported by Eichler et al. [24] investigating flashback in a (non-swirling) channel flow. This is reasonable as the trailing sides of the swirling flame tongues observed in the current work are aligned approximately perpendicular to the streamlines of the approach flow just like in a channel flashback where the flame brush is oriented perpendicular to the flow. However, the contribution of these flame bulges to facilitate the overall flashback is different. In a channel boundary layer

flashback, a combination of parameters likely to include flame speed, quenching distance and density ratio (the relative importance of each of these factors is not yet fully understood) has to be above a particular threshold such that the formation, upstream propagation, break-up and downstream convection of these small-scale bulges leads to a net upstream propagation of the entire flame brush. The requirement for the flame to achieve overall flashback in a swirl flow is different, however. Instead of fighting the approach flow head-on in form of small-scale bulges, the flame is found to flashback in the form of large-scale flame tongues swirling upstream, which appears to be the path of least resistance for the flame even when flashback was triggered at an equivalence ratio significantly beyond the flashback limit.

In summary, we consistently observe two modes of upstream flame propagation during boundary layer flashback in swirl flows. The first mode consists of large-scale flame tongues swirling in the direction of the bulk flow as they propagate upstream. The second mode concerns small-scale flame bulges aligned with the streamwise direction, which – particularly for high-hydrogen-content flames – resist the approach flow head-on and counter-propagate into the negative streamwise direction for short distances (~ 1 mm) but do not provide net upstream flame propagation on their own. The first and second mode will be investigated in more detail in Sections 4.5 and 4.4, respectively, by discussing the velocity field in the vicinity of the flame front associated with each mode.

4.4 Flame propagation associated with small-scale bulges

The velocity field upstream of small-scale bulges is compared with non-swirling channel flashback results by Eichler et al. [24] and Gruber et al. [25] to provide evidence that the same mechanism facilities the upstream flame propagation associated with such bulges in the investigated swirl flow as suggested qualitatively by the time-resolved chemiluminescence imaging discussed in Section 4.3. The chemiluminescence image sequence in Figure 4.5 shows the formation of a small-scale bulge on the trailing side of a flame tongue during a CH_4-air flame flashback ($\phi = 0.8$). Results from the volumetric velocity field measurement corresponding to an instant in time when the flame bulge resists the approach flow (the local displacement speed matches the flow velocity) is shown in Figure 4.5a. The three-dimensional flame front topography based on the marker for the preheat zone is shown in grey. The axial velocity field is shown in a secant through the annulus, which is offset from the center body by about 0.8 mm at its closest point as described in Section 4.1. The white band separates positive from negative axial velocity with the region of negative axial velocity colored in blue. A reverse flow pocket, marked by the black solid line corresponding to zero streamwise velocity, exists in agreement with previous studies [24,25]. Three-dimensional streamlines are plotted and color coded by the y-distance to indicate their location in the depth direction as indicated in Figure 4.5c, which is a bottom view of Figure 4.5a highlighting again the location of the measurement volume in relation to the center body with the back side of the measurement domain slightly offset from the center body wall.

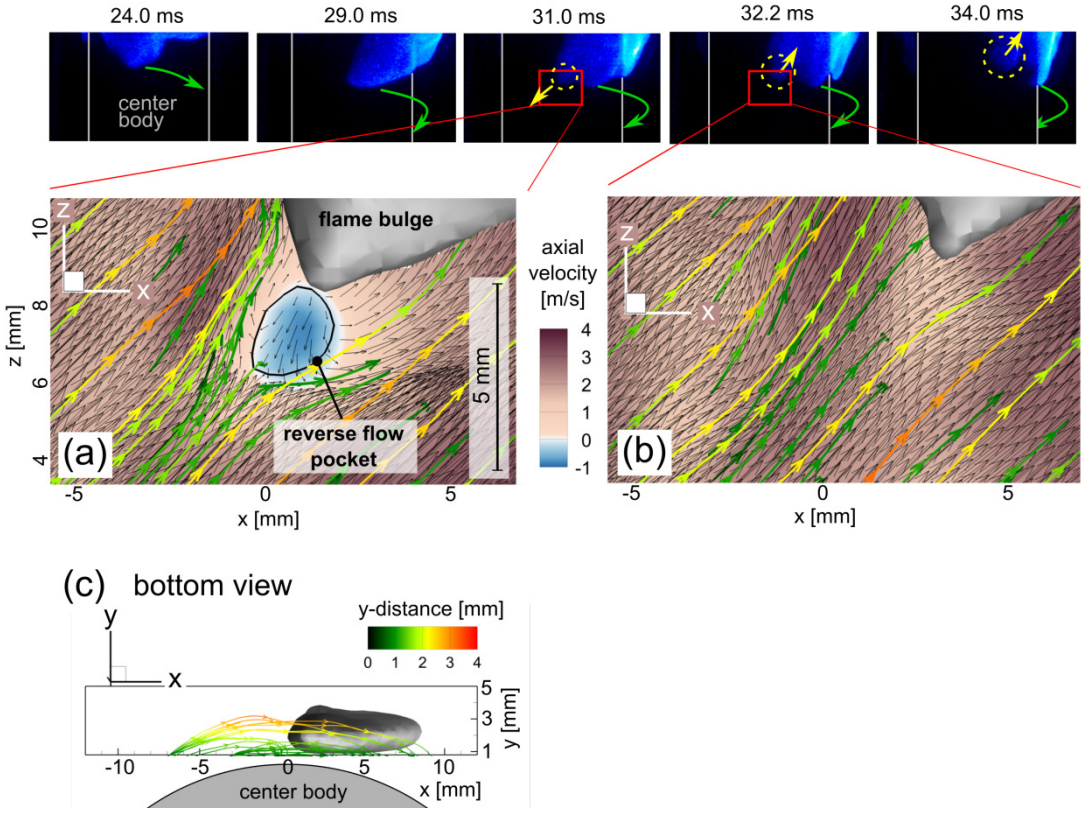

Figure 4.5: Formation of a small-scale flame bulge on the trailing side of a flame tongue (luminescence image sequence, top row). Axial velocity field in $y = 0.8$ mm plane and 3D streamlines showing (a) the reverse flow pocket associated with the flame bulge as it resists the approach flow and (b) the recovered flow field subsequently convecting the bulge downstream. Streamlines are colored by y-distance from the center body as explained in (c). The flame surface rendered in grey corresponds to an isotherm of about 555 K.

Flame bulges locally push the low-momentum near-wall fluid upstream in the negative streamwise direction, which leads to a stagnation point at the upstream end of the reverse flow pocket. The near-wall streamlines (green) diverge symmetrically to either side of the flame bulge. Streamlines farther offset from the wall (yellow and orange) still diverge but to a lesser extent. The agreement in the velocity field with the

DNS results by Gruber et al. suggests that the propagation mechanism associated with these small-scale bulges is indeed the same. The DNS was further able to show that the reverse flow pockets are associated with a localized pressure peak ahead of the convex shaped bulges whereas the pressure drops downstream of the flame brush. The location where convex shaped bulges form was found to be correlated with the occurrence of low-momentum streaks [25] as previously suggested by Eichler et al. [24]. It appears that in the investigated swirl flow the formation of small-scale bulges is also linked to the arrival of low-momentum fluid either due to low-momentum streaks in the boundary layer or due to wake effects originating from the swirler vanes. However, since we cannot measure the velocity along the circumference of the center body but only in a tangent or wall-normal plane, we cannot establish the correlation with certainty. As described before, small-scale bulges are found not to sustain in the investigated swirl flow and are washed downstream shortly after their formation as shown in Figure 4.5b.

4.5 Flame propagation associated with large flame tongues in swirl flows

4.5.1 Region of negative axial velocity

Regions of negative axial velocity upstream of the leading flame front have first been observed by Heeger et al. [48] in a similar swirl burner configuration featuring a mixing tube with center body along which the flame propagates during flashback. The planar two-component velocity field in a radial-axial slice was measured in their work while simultaneously recording the flame luminescence from a point-of-view

perpendicular to the planar measurement domain. Apparent upstream propagation without negative axial velocity was observed in about half of the recorded cases. The possibility that such cases correspond to instances when the laser sheet slices through the leading or trailing side of a flame tongue rather than the leading tip was suggested.

Our measurements consistently show that upstream propagation without a negative axial velocity region is an artifact associated with a planar measurement in a 3D flow in agreement with the suggestion by Heeger et al. As an example, a few selected time steps of a methane-air flashback ($\phi = 0.8$) movie are shown in Figure 4.6. The luminescence is shown in the top row with arrows indicating the nominal flow direction and the flame propagation direction as well as the PIV measurement domain (green vertical line). The corresponding velocity fields are shown in the bottom row with the grey vertical bar on the left indicating the location of the center body wall and the red line indicating the flame front (based on the employed marker for the preheat zone). The planar velocity field and flame front location measurement by itself would suggest that flashback is characterized by an initial flame propagation away from the wall (Figure 4.6b) followed by flame propagation along the wall without a region of negative axial velocity upstream of the flame base (Figure 4.6c) and finally upstream flame propagation with a region of negative axial velocity (Figure 4.6d). In contrast, the flame luminescence reveals that the apparent upstream propagation is instead a swirling motion as previously discussed where the flame is behind the center body in Figure 4.6a and the measurement slices through a downstream portion of the flame in Figure 4.6b and Figure 4.6c. Only

Figure 4.6d corresponds to a time step when the flame tip is in the planar field-of-view. We confirmed all findings just discussed based on planar measurements with high-speed volumetric measurements to be discussed in the subsequent sections. Studying certain aspects of the three-dimensional flame-flow interaction during swirl flame flashback is therefore possible if some means to unambiguously interpret the planar data is available such as luminescence imaging from a perpendicular point-of-view in this case. True upstream propagation of the leading flame tip is found always to be associated with a region of negative axial velocity ahead of the flame tip for all conditions and all runs conducted as part of the present work.

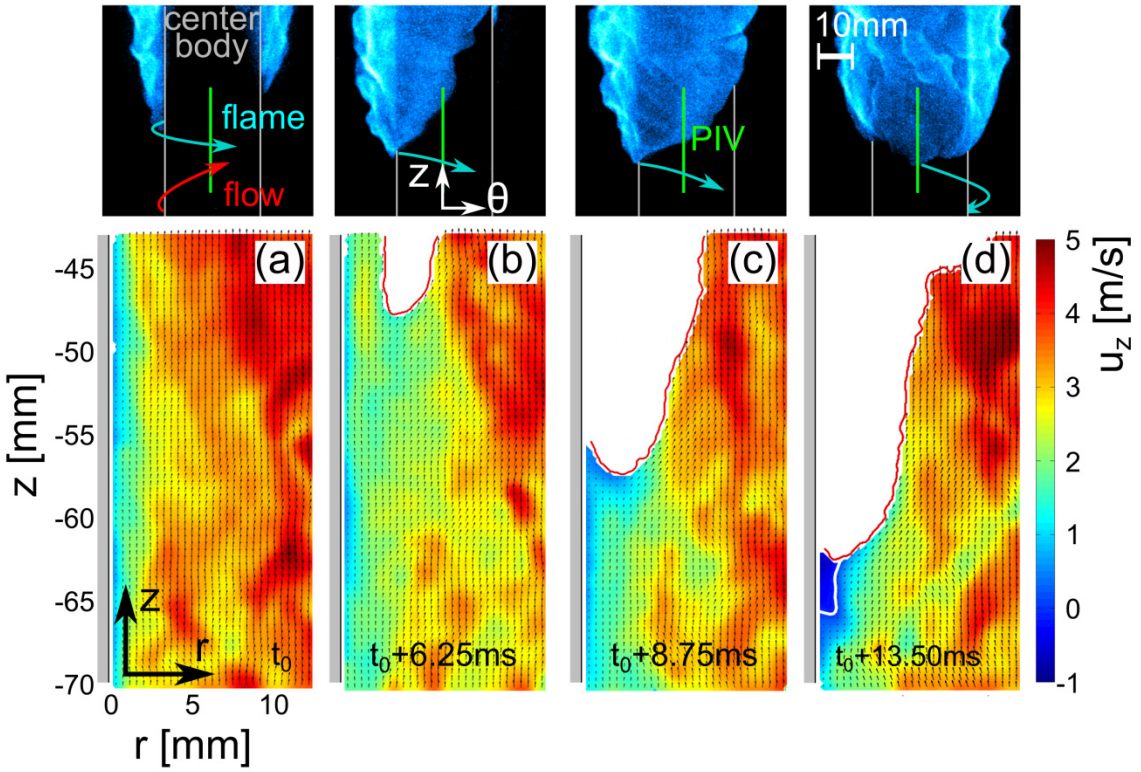

Figure 4.6: Simultaneous chemiluminescence (top row) and velocity field measurement (bottom row) highlighting the difference between apparent and true upstream flame propagation and its correlation with a region of negative axial velocity. The planar flame front (red line) and axial velocity field is shown in a radial-axial slice corresponding to the green line in the luminescence images. The white line in (d) is an isoline of 0 m/s indicating the region of negative axial velocity.

The region of negative axial velocity upstream of the leading flame tongue is found to exist not only immediately at the flame tip but also on its leading side corresponding to the fluid region the flame is propagating into as shown in Figure 4.7a. On the leading side of the flame tongue negative axial velocity is observed in the near vicinity of the flame front only. In contrast, the region of negative axial velocity reaches

far upstream in the vicinity of the flame tip as shown in Figure 4.7b. The negative axial velocity region is about 5 to 10 mm in extent based on observations from ten flashback events. This observation of the extent of negative axial velocity holds even for more turbulent conditions (twice the bulk flow velocity corresponding to Re_h = 8,000).

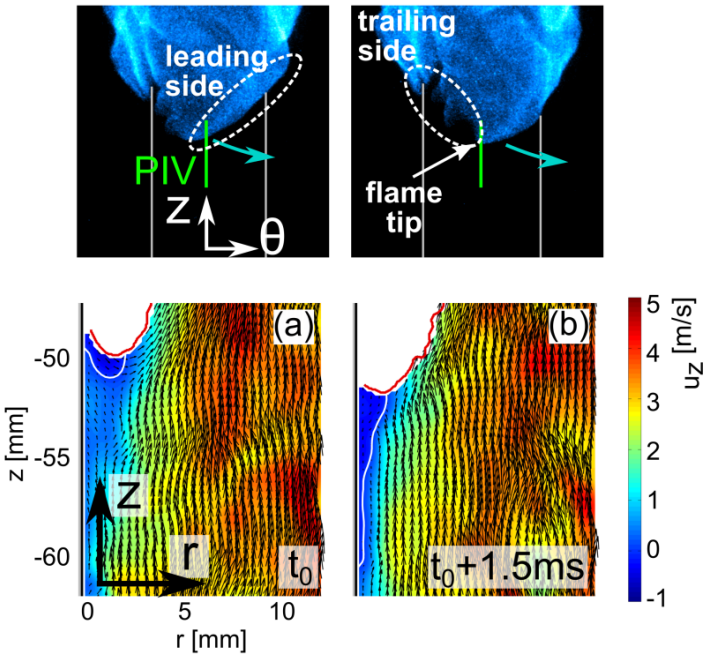

Figure 4.7: Velocity field and region of negative axial velocity (white line) in the vicinity of the leading flame front (red line) in a slice through the leading side of the flame tongue (a) and through the flame tip (b).

As discussed in Section 4.3, the investigated H_2/CH_4-air flames (95% hydrogen by volume, $\phi = 0.4$) are found to be more convoluted as a result of small-scale bulges, which form more frequently compared to the methane-air flames. However, focusing on the similarities in this chapter, the upstream flame propagation again occurs in the form of larger flame tongues. The velocity measurements show regions of negative axial

velocity upstream of the leading flame tongue, which compare well with the findings in methane-air flames. The observed axial extent of the negative axial velocity region appear to be smaller (about 5 mm), but a wider range of conditions would need to be tested before more general conclusions can be drawn.

4.5.2 Three-dimensional velocity field in the vicinity of leading flame tongues

The volumetric velocity field in the vicinity of flame tongues, which dominate boundary layer flashback in the investigated swirl flames, is shown in Figure 4.8. The axial velocity field is seen in a secant through the annulus, as shown in Figure 4.1, which is offset from the center body by about 0.8 mm. The blue colored region bounded by the white band shows a region of negative axial velocity. The color coding for the three-dimensional streamlines follows Figure 4.5c indicating the *y*-distance from the center body. The chosen instant in time captures the tip of a larger flame tongue that is swirling with the bulk flow velocity in the counter-clockwise direction as it propagates in the negative axial direction, which corresponds to the flame motion found to lead flashback in the investigated swirl flames. The velocity field is fundamentally different compared to the velocity field upstream of small-scale bulges as presented in Figure 4.5. The region of negative axial velocity is merely the result of a rather large-scale deflection of streamlines as opposed to a localized reverse flow pocket, which is emphasized by the near-wall streamlines (green) deflected around the tip of the flame tongue without being reversed. The azimuthal velocity component remains large upstream of the flame tongue

in contrast to the reverse flow pockets which are the results of both negative axial and negative azimuthal velocity. Note that we define “reverse flow” as a region with fluid that flows counter to the dominant upstream flow direction. In the case of a swirling flow, reverse flow propagates in the negative swirl direction. A moderate level of deflection of streamlines in the investigated swirl flow is sufficient to result in a region with a negative axial component, but without flow reversal.

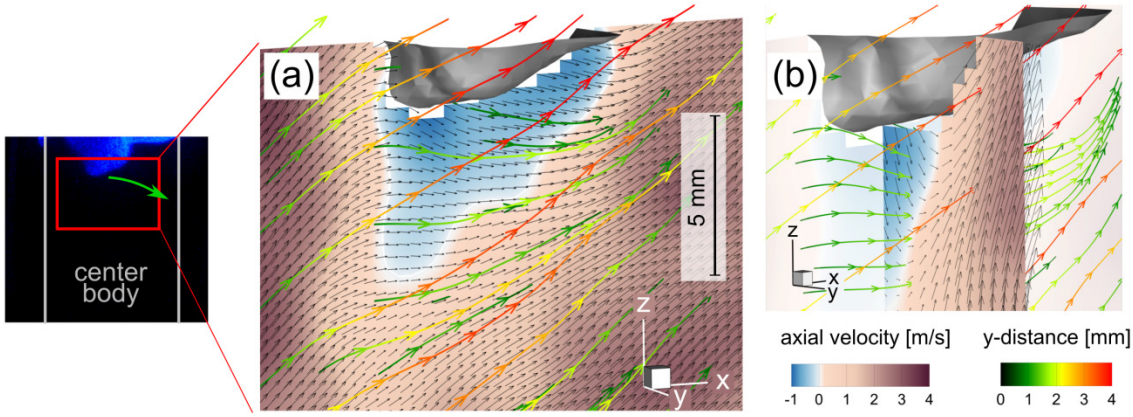

Figure 4.8: Three-dimensional velocity field associated with flame tongues (grey surface): (a) Axial velocity field in $y = 0.8$ mm plane and 3D streamlines. (b) Velocity field in $x = 0$ plane. Shown here: CH_4-air flame ($\phi = 0.8$).

The velocity field is shown in a perpendicular plane in Figure 4.8b, which corresponds to a radial-axial slice typically measured with a planar technique as presented previously in Figure 4.6 and Figure 4.7. The tangent vectors suggest flow recirculation, which has been interpreted as boundary layer separation in previous works [48]. However, neither flow recirculation nor boundary layer separation occurs upstream of the preheat zone in this case as the volumetric measurements reveal. Furthermore, the

location where the velocity vectors switch from a positive to a negative axial component at the upstream end of the negative axial velocity region is not a stagnation point but instead corresponds to purely swirling flow.

The volumetric measurement readily provides the explanation for the difference in characteristic shape and axial extend of the negative axial velocity region between the leading side of the flame tongue and at the flame tip as observed previously in planar measurements shown in Figure 4.7. Instead of diverging to either side of the flame tongue, the flow is deflected downwards ahead of the flame tongue as well as alongside the leading side of the flame tongue, hence providing a region of negative axial velocity for the flame to propagate into.

Fluid farther out in the radial direction is only moderately deflected in the axial direction as the streamlines colored in red indicate (Figure 4.8). A shear layer forms between the near-wall layer of fluid with a predominantly swirling motion and fluid away from the wall moving at a swirl angle closer to the nominal angle and hence with a significant axial component. The shear layer consists of negative azimuthal vorticity, which may also be measured with planar PIV in a radial-axial slice as shown in Figure 4.9 and Video 3. The red line marks the location of the flame front. The grey vertical line along the left edge indicates the location of the center body wall. The shear layer is indicated by the dashed black line. Figure 4.9a corresponds to the time step shown in Figure 4.7a, at which the leading side of the flame tongue is in the field of view. Negative azimuthal vorticity is concentrated in the near vicinity of the flame front. The flame

continues to swirl into the measurement plane, which is associated with shear appearing farther upstream of the flame. Figure 4.9d corresponds to the instant in time shown in Figure 4.7b when the laser sheet cuts through the flame tip. At this time, a strong shear layer exists between the near-wall fluid with a negative axial velocity and fluid moving in the positive axial direction farther away from the wall.

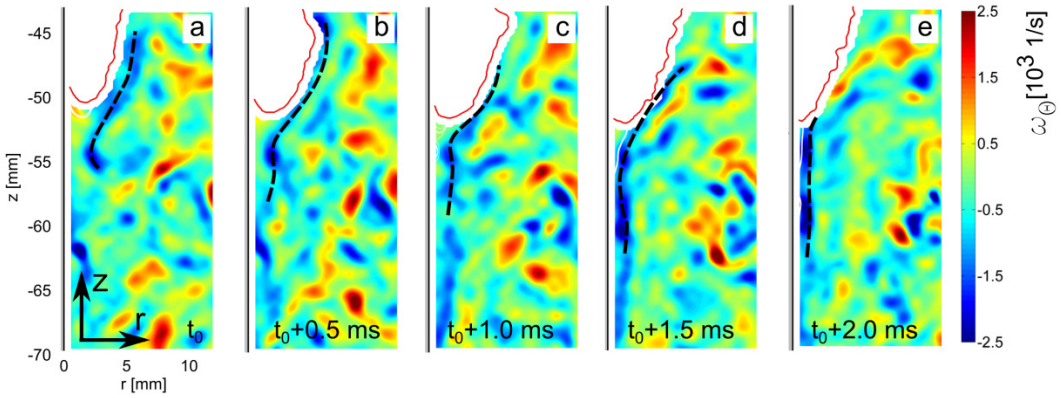

Figure 4.9: Azimuthal vorticity field in a radial-axial slice in the vicinity of a flame tongue (red line marks flame front) leading flashback. The black dashed line highlights a layer of vorticity moving coherently based on the movie sequence (see Video 3 in Appendix A).

The production of negative azimuthal vorticity at the flame tip due to baroclinic torque, which results from the axial density gradient across the flame tip and the radial pressure gradient due to the swirl flow, has been proposed as a mechanism enhancing the flame speed along a vortex axis [45]. The concept of vorticity produced by baroclinic torque and inducing a negative axial velocity has subsequently been identified as a mechanism driving flashback in the core of swirl flows associated with combustors not featuring a center body in the mixing tube [41–43]. The measurements in the present

work suggest that in *boundary layer* flashback of swirl flames the observed negative azimuthal vorticity present in the immediate vicinity of the flame tip is part of a larger coherent shear layer, which reaches far upstream into the cold approach flow and hence is not dominated by vorticity production due to baroclinic torque. Hence, the data suggest that the observed azimuthal vorticity is not the cause but an effect of the upstream flame propagation. The observed concentration of elevated azimuthal vorticity may be the result of already existing boundary layer vorticity, which is being reoriented and transported away from the wall by the modified flow field in the vicinity of the leading flame tip. Additional vorticity may possibly be produced at the center body wall due to a pressure gradient induced by the presence of the flame tongue.

4.5.3 Region of influence of the local blockage effect

As described in the previous section and highlighted in Figure 4.8, flame tongues decelerate and deflect the approach flow. The effect flame tongues have on the approach flow may hence be described as a blockage effect due to the gas dilatation associated with the heat release. It is instructive to investigate where and how the velocity field is influenced at various points relative to a flame tongue. For that purpose time traces of axial velocity, azimuthal velocity and swirl angle (angle between the axial direction and the instantaneous, local streamwise flow direction) are evaluated at two points in space as shown in Figure 4.10. Both points are located at the same axial location as marked by a white cross in the sequence of chemiluminescence images shown in Figure 4.10a, which

provides the flame location in relation to the measurement points. The instantaneous velocity evolution (thin lines) are low-pass filtered (thick lines) to highlight trends due to the presence of the flame as opposed to turbulent fluctuations.

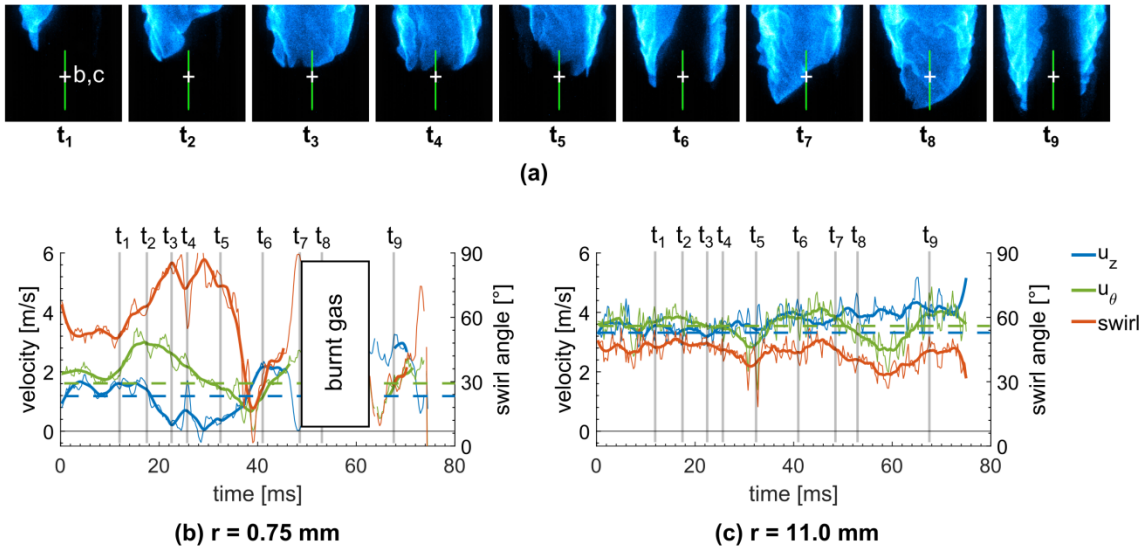

Figure 4.10: Time traces of axial velocity (blue), azimuthal velocity (green) and swirl angle (red) at two radial locations (b) in the boundary layer close to the center body and (c) close to the mixing tube wall, respectively. Mean velocities are marked by horizontal dashed lines. The global flame position in relation to the measurement points (white cross, same axial location) is shown in (a) at nine instants in time.

We first discuss the velocity evolution at the measurement point close to the center body wall (Figure 4.10b). As the flame tongue swirls through the laser plane the approach flow is decelerated starting at time t_2 and subsequently recovers again starting around time t_5 indicating that the presumed elevated pressure causing the flow deflection is limited to the portion of the annulus occupied by a flame tongue. Interestingly, the cusp

between the leading flame tongue and a secondary flame tongue is associated with the immediate spike in axial velocity at time t_4. The flame tongue furthermore accelerates the azimuthal velocity on its leading side (time t_2) and decelerates it on its trailing side (time t_6). The same acceleration and deceleration is observed rather far downstream of the leading flame tip. At time t_7, immediately before the flame front arrives, the azimuthal velocity is high. In contrast, the azimuthal velocity is low between the time the trailing side of the flame tongue passes through and t_9. These observations suggest that the presumed region of elevated pressure is not limited to the immediate vicinity of the leading flame tip. The described velocity pattern leads to predominantly swirling motion of the near-wall fluid ahead of the flame tongue (swirl angle of about 90° between times t_2 and t_5) and a primarily axial fluid motion on the opposite side of the flame tongue. The low swirl and high axial velocity around times t_6 and t_9 indicates a reliving effect away from the flame tongue.

The second measurement point is close to the mixing tube wall and outside the burnt gas for all times show in Figure 4.10c. The decrease in azimuthal velocity starting around times t_5 and t_8 indicate the blockage effect of the flame tongue affects the flow close to the center body wall but also the incoming swirl flow beyond the radial portion occupied by burnt gas. The steady increase in axial velocity relative to the mean velocity (dashed line) close to the outer wall as the flame tongue swirls upstream further indicates an additional relieving affect for the unburnt gas. It appears that the path of least

resistance for the flame to flashback is not to block the flow in the entire annulus or even transiently back-pressurize the entire flow, but only locally ahead of flame tongues.

A recent study was able to measure a static pressure rise on the center body wall inside the burnt gas region of a flame tongue swirling past the measurement port [51]. The present velocity field measurements further suggest that this increase in pressure is not limited to a region close to the center body wall and in addition has a magnitude capable of causing a time-rate-of-change in momentum associated with the changes in the velocity field just discussed.

4.6 Differences and similarities of propagation modes

Evidence for the existence of two different modes of upstream flame propagation along a wall during swirl flame boundary layer flashback has been presented. We now want to summarize the important features associated with each mode of flame propagation and discuss similarities as well as differences. The first mode consists of large-scale flame tongues swirling in the bulk flow direction as they propagate in the negative axial direction along the center body wall as discussed in Section 4.5. and summarized in Figure 4.11a. This form of flame propagation is found to lead swirl-flame boundary-layer flashback under the conditions investigated in the present work. The second mode consists of small-scale bulges aligned with the streamwise direction, which may counter-propagate into the approach flow as described in Section 4.4 and summarized in Figure 4.11b.

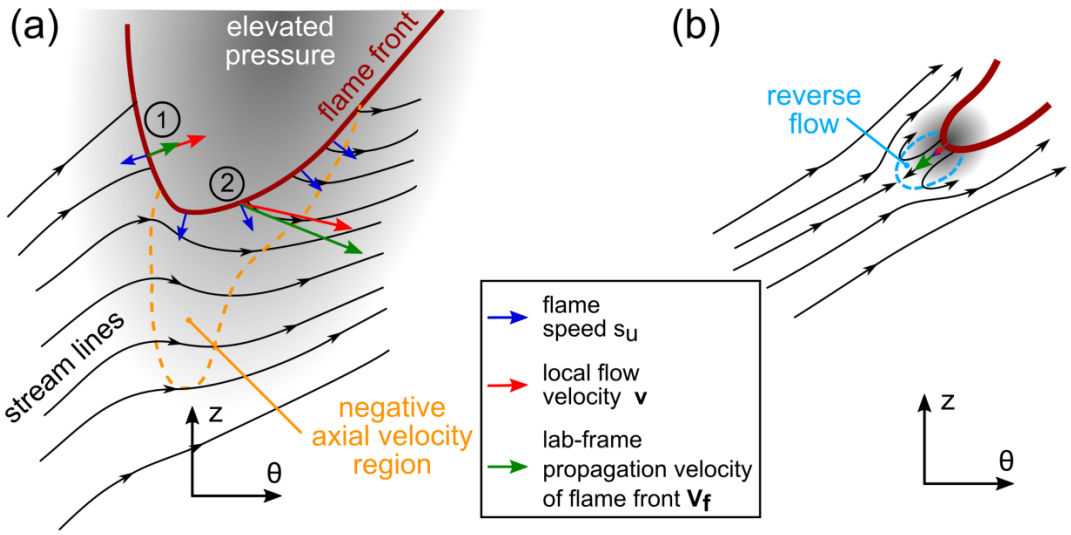

Figure 4.11: Schematics summarizing flame shape, flame propagation direction and important flow features associated with (a) flame tongues leading boundary layer flashback in swirl flows and (b) flame bulges counter-propagating into the approach flow on the trailing side of flame tongues.

Boundary layer flashback in non-swirling channel flows has been found to be driven by small-scale bulges, which are correlated with the arrival of low-momentum streaks in the turbulent boundary layer [24,25]. Interestingly, we find that the formation of small-scale bulges in the investigated swirl flow is only observed on the trailing side of the larger flame tongues where the flame surface is oriented perpendicular to the streamwise flow direction and hence provides the same alignment as in a 2D flow. The formation on the trailing side is likely assisted by the overall deceleration of the flow in that region due to the flame tongue itself. The formation, counter-propagation, break-up and downstream convection of small-scale bulges leads to a net upstream propagation of

the flame brush in the negative streamwise direction in a channel flashback [24], which is not the case for the conditions investigated in the present work as described in Section 4.3 and Section 4.5. In contrast, the large flame tongues leading flashback in the investigated model swirl combustor do not depend on the arrival of low-momentum fluid, which leads to a continuous, rather than intermittent, upstream propagation of the leading flame tip. The bulges may nonetheless contribute to flashback by additionally modifying the approach flow in the vicinity of the flame tip at occasions when they are formed at the tip of the flame tongue. Furthermore, they may modify the rate at which reactants are consumed by the flame tongue by increasing the flame surface area. Whether the consumption rate and hence the rate at which low density burnt gas is generated (generation of volume) is a dominant effect for the flashback mechanism requires further investigations, however.

Both modes of flame propagation are coupled with the velocity field through the pressure field. Both propagation modes lead to a region of negative axial velocity ahead of the leading flame tip and hence enable flashback by strongly modifying the approach flow. However, the region of negative axial velocity is the result of a different underlying velocity field. In the case of flame tongues, the approach flow is deflected in the negative axial direction as indicated by the streamlines in Figure 4.11a such that a predominantly swirling fluid motion with a small negative axial component exists upstream of the flame tip. No stagnation point exists upstream of the preheat zone in this case. As discussed in Section 4.5.3, the velocity field is modified far upstream and downstream of the leading

flame tip as well as beyond the burnt gas region in the radial direction, which suggests that a large portion of the burnt gas is associated with elevated pressure as indicated by the grey area in Figure 4.11a. In contrast, the region of negative axial velocity upstream of small-scale bulges is the result of flow reversal in a small pocket ahead of the convex shaped flame tip with a stagnation point at its upstream end as sketched in Figure 4.11b. The DNS has shown that the elevated pressure is restricted to the immediate vicinity of the tip of convex bulges and subsequently decreases in the burnt gas [25], which is indicated by the grey spot in Figure 4.11b.

The newly found velocity field associated with flame tongues causing the observed flame propagation during swirl-flame flashback is summarized in more detail based on two locations along the flame front, positions 1 and 2, in Figure 4.11a. The azimuthal velocity is decreased on the trailing side of the flame tongue corresponding to a decrease in azimuthal momentum of the approach flow as indicated by the red arrow at position 1. In contrast, the azimuthal velocity is increased towards the leading side (position 2) suggesting the flame tongue is pushing the flow ahead of itself. The red arrows are drawn to scale based on the velocity field measurement. The axial velocity along the leading side is found to be negative or at least significantly decelerated even far downstream of the flame tip. The displacement speed associated with the flame front is indicated by blue arrows assuming a flame speed of 0.7 m/s. The vector sum of local flow velocity and flame speed is indicated by the green arrows providing the propagation direction and speed of a local flame front element. The discrepancy in the azimuthal

flame front propagation velocity between position 1 and 2 leads to the characteristic spreading of the flame tongue in the azimuthal direction with downstream distance. The positive axial component on the trailing side indicates that flame front elements are convected downstream in agreement with the high-speed chemiluminescence movies discussed in Section 4.3, which show structures along this side of the flame tongue being convected downstream by the flow. In contrast, the leading side of the flame tongue continuously propagates into a region of negative axial velocity that it created by pushing the flow ahead of itself.

4.7 Summary

The qualitative upstream flame propagation and the approach flow velocity field, which is strongly modified by the propagating flame, have been studied in detail in this chapter. It was found that small-scale bulges, similar to those that facilitate flashback in non-swirling channel flows, exist in boundary layer flashback in the current swirl flow. The formation and break-up process described by Eichler et al. [24] together with their finding of reverse flow pockets as well as the agreement of the measured three-dimensional velocity field with the DNS results by Gruber et al. [25] provide evidence that indeed the flame bulges observed in the present swirl flow result from the same mechanism. However, the findings further show that the formation, upstream propagation, break-up and downstream convection of these bulges on the trailing side of larger flame tongues do not lead to a net upstream flame propagation of the flame.

Instead, flashback is led by larger-scale flame tongues swirling with the bulk flow in the azimuthal direction as they propagate in the negative axial direction along the center body wall. The time-resolved planar three-component and volumetric velocity field measurements revealed that these large-scale flame tongues modify the approach flow differently. A deflection of streamlines ahead and around the flame tip causes a predominantly swirling motion including a region of negative axial velocity for the leading side of the flame tongue to propagate into. This region of negative axial velocity does not correspond to boundary layer separation or a recirculation bubble, and does not feature a stagnation point upstream of the preheat zone, as has been shown in channel-flow flashback [24,25].

The formation of the observed flame tongues affects the flow on a larger scale compared to the small-scale bulges. This observation suggests that the presumed elevated pressure region causing the streamline deflection extends well into the burnt gas. Recent measurement of the wall pressure inside the burnt gas support this finding [51]. However, the region of negative axial velocity, which facilitates the upstream propagation, is still local as it only occupies the portion of the annulus in the vicinity of the flame tongue.

The investigated ultra-lean high-hydrogen content flames differ from the methane flames as they are significantly more convoluted. Despite a matched laminar flame speed, small-scale bulges form and resist the approach flow more frequently. Yet during flashback events these investigated hydrogen flames are found to still form larger

tongues, which propagate upstream in a swirling motion with the smaller bulges being a superimposed perturbation.

Chapter 5: Mechanism Facilitating Swirl Flame Boundary Layer Flashback

This chapter analyzes the flow-flame interaction including the burnt gas velocity field to provide insight into the mechanism facilitating swirl flame boundary layer flashback. Velocity measurements in the burnt gas are enabled by using ceramic particles (rather than olive oil droplets), which do not evaporate as they encounter the flame. Flashback of hydrogen-methane-air flames is studied for a range of conditions in two fields-of-view as described in Section 5.1. The onset of flashback is analyzed in Section 5.2 followed by a detailed discussion of the burnt gas flow field in Section 5.3. Conclusions with regards to the mechanism causing flashback in the investigated swirl flames are drawn in Section 5.4.

5.1 Diagnostic setup and experimental conditions

High-speed stereoscopic PIV and planar flame front detection based on solid seeding particles provided the dataset analyzed in this chapter. The flame luminescence was imaged simultaneously. The experimental techniques are described in Sections 2.2 and 2.3. The velocity field and flame propagation was investigated in a radial-axial plane in the two fields-of-view shown in Figure 2.3.

Flashback of hydrogen-methane-air flames was studied at atmospheric pressure with an inlet air temperature of about 293 K. The sustained upstream flame propagation was investigated for a wide range of hydrogen contents and equivalence ratios. The

parameter space covered is marked by red dots in Figure 5.1. The hydrogen content was varied from 0% to 75% in 25% increments. Increasing the hydrogen content led to a decrease in equivalence ratio when flashback occurred. The grey dashed curve indicates the flashback limit at a bulk flow velocity of 5.0 m/s. Equivalence ratios close to the flashback limit were investigated for each hydrogen percentage as well as equivalence ratios significantly above the flashback limit. The relative size of each red dot shows the relative magnitude of the unstretched laminar flame speeds s_L^0, which were computed with Cantera using the GRIMech 3.0 chemical mechanism. The numerical values are listed in Appendix B. The convex-shaped flame tongues leading flashback are subject to significant stretch effects. The stretched laminar flame speeds are hence expected to be significantly higher for the ultra-lean high-hydrogen content flames owing to thermo-diffusive effects [5]. The colored contours show the adiabatic flame temperatures and unburnt-to-burnt gas density ratio, respectively. The density ratios are listed in Appendix B and range from 4.4 to 7.6.

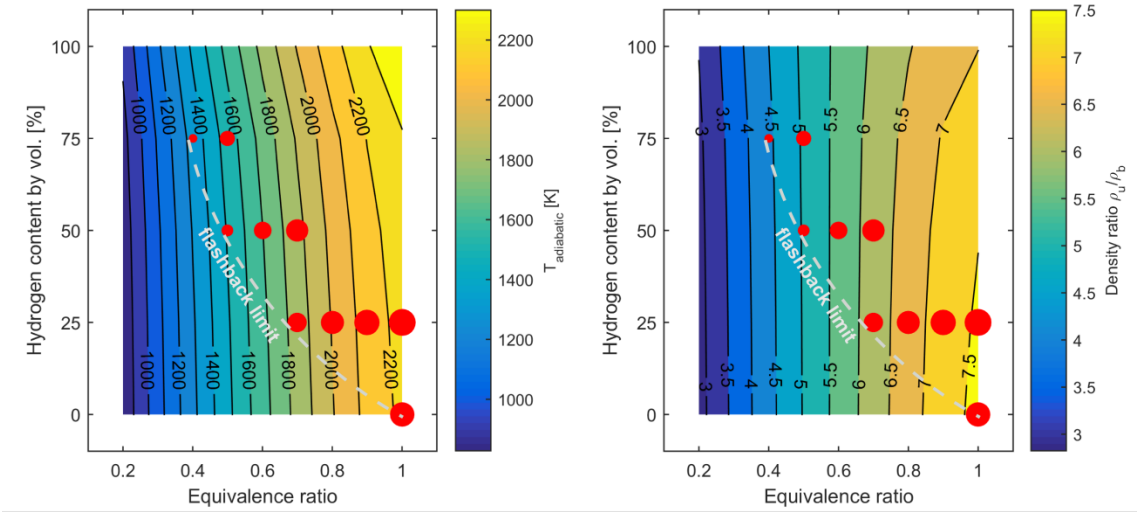

Figure 5.1: Conditions at which flashback was investigated (shown as red dots). The relative dot sizes represent the computed laminar flame speed for the corresponding conditions. The color maps show the adiabatic flame temperature (a) and density ratio between unburnt and burnt gas (b). The grey dashed line indicates the flashback limit for u_{bulk} = 5.0 m/s.

Most of the experiments were conducted using a total flow rate of 500 slpm, which corresponded to a bulk flow velocity of 5.0 m/s and a cold-flow Reynolds number of about Re_h = 8,000 based on the streamwise centerline velocity and the annular gap width h. The maximum flow rate was limited by the diagnostic hardware and the objective to temporally resolve the upstream flame propagation. Flashbacks of a stoichiometric methane-air flame and a hydrogen-methane-air flame with 75% hydrogen and a equivalence ratio of 0.4 were also investigated for a flow rate of 250 slpm corresponding to 2.5 m/s bulk flow velocity and Re_h = 4,000. The detailed flow conditions are listed in Table 5.1. The relevant mean velocity $\langle u_{st} \rangle$ and fluctuation velocity u'_{st} for the investigated swirl flow are in the dominant streamwise direction. The

listed values are evaluated on the centerline of the mixing tube annulus. The turbulent integral time scale τ was computed based on the temporal auto-correlation function. The integral length scale L was computed from the integral time scale and the mean velocity.

Bulk flow	Re_h	$\langle u_{st} \rangle$	u'_{st}	τ	L
5.0 m/s	8,000	9.3 m/s	0.87 m/s	0.20 ms	1.9 mm
2.5 m/s	4,000	4.5 m/s	0.41 m/s	0.51 ms	2.3 mm

Table 5.1: Turbulent flow characteristics. All quantities are based on the velocity in the dominant (streamwise) direction evaluated on the center line.

In total, the findings and conclusions in the following sections are based on detailed measurements of 60 flashbacks (12 conditions with 5 recorded flashbacks for each condition) in the field-of-view "middle" (Figure 2.3) and an additional three flashbacks in the field-of-view "exit". Any observations presented here are common to all flashback events tested at the same condition.

5.2 Onset of flashback

The flow field is first analyzed in the field-of-view at the mixing tube exit (Figure 2.3). The onset of flashback is possibly more geometry dependent and hence less universal than the upstream flame propagation analyzed in the subsequent sections. Nonetheless, understanding the onset in the current configuration subsequently simplifies identifying cause and effect in the mechanism facilitating flashback.

5.2.1 Non-reacting velocity field at mixing tube exit

The non-reacting axial velocity field for a bulk velocity of 5.0 m/s is shown at two instants in time in Figure 5.2. The center body wall is on the left. The center body ends flush with the mixing tube exit at $z = 0$ mm. The mixing tube wall is on the right. Every second vector is plotted. The non-reacting flow field near the mixing tube exit is characterized by an alternate occurrence of high and low axial velocity as shown in Figure 5.2a and Figure 5.2b, respectively. Instants with a reduced axial velocity even feature a region of negative axial velocity along the mixing tube wall reaching rather far upstream as indicated by the solid white line. Note again that the entire flow is non-reacting.

The corresponding time traces of the axial (blue) and azimuthal (red) velocity component are shown in Figure 5.3 for a location in the boundary layer ($r = 0.96$ mm) close to the dump plane ($z = -3.1$ mm). A large-amplitude, periodic fluctuation in the velocity field is observed. At this particular location, the axial velocity fluctuates between about -2 m/s and +7 m/s. The azimuthal velocity fluctuates between about +1 m/s and +7 m/s.

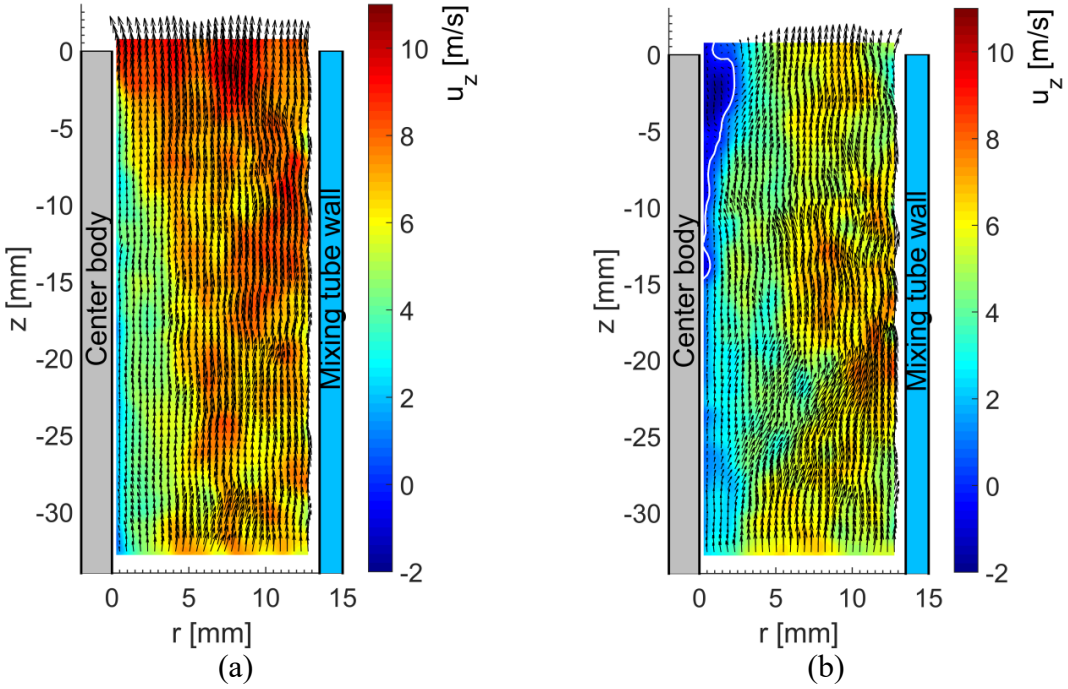

Figure 5.2: Non-reacting velocity field at mixing tube exit at two instants in time. Dump plane is at z = 0 mm. White solid line in (b) corresponds to 0 m/s axial velocity.

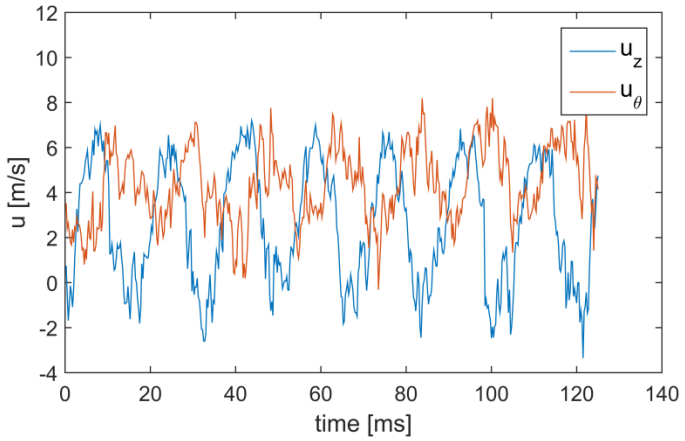

Figure 5.3: Time traces of axial and azimuthal velocity near the center body wall close to the mixing tube exit in the non-reacting case (r = 0.96 mm, z = -3.10 mm).

Computing the power spectral density (PSD) revealed a dominant frequency of 55.7 Hz in all velocity components. The velocity time traces were windowed appropriately (Hanning window) before computing the PSD via a digital Fast Fourier Transform. Proper amplitude scaling of the spectra was ensured applying Parseval's Theorem. As an example, the spectra for the azimuthal velocity are plotted on a semi-log scale at three radial locations and two axial locations in Figure 5.4. The periodic modulation of the velocity field is most dominant near the center body wall close to the sudden expansion. The relative energy in the dominant frequency decreases with increasing radial distance. The modulation is still present at the bottom edge of the field-of-view rather far upstream inside the mixing tube (z = -31.9 mm), though with a decreasing amplitude with increasing distance from the dump plane. The same holds for the axial velocity component. By the "middle" field-of-view, this frequency spike is not observed.

The periodic modulation of the velocity field at the mixing tube exit may be attributed to a hydrodynamic instability inside the combustion chamber termed the precessing vortex core (PVC) [144]. Isothermal swirl flows above a critical swirl number of $S \sim 0.6$ experience vortex break-down when they undergo a sudden expansion such as in the swirl burner used in the present study [27,28]. Despite extensive research, vortex-breakdown is not yet fully understood. Vortex-breakdown is typically associated with a flow-recirculation bubble; however, the generally accepted least common feature among vortex-breakdowns appears to be a stagnation point on or near the axis [30]. A PVC

occurs if a helical hydrodynamic global instability transitions the vortex-breakdown from being axisymmetric to featuring a stagnation-point that is off-axis and precesses with a frequency that scales with the characteristic azimuthal velocity and the nozzle diameter [145]. The frequency associated with the velocity field oscillation was found to change linearly with bulk flow velocity in this work, which is a characteristic feature of the PVC instability [144][146].

Cross-correlating the azimuthal and axial velocity trace shown in Figure 5.3 yields a phase lag of 5.5 ms with the axial velocity component leading the azimuthal component. The phase lag may be explained by the position of the local, precessing stagnation zone (elevated-pressure zone) with respect to the observed fluid region in the field-of-view at a particular instant in time. The pressure gradient associated with the elevated-pressure zone decreases the momentum upstream. At times when the elevated-pressure zone is immediately above the field-of-view, the axial momentum and hence the axial velocity is predominantly decreased. In contrast, the pressure gradient acts predominantly against the azimuthal momentum when the elevated-pressure zone has precessed some angle relative to the field-of-view.

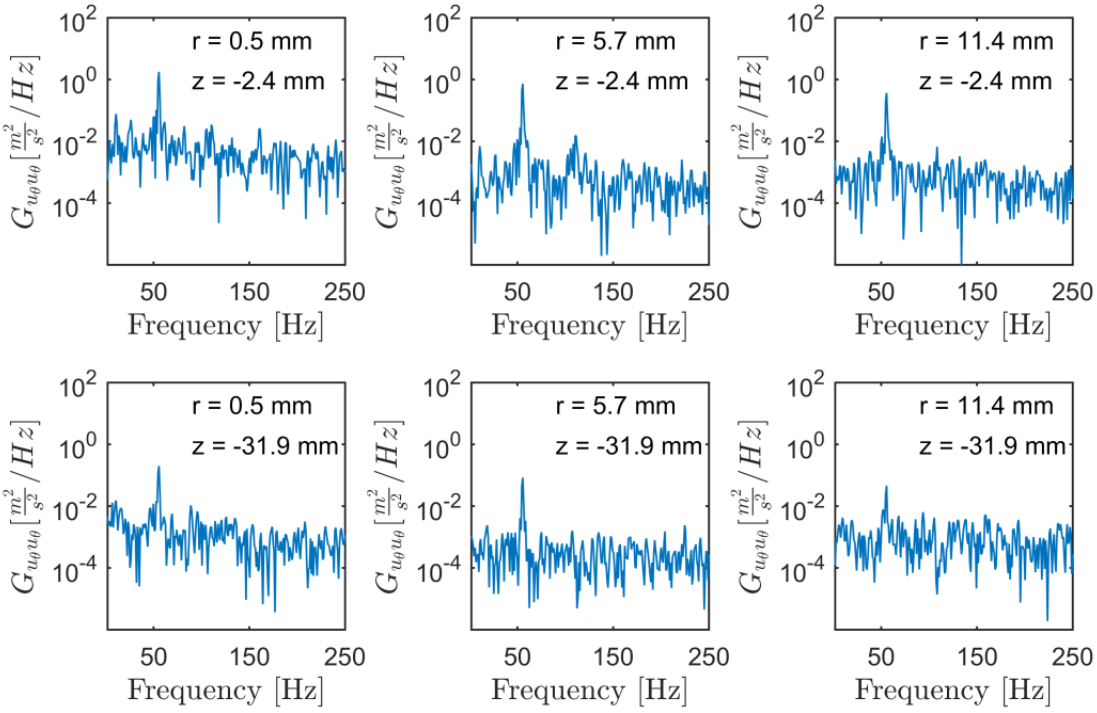

Figure 5.4: Single-sided power spectral density of the azimuthal velocity component in a *non-reacting* case at three radial (columns) and two axial (rows) locations. The dominant peak is at a frequency of 55.7 Hz.

5.2.2 Flame dynamics close to flashback

Stable flames in the investigated swirl combustor were stabilized about 5-10 mm downstream of the center body tip. When approaching the flashback limit, the flame shifted upstream and stabilized on the center body rim. In this intermediate state between a stable flame and flashback, which was also observed in a similar swirl burner [47], the flame was found to already penetrate into the mixing tube along the center body wall without initiating a sustained flashback. In some cases, flame tongues were found to form, propagate upstream a short distance (~ 5 mm) and swirl around the center body

before being washed downstream again. As an example, a chemiluminescence image sequence is shown in Figure 5.5 for a methane-air flame at a bulk flow velocity of 2.5 m/s.

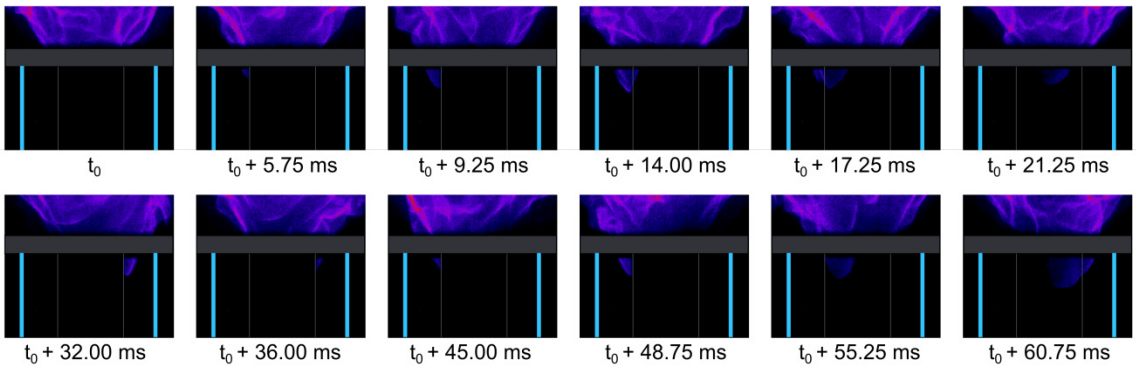

Figure 5.5: Luminosity time-sequence of a condition close to flashback, but without flashback. Flame tongues begin to penetrate upstream into the mixing tube without initiating a sustained flashback. Horizontal grey bar indicates plate separating mixing tube from combustion chamber. Vertical lines outline center body (grey) and mixing tube wall (blue).

The velocity field for such an intermediate state with a methane-air flame ($\phi = 0.85$) stabilized on the center body rim is analyzed next for the 5.0 m/s bulk velocity case. The non-reacting flow field for the same bulk flow velocity was discussed previously in Section 5.2.1. The spectra are computed for the reacting case at the same spatial locations and shown in Figure 5.6. The oscillation in the velocity field, which was attributed to a PVC, is completely eliminated. The absence of any dominating frequency suggests that the PVC has been suppressed entirely by the flame, which is in agreement with previous works showing that a PVC existing in the isothermal case may be

suppressed in the reacting case [144,145,147]. As a result, periodically occurring regions of negative axial and reduced azimuthal velocity due to a PVC do not exist anymore.

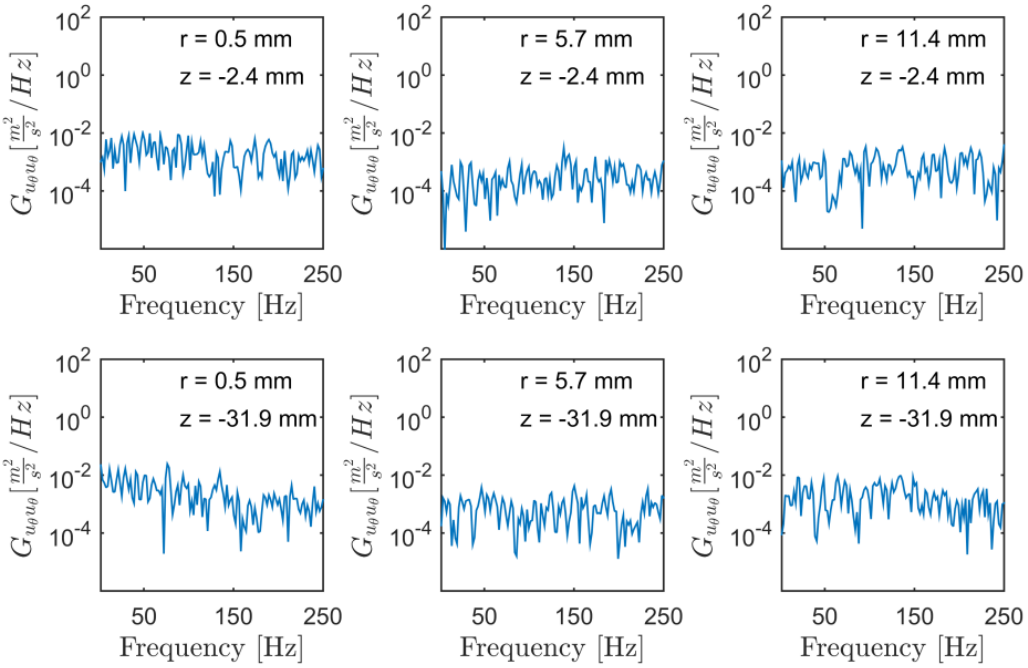

Figure 5.6: Single-sided power spectral density of the azimuthal velocity in the *reacting* case at the onset of flashback in analogy to the non-reacting flow spectra in Figure 5.4.

The axial and azimuthal velocity fields are shown in Figure 5.7 at one instant in time. The solid black line marks the flame front. The flame is found to intermittently creep upstream into the mixing tube along the center body wall at equivalence ratios below the flashback limit. Despite the absence of a PVC, the flow near the center body wall upstream of the dump plane is characterized by a predominantly swirling motion with a mean axial velocity of about 0 m/s and a positive azimuthal velocity as shown in Figure 5.8 before the onset of flashback (t < 200 ms). Turbulent fluctuations around the

mean then lead to intermittently occurring regions of negative axial velocity, which is shown in Figure 5.7a (solid white line).

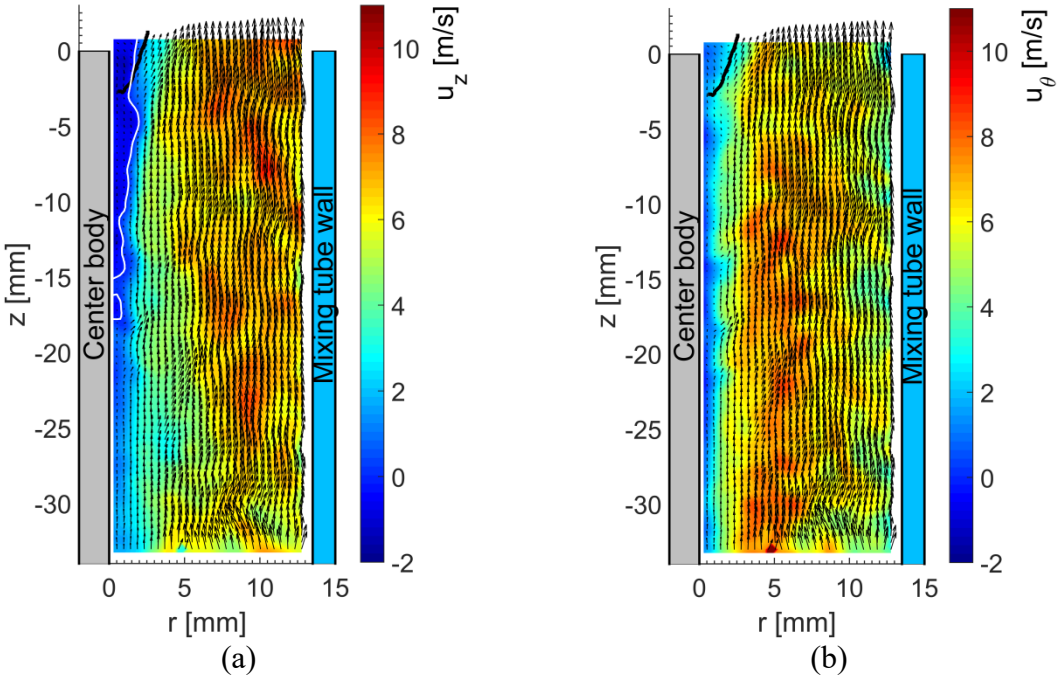

Figure 5.7: Velocity fields at the onset of flashback: (a) Axial and (b) azimuthal velocity field at the mixing tube exit at conditions close to flashback. Black line: flame front. White line: 0 m/s isoline.

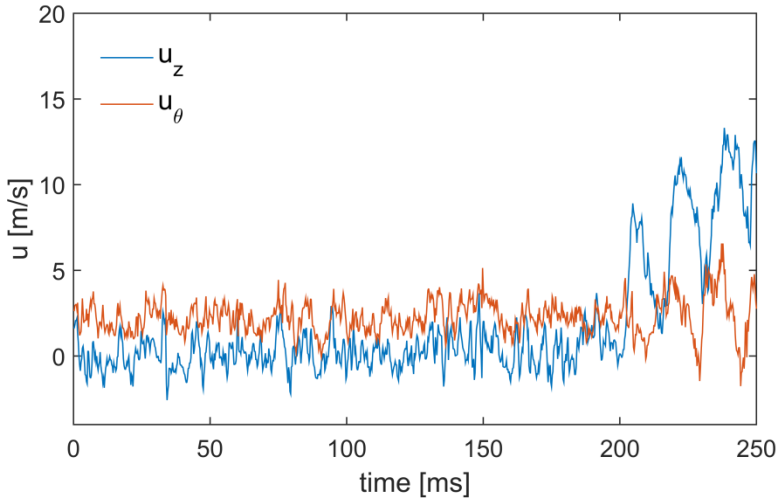

Figure 5.8: Axial and azimuthal velocity time traces at the onset of flashback and near the mixing tube dump plane (r = 0.96 mm, z = -3.10 mm).

In summary, the flame is observed to intermittently penetrate into the mixing tube prior to flashback. Experimental evidence is found that regions of negative axial velocity corresponding to a predominantly swirling flow exist along the center body wall close to the mixing tube exit even before flashback occurs. These regions appear to either be an upstream effect of a PVC or caused by the flame being stabilized at the center body rim. The latter holds when the PVC is suppressed in the reacting flow as is the case for the swirl burner and conditions investigated in this work. A similar observation of, in this case, reverse flow prior to flashback was made based on a 2D RANS simulation investigating the onset of boundary layer flashback in a non-swirling flow [24]. It was argued that flashback occurs once the convex shaped flame bulges induce a reverse flow reaching above some quenching distance. To test whether the hypothesis holds for swirl flame boundary layer flashback in the current configuration, the radial spread of the

negative axial velocity region prior to flashback is evaluated. The histogram shown in Figure 5.9 aggregates the maximum radial spread for each of the 1800 time steps recorded before flashback occurred. The mean and median thickness of the layer characterized by a negative axial velocity is 1.4 mm. In comparison, the quenching distance for this lean methane-air mixture ($\phi = 0.85$) is below 1 mm [148–150]. It may therefore be concluded that for the investigated swirl flames the region of negative axial velocity, at least intermittently, already reaches beyond the quenching distance prior to flashback. The onset of flashback is seen in the velocity traces in Figure 5.8 at $t = 200$ ms, which leads to a sustained upstream flame propagation investigated in the following section.

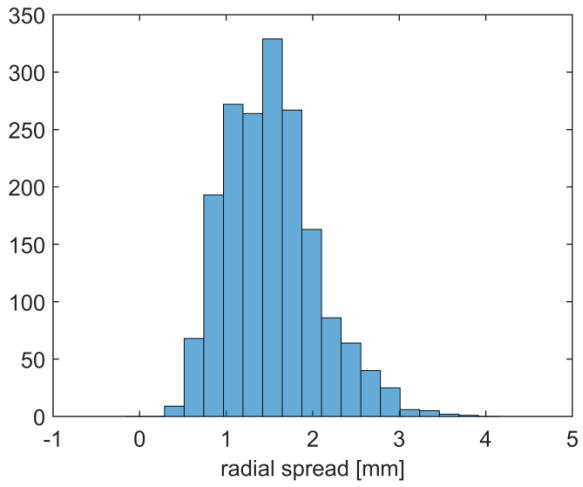

Figure 5.9: Histogram aggregating the maximum radial spread of the negative axial velocity region for 1800 time steps recorded prior to flashback of a methane-air flame.

5.3 Burnt gas velocity field associated with flashback

We now turn from the onset of flashback to analyzing the velocity field associated with the sustained upstream flame propagation in the field-of-view "middle" (Figure 2.3). In contrast to Chapter 4, the focus is now on the burnt gas velocity field as it provides valuable insight in the mechanism driving flashback. A methane-air flashback ($\phi = 1.0$) for the higher bulk flow velocity of 5.0 m/s is investigated first.

The velocity field is shown in Figure 5.10 for an instant in time when the leading side of the flame tongue is in the field-of-view, which is known based on the simultaneously recorded chemiluminescence (Figure 5.10a). As shown in Sections 4.5 and 4.6 based on 2.5 m/s bulk flow velocity cases, the flow field upstream of the leading flame tongue is characterized by a predominantly swirling motion (small u_z, small u_r and large u_θ) with a small negative axial velocity component. The negative axial velocity region is still observed at twice the bulk flow velocity as seen in Figure 5.10b, again indicated by the white solid line corresponding to an isoline of 0 m/s. Furthermore, the burnt gas velocity field measurements reveal that the regions of negative axial velocity reach well within the burnt gas. On average, 35% of the area characterized by a negative axial velocity component is within the burnt gas (based on all time steps of all 5 methane-air flashback events recorded under identical conditions). The axial velocity then gradually increases with downstream distance from the leading flame tip.

The azimuthal velocity is reduced in the burnt gas as seen in Figure 5.10c, which has important implications for the mechanism driving flashback. The azimuthal velocity field is discussed in detail below (Section 5.3.3).

The radial velocity is generally found to correlate well with the flame front location in a sense that the radial velocity tends to be positive on the unburnt side and is shifted to negative velocities on the burnt side of the flame front (Figure 5.10d). The radial velocity field is discussed in more detail below (Section 5.3.2).

The velocity magnitude decreases significantly in the vicinity of the leading flame tip as seen in Figure 5.10e, which indicates a loss in momentum. The velocity magnitude is particularly low on the burnt gas side of the leading flame tip despite the heat release, which is in contrast to an ideal planar flame front, where the static pressure drops across the flame and the heat release leads to an increase in momentum of the burnt gas. The conditions leading to this low-momentum region in the burnt gas will be discussed further in Section 5.3.2

The azimuthal vorticity field is shown in Figure 5.10f. A number of vortical structures with sizes on the order of the integral scale and smaller are seen in the unburnt gas. Such structures of comparable magnitude are not found in the burnt gas, which is expected due to significantly higher viscosity. The region near the center body wall upstream and along the leading flame tip is again dominated by negative azimuthal vorticity, which has been discussed previously in Section 4.5.2. Strong azimuthal

(boundary layer) vorticity is found in the burnt gas, which is attributed to the acceleration of the burnt gas in the axial direction seen in Figure 5.10b.

Gas expansion leads to non-zero dilatation at a premixed flame front. With planar PIV, only the in-plane gradients are available. Nonetheless, a significant level of non-zero in-plane dilatation is generally found to correlate well with the flame front location as shown in Figure 5.10g.

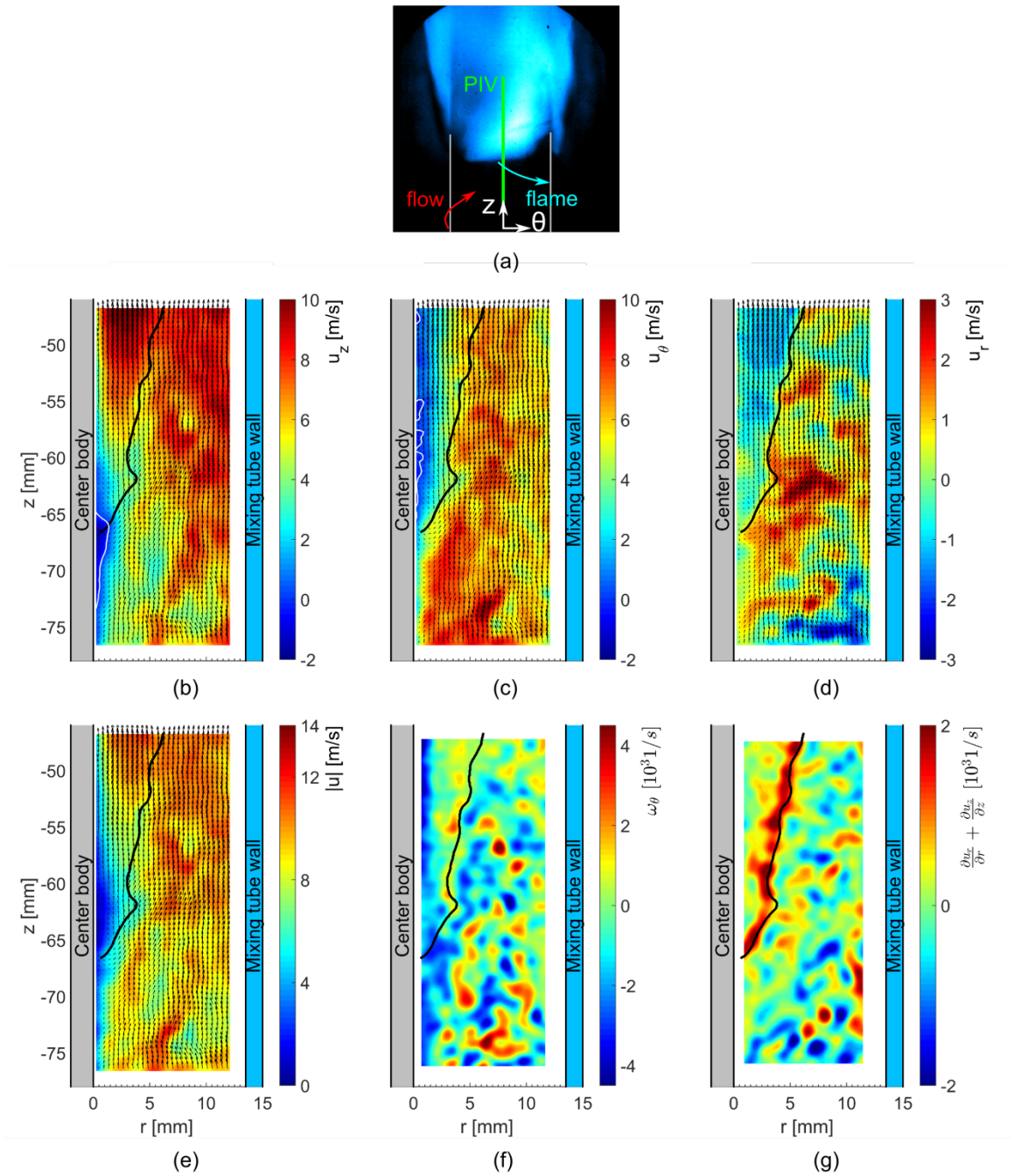

Figure 5.10: CH_4-air flashback at $\phi = 1.0$. (a) Luminescence image providing the flame tongue location in relation to the laser sheet, (b) axial velocity, (c) azimuthal velocity, (d) radial velocity, (e) velocity magnitude, (f) azimuthal vorticity and (g) in-plane dilatation. Black line: flame front. White line: 0 m/s isoline.

5.3.2 Radial velocity field and flame spread

The radial velocity field, which was found to be positive on the unburnt side of the flame and negative on the burnt side in regions where the flame front is aligned perpendicular to the radial direction as shown in Figure 5.10d, is investigated further. The corresponding PDFs evaluating the radial velocity component for all time steps along the flame front are shown in Figure 5.11. The PDFs are conditioned on the unburnt and burnt gas side, respectively. Only vectors within 1 mm of the flame front location to either side are included in the PDFs. Also included is the PDF of radial velocities in the non-reacting case, which were sampled from the same locations as for the reacting case. The PDFs confirm that the shift towards negative radial velocities on the burnt side and to positive radial velocities on the unburnt side seen at one instant in time in Figure 5.10d generally holds. This observation on the radial velocity field may be compared to two limiting cases (with regards to the burnt gas velocity) of premixed flame propagation. The flame front is treated as a discontinuity in the following discussion where the role of turbulence is limited to slightly wrinkling the flame and moderately increasing the flame speed (flamelet regime).

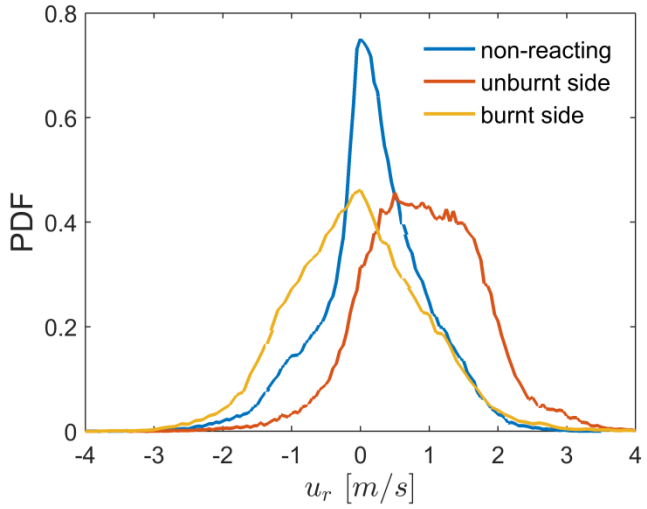

Figure 5.11: PDFs of radial velocity magnitudes evaluated along the flame front. The PDFs are conditioned on the region within 1 mm of the flame front location to the unburnt and burnt gas side. For comparison, the PDF of radial velocities in the non-reacting case is evaluated at the same location as for the reacting case.

The first limiting case is an ideal planar flame propagating into quiescent reactants (e.g., in a channel) as shown in Figure 5.12. The flame front propagates to the left into the unburnt gas. Gas dilatation leads to a local pressure build-up acting in all directions, which corresponds to a blockage effect (Rayleigh flow). In the case of this planar flame, there is no constraint on the burnt gas moving to the right. The products can expand freely and accelerate normal to the flame front in the direction opposite to the flame propagation direction. Since the burnt gas is much lighter than the unburnt gas (density ratio of about 7.5 for stoichiometric CH_4-air flame), dilatation primarily accelerates the burnt gas whereas the effect on the heavy unburnt gas is negligible. To a good approximation, the flame is passively propagating into the reactants without

inducing motion in the unburnt gas. The magnitude of the lab-frame propagation velocity (green arrow) equals the flame speed with respect to the unburnt gas, $|\boldsymbol{v}_f| = s^u$.

The opposite limiting case is the propagation of a spherically expanding flame into an initially quiescent unburnt gas, which is frequently utilized to measure laminar flame speeds [88,151]. In contrast to the planar flame, the *burnt gas* remains quiescent in the lab-frame, which is effectively a result of a constraint imposed by geometry: Any net burnt gas velocity induced by a flame front element is counteracted by the flame front on the opposite side of the spherical flame surface. Dilatation hence has no other chance than accelerating the unburnt gas ahead of the flame front and so the flame front propagates with a lab-frame velocity that matches the flame speed based on the burnt gas, $|\boldsymbol{v}_f| = s^b = \rho_u \rho_b^{-1} \cdot s^u$. The constraint on the burnt gas velocity together with the jump condition in density (mass conservation) across the flame front causes the flame to induce a radial velocity ahead of itself in the originally quiescent unburnt gas.

In summary, two flames having the same flame speed *s* propagate at significantly different lab-frame propagation velocities due to the different constraints on the burnt gas. The spherically expanding flame propagates faster by a factor equal to the density ratio ρ_u/ρ_b, which is about 7.5 for the investigated, stoichiometric methane-air flame.

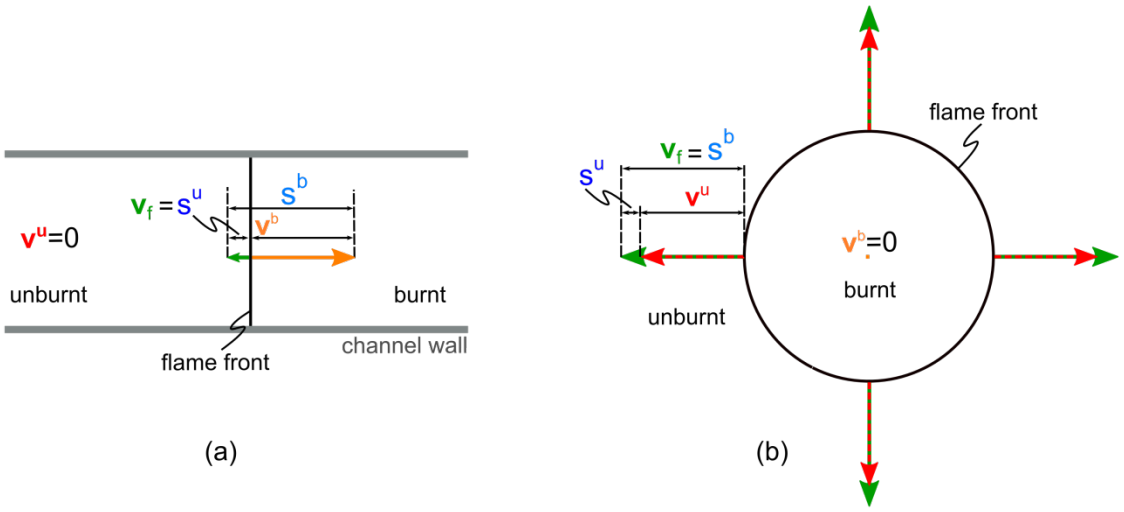

Figure 5.12: Comparison of two limiting cases of premixed flame propagation with respect to the burnt gas velocity field. (a) Ideal planar flame propagating in a channel. (b) Spherically expanding flame. Symbols: Lab-frame flame propagation velocity $\boldsymbol{v}_f$ (green); flame speed with respect to the unburnt (s^u, dark blue) and burnt gas (s^b, light blue); flow velocity with respect to the unburnt ($\boldsymbol{v}^u$, red) and burnt gas ($\boldsymbol{v}^b$, orange).

The PDFs in Figure 5.11 suggest the radial flame spread of the investigated CH_4-air flames lie between the two limiting cases. The portion of the flame surface characterized by a surface normal vector pointing in the radial direction (vertical flame front) does not passively propagate outwards but pushes the flow ahead of itself by inducing a positive radial velocity component. At the same time, regions exist where the burnt gas has a net negative radial velocity in the lab-frame-of-reference. The constraint on the radial burnt gas velocity in the investigated swirl flames is the center body wall, since the near-wall flow has to be tangent to the wall (0 m/s radial velocity). The gas dilatation combined with the constraint of the center body wall on the burnt gas hence acts as a blockage on the approach flow causing the unburnt gas to accelerate axially in

the annular gap between flame front and mixing tube wall similar to the findings of boundary layer flashback in a (non-swirling) channel flow [26]. The acceleration of the unburnt gas was discussed in Section 4.5.3. In contrast to channel flashback, the flow also accelerates in the axial direction on the opposite side of the center body, which is possible owing to the shape of the flame tongues (they only occupy a portion of the annulus in the azimuthal direction).

Nominally, a positive radial pressure gradient forms, which is responsible for the centripetal acceleration in the investigated swirl flow. Pushing the unburnt gas ahead of the flame front in the positive radial direction and turning the burnt gas tangent to the wall may both be achieved by a reduced radial pressure gradient. A modified radial pressure distribution may potentially contribute to the formation of an adverse axial pressure gradient as discussed in Section 5.3.4.

5.3.3 Azimuthal velocity field and blockage effect

The deceleration of the burnt gas velocity in the azimuthal direction is discussed in more detail in this section since the findings have important implications for the mechanism driving flashback. A methane-air flashback at 5.0 m/s bulk flow velocity is again taken as an example. It is particularly instructive to visualize the velocity in an azimuthal-axial plane as opposed to the radial-axial plane (corresponding to the laser sheet) in which the planar data has been presented before. Since imaging in an azimuthal-

axial plane would require a curved laser sheet wrapped around the center body, a pseudo azimuthal-axial surface is visualized by taking advantage of the time-resolved data.

The velocity field is sampled along a vertical line – i.e., at a fixed radial location and for all axial locations – over time to construct the vector plots shown in Figure 5.14. The horizontal axis is the time axis. Note that time increases from right to left. The vertical axis corresponds to the axial direction. Figure 5.14(a), (b), (c) and (d) present vector fields at progressively larger radial locations (i.e. $r = 0.47$ mm, 0.91 mm, 1.35 mm and 2.01 mm, respectively). These vector fields are analogues to different diameter annular shells on which the velocity measurements are made. Figure 5.13 further illustrates how Figure 5.14 is constructed. The luminescence images in Figure 5.13a show the global flame propagation and position of the leading flame tongue at four instants in time. The time in milliseconds corresponds to the time scale of the time axis in Figure 5.14. Each vector column in Figure 5.14 corresponds to a vector column sampled at a fixed radial position at one instant in time. The radial positions where the vector columns are sampled are illustrated in the radial-axial contour plots in Figure 5.13b and c. The inverse time axis in Figure 5.14 may be interpreted as the azimuthal direction in a Taylor's hypothesis sense; however, Taylor's hypothesis does not hold in this case due to the transient nature of the flow and the presence of the propagating flame. Gradients may hence not be computed along the time axis. Nonetheless, constructing the velocity field in this way is particular instructive since the plotted vectors are composed of the azimuthal and axial component. Changes in swirl are hence readily visualized.

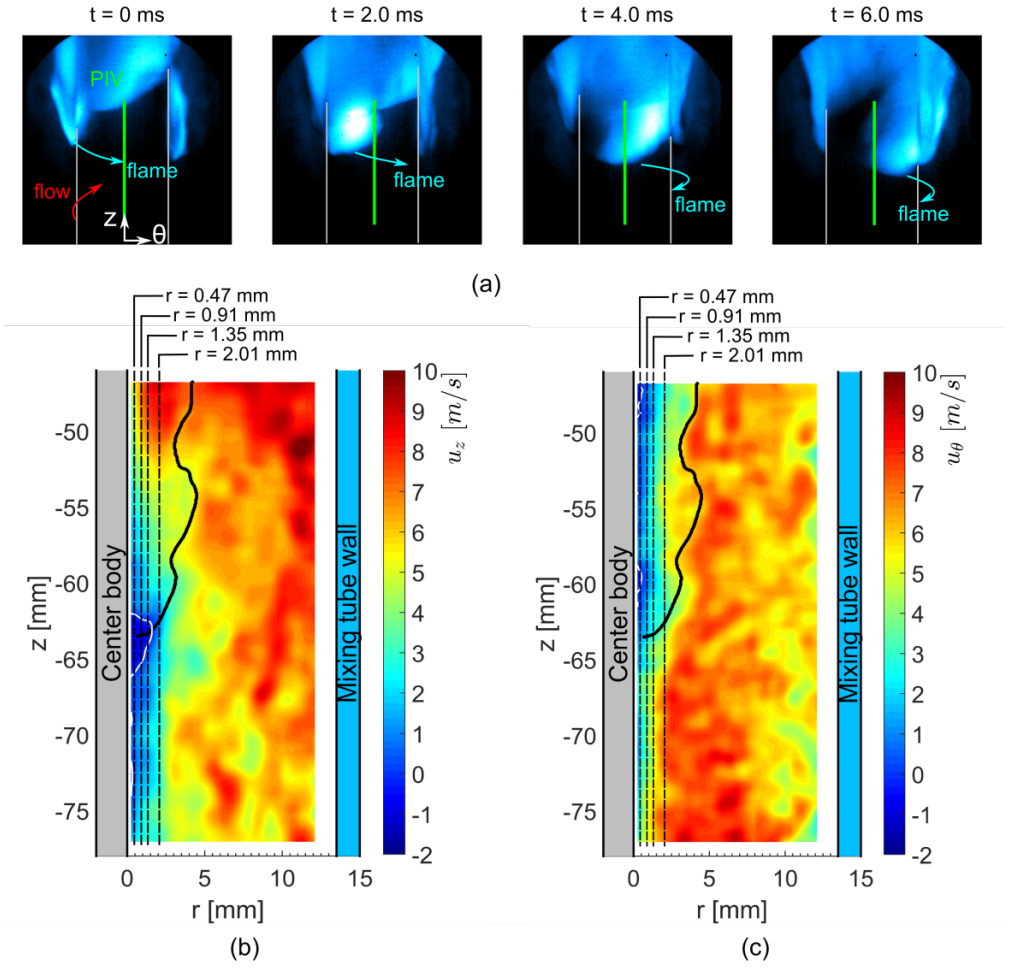

Figure 5.13: Graphic illustrating the axial distance versus time vector space shown in Figure 5.14. (a) Global flame position relative to laser sheet at four instants in time. The vector field in Figure 5.14 is constructed by sampling the velocity vectors over time at four fixed radial positions. The radial positions are marked by dashed lines in the axial (b) and azimuthal (b) velocity field.

The grey background in Figure 5.14 marks the burnt gas region. The obtained shape of the burnt gas region approximates the shape of the flame tongue swirling through the field-of-view. The global flame propagation direction of the leading side of the flame tongue is indicated by the blue arrow. Before discussing the burnt gas velocity

field, note how the velocity field on the unburnt side in Figure 5.14b agrees with the schematic in Figure 4.11, which summarizes the findings based on the measurements presented in Section 4.5.

A large portion of the burnt gas velocity field is found to be characterized by a predominantly axial flow direction at a radial distance from the wall that is on the order of the quenching distance (r = 0.91 mm, Figure 5.14b). The azimuthal velocity component is essentially decelerated to zero in the center of the burnt gas region enclosed by the convex-shaped flame tongue. Close to the wall (r = 0.47 mm), where the azimuthal velocity in the non-reacting case is lower, the flow is even turned in the negative azimuthal direction in some regions as shown in Figure 5.14a. These regions are marked by the white isoline of 0 m/s in Figure 5.13c. At larger radial distances the azimuthal velocity is still decelerated as shown at r = 1.35 mm (Figure 5.14c) and r = 2.01 mm (Figure 5.14c). However, the final decelerated azimuthal velocity component increases with radial distance, which may be expected because the azimuthal momentum flux of the approach flow increases with radial distance across the boundary layer.

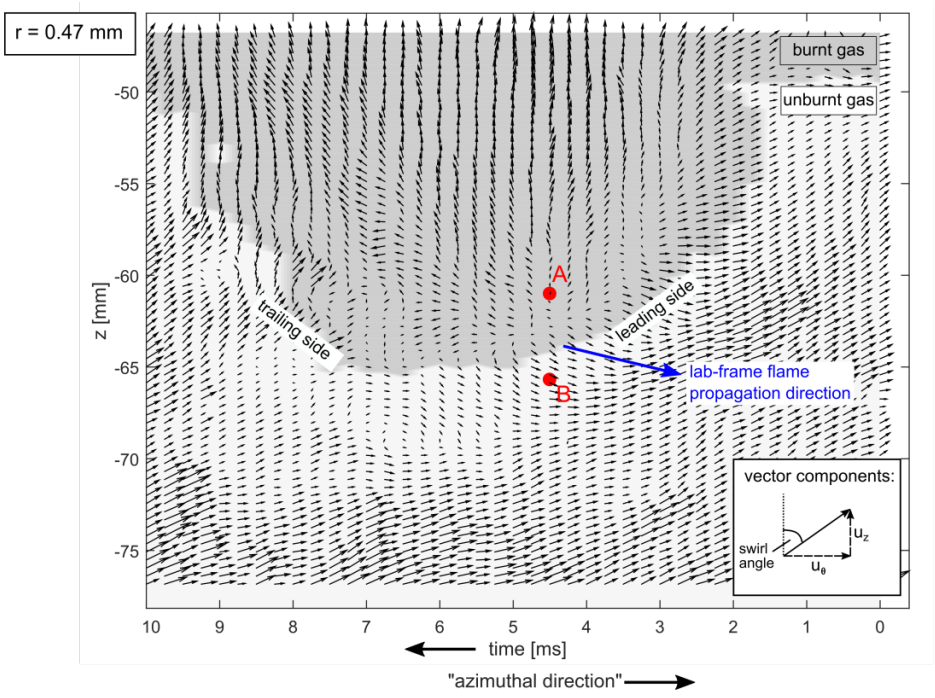

(a)

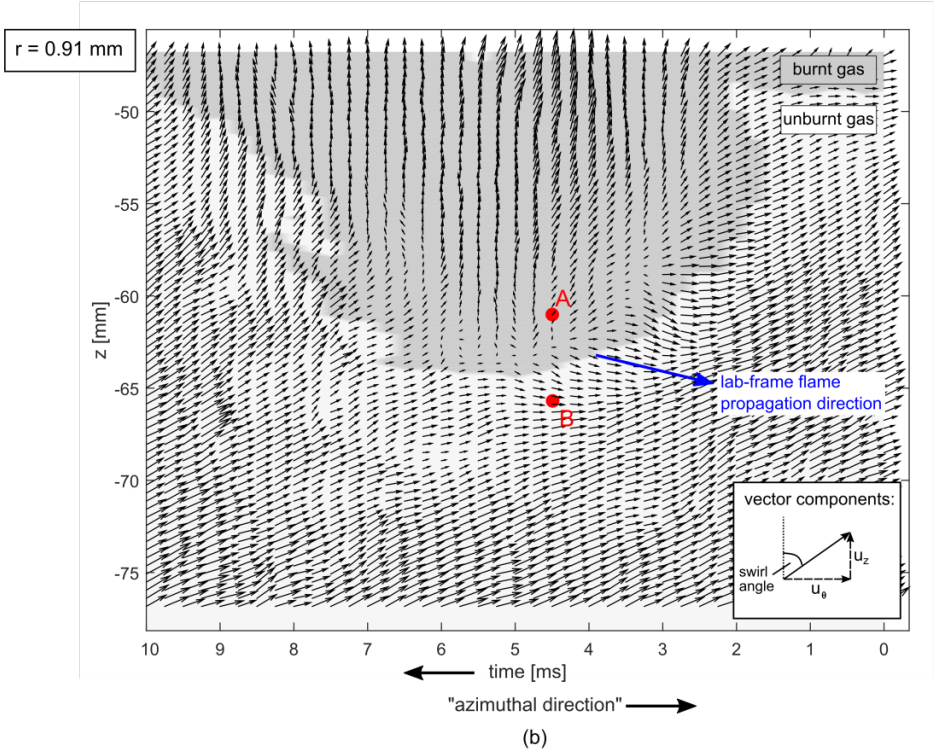

(b)

Figure 5.14

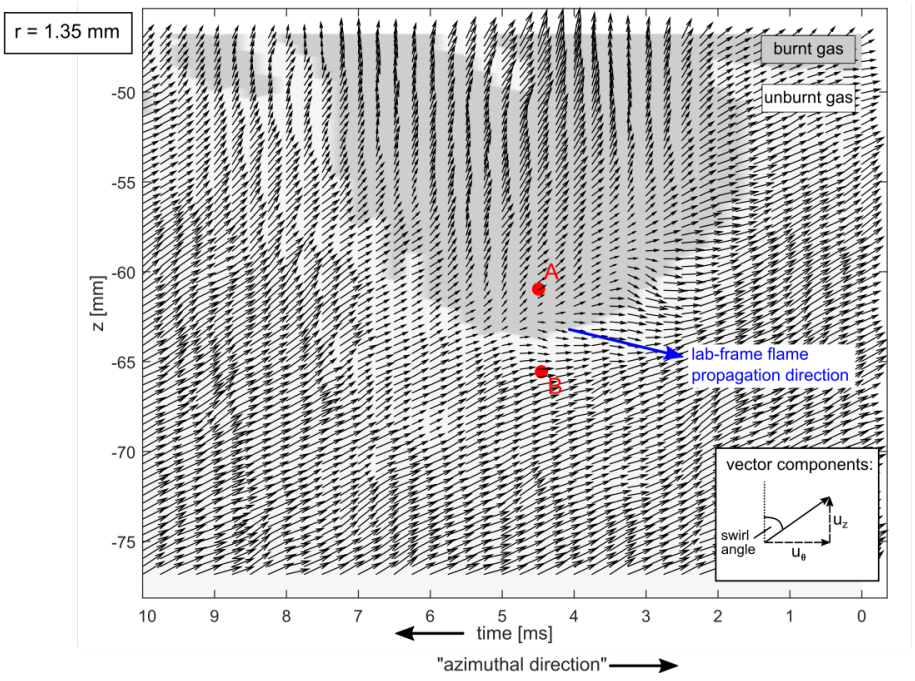

(c)

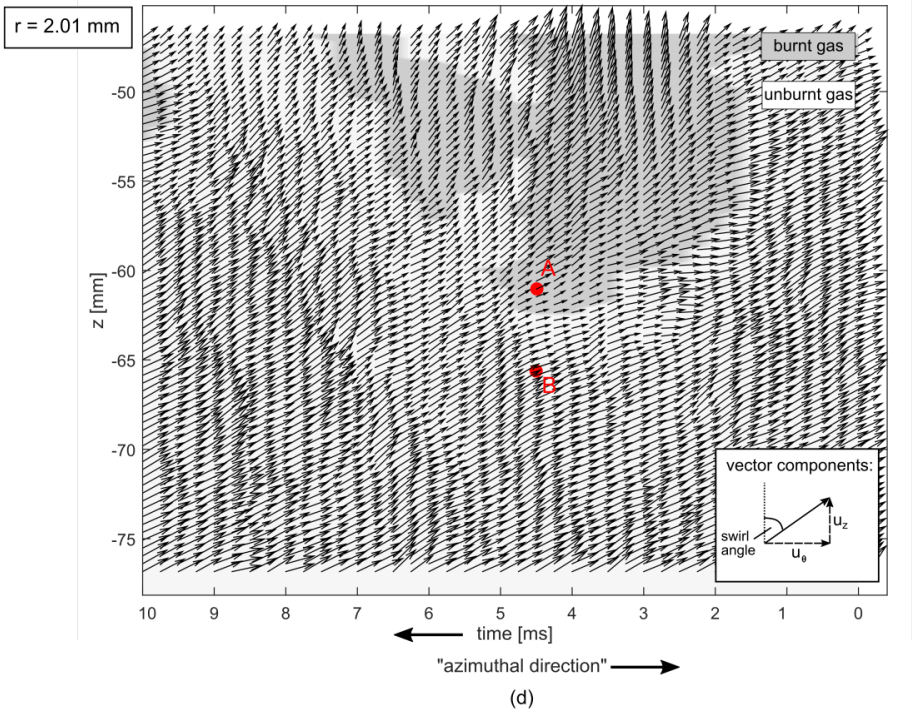

(d)

Figure 5.14: Velocity field in time-z-space at radial locations (a) $r = 0.47$ mm, (b) $r = 0.91$ mm, (c) $r = 1.35$ mm, (d) $r = 2.01$ mm. CH_4-air flashback, $\phi = 1.0$.

Let us now investigate the cause for the deceleration of the azimuthal velocity and the turning of the burnt gas flow toward the axial direction. For that purpose, it is instructive to compare the characteristic shape of a flame tongue and the associated flow field to the two limiting cases of the ideal planar and spherically expanding flame introduced in Section 5.3.2. It was shown that for the spherically expanding flame the dilatation accelerates the unburnt gas ahead of the flame front due to the geometrical constraint (the burnt gas velocity had to be stagnant). A similar effect appears to be responsible for the deceleration of the unburnt gas ahead of the flame tongues and hence contribute to the occurrence of flashback.

First, consider flame front elements on the leading side and trailing side of a flame tongue, as shown in Figure 5.15. Let us assume for now that these leading and trailing side flame fronts develop independently; i.e., there is no constraint on the burnt gas velocity field and hence the flame front elements propagate like ideal planar flames.

The velocity vector in the unburnt gas (red arrow) is based on the measured mean non-reacting velocity field at $r \approx 1.0$ mm ($v_z^u = 2.2$ m/s, $v_\theta^u = 4.0$ m/s). All subsequent velocity vectors in Figure 5.15 are drawn to scale relative to the unburnt velocity field. The flame front elements propagate normal to themselves with a local turbulent displacement speed s_T^u relative to the local unburnt velocity v^u. The estimated flame displacement speed for the stoichiometric CH_4-air flame is 0.7 m/s as discussed in Appendix C. The local flow velocity, the flame speed and the lab-frame flame propagation velocity are related according to

$$s_T^u = \left(\boldsymbol{v}^u - \boldsymbol{v}_f\right) \cdot \boldsymbol{n}, \tag{5.1}$$

where $\boldsymbol{n}$ is the flame-normal vector, which is defined positive pointing from the unburnt to the burnt gases [152]. The flame speed is the difference between the flame-normal component of the velocity vector and the lab-frame flame propagation vector. Solving Eq. (5.1) for $\boldsymbol{v}_f$, the lab-frame propagation velocity is computed (green vector), which points in the positive azimuthal and positive axial direction. Clearly, in the absence of any dilatation induced blockage effect on the approach flow, the flame front element on the trailing and leading side both propagate downstream (i.e., no flashback) because the nominal approach flow velocity significantly exceeds the flame speed about one quenching distance away from the wall.

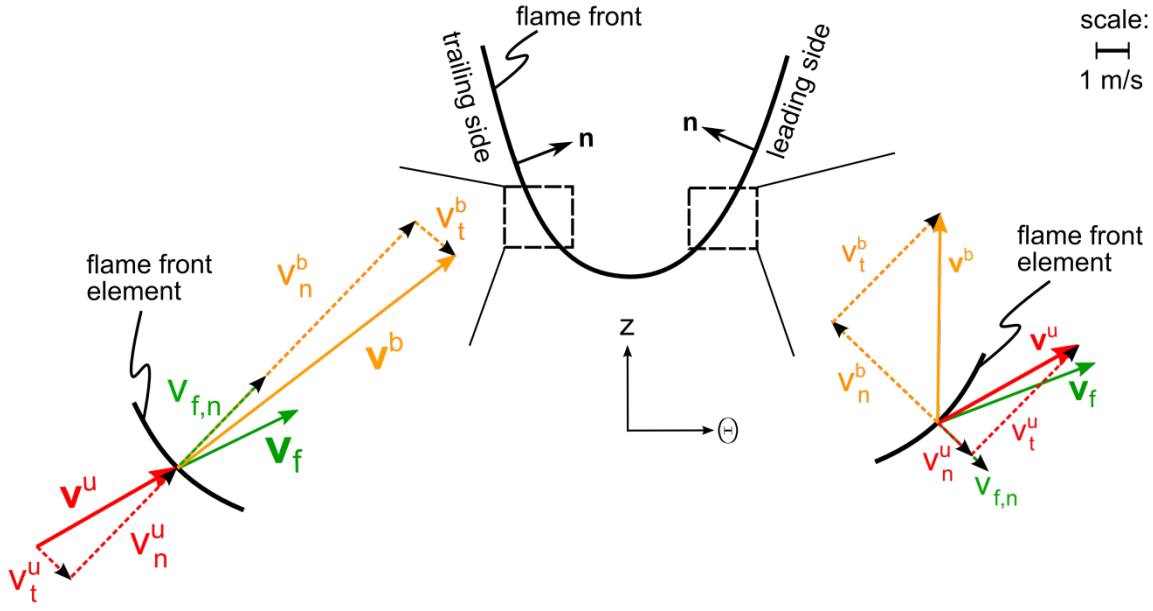

Figure 5.15: Schematic diagram showing the hypothetical unburnt and burnt gas velocity field without any dilatation induced blockage on the approach flow. Red: Velocity field in unburnt gas at $r \approx 1.0$ mm. Orange: Burnt gas velocity field. Green: Lab-frame flame propagation velocity. Assumed density ratio: 7.5.

The jump conditions in the limit of a thin flame are now applied to construct the hypothetical burnt gas velocity field. Mass conservation in a control volume encompassing the flame front then dictates that

$$s_T^b = s_T^u \cdot \frac{\rho^u}{\rho^b} \tag{5.2}$$

and provides the flame speed with respect to the burnt gases, s_T^b. The burnt gas is accelerated in the direction normal to the flame front by a factor of 7.5, which is the density ratio for the investigated stoichiometric CH_4-air flame. In analogy to the unburnt gases, the flow velocity, flame speed and lab-frame flame propagation velocity are related by the following relation,

$$s_T^b = \left(\boldsymbol{v}^b - \boldsymbol{v}_f\right) \cdot \boldsymbol{n}, \tag{5.3}$$

which provides the burnt gas velocity component normal to the flame front. Assuming no forces act in the tangential direction, tangential momentum is conserved and the flow velocity tangential to the flame front is constant across the flame front. The burnt gas velocity vectors are shown as orange arrows in Figure 5.15. On the trailing side, the approach flow velocity is approximately aligned with the flame-normal vector; hence, the unburnt gas would be accelerated in the positive axial direction to about 12 m/s, and in the positive azimuthal direction to about 15 m/s. In contrast, on the leading side, the flame-normal vector is aligned such that the flow is accelerated in the negative azimuthal direction, which leads to an azimuthal velocity in the burnt gas of about 0 m/s. The axial burnt gas velocity would again be about 12 m/s.

The mismatch in the azimuthal burnt gas velocity component clearly shows that a constraint on the burnt gas velocity field exists similar to the spherically expanding flame. The gas processed by the leading side appears to impose a blockage in the azimuthal direction on the gas processed by the trailing side. In contrast to the spherically expanding flame, the burnt gas can accelerate in the positive axial direction in this two-dimensional treatment of a flame tongue.

To satisfy the constraint on the burnt gas velocity field, gas dilatation significantly affects the burnt *and* unburnt gas as the measured velocity fields show (e.g. Figure 5.14). The modified flow fields at characteristic locations on the trailing and leading side, respectively, are summarized in the schematic diagram in Figure 5.16. The flow velocities are shown at a radial location of $r \approx 1.0$ mm to match the previous theoretical treatment in Figure 5.15. An actual measured velocity field associated with a flame tongue at $r \approx 1.0$ mm was shown in Figure 5.14b. The dilatation-induced blockage decelerates the azimuthal velocity component upstream of the trailing side to about 3 m/s. The flame front along the trailing side propagates downstream in the lab-frame of reference as indicated by the green arrow. The lab-frame speed of features on the trailing side of the flame front seen in the high-speed chemiluminescence movies agrees well with the vector $\boldsymbol{v}_{f,1}$. Ahead of the leading side, the azimuthal velocity is increased to about 4.5 m/s. At the same time, the flow is strongly decelerated in the axial direction along the leading side. The axial velocity reaches negative axial values of about -0.5 m/s. The modified unburnt velocity vectors $\boldsymbol{v}^u$ are shown in red in Figure 5.16. The lab-frame

flame propagation velocity $\boldsymbol{v}_f$ along the leading side is approximately known from global flame propagation speed measurements based on the high-speed chemiluminescence movies. A CH_4-air flame tongue propagates with about 5.2 m/s in the positive azimuthal direction and with about 1.1 m/s in the negative axial direction, which is indicated by the green arrow. The difference between the local flow velocity and the lab-frame propagation velocity is the flame speed according to Eq. (5.1). The difference agrees well with the turbulent displacement speed of about 0.7 m/s estimated in Appendix C and used for the theoretical discussion in combination with Figure 5.15.

The burnt gas velocity vector $\boldsymbol{v}_2^b$ (orange vector) shown in Figure 5.15 is obtained by applying the jump conditions. It is included in Figure 5.15 because it agrees well with the actual burnt gas velocity field in the center of the burnt gas region enclosed by the convex flame tongue as seen in Figure 5.14b: The burnt gas is decelerated in the azimuthal direction to about 0 m/s as discussed before and has a low axial velocity, which only increases gradually with downstream distance from the leading flame tip. The fact that the jump conditions applied to the local modified flow field at the leading side agrees well with the measured burnt gas velocity supports the notion that the gas processed by the leading side determines the burnt gas velocity field by imposing a blockage on the gas processed by the trailing side. In the absence of the leading side burnt gas, the trailing side burnt gas would be accelerated in the positive azimuthal direction.

The change in azimuthal momentum of the burnt gases described above must be caused by an azimuthal pressure gradient. Such a pressure gradient is supported by

pressure measurements on the center body wall in a similar configuration [51]. Viscous effects may add to the reduction of the azimuthal velocity in the near-wall (low-momentum) region both along the leading and trailing side of the flame tongue since the sharp increase in temperature across the flame front leads to an increase in viscosity.

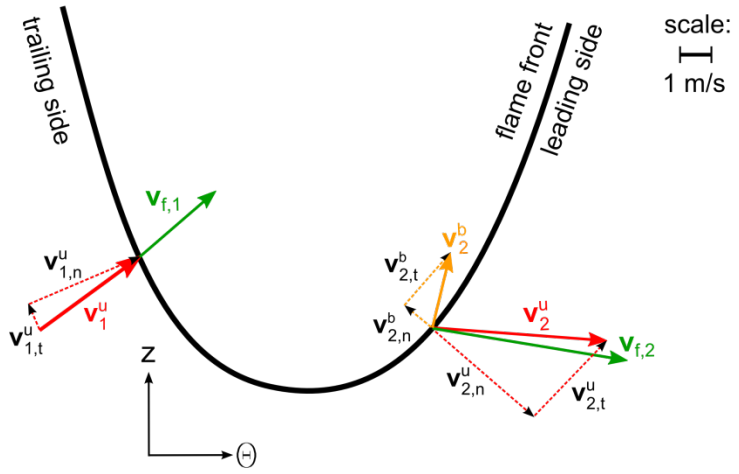

Figure 5.16: Schematic diagram showing measured velocities associated with flame tongues Red arrows: Modified unburnt velocity field at $r \approx 1.0$ mm. Green arrows: Lab-frame flame propagation of local flame elements. Orange arrow: Burnt gas velocity. CH_4-air flashback, $\phi = 1.0$.

5.3.4 Effect of burnt gas velocity field on radial pressure gradient

The significant decrease in azimuthal velocity in the burnt gas, together with the lower density, significantly reduces the required centripetal force and so it is reasonable to conclude that the radial pressure gradient is strongly modified locally where a flame tongue is present. To illustrate, radial profiles of the azimuthal velocity component are plotted in Figure 5.17 at two axial locations. The first axial location at z = -61.25 mm, marked as point *A* in Figure 5.14, is downstream of the leading flame front. Hence, the near-wall region at this point is inside the flame tongue and occupied by burnt gas. The dotted vertical line marks the position of the flame front at this axial location. Any fluid to the right is unburnt gas. The second axial location at z = -66.08 mm, marked as point *B* in Figure 5.14, is upstream of the flame tongue. The entire annulus is occupied by unburnt gas at this location.

The instantaneous velocity profile (solid line) *upstream* of the flame tongue essentially follows the mean non-reacting profile (dashed line) at this location. In contrast, the azimuthal velocity is significantly reduced in the burnt gas, as discussed previously based on the vector plots in Figure 5.14. Close to the center body wall (order of quenching distance) it is decelerated to about 0 m/s. Figure 5.17 further shows that the azimuthal velocity is reduced outside of the burnt gas region in the radial direction; i.e. no jump occurs in the azimuthal velocity at the location of the flame front, which is reasonable since the azimuthal velocity component is approximately tangent on the flame surface in this region. The difference in absolute velocity between the instantaneous and

mean profile is approximately constant in the radial portion of the annulus where the azimuthal velocity is affected.

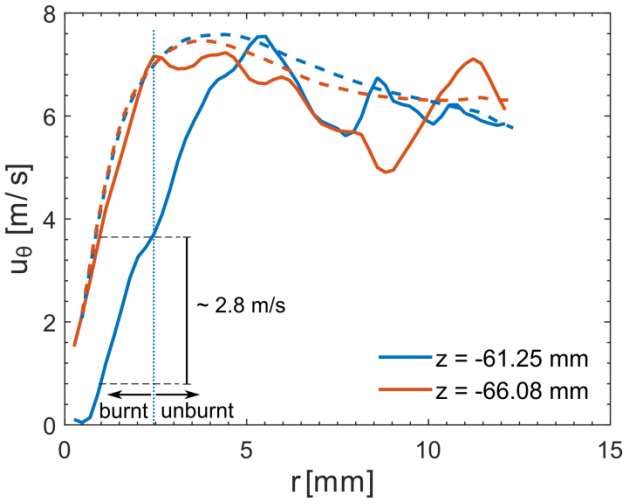

Figure 5.17: Radial profiles of the azimuthal velocity component downstream (blue) and upstream (red) of the leading flame front. The solid lines are instantaneous profiles; the dashed lines are the mean non-reacting profiles. The vertical dotted line marks the flame front location at z = -61.25 mm. CH_4-air flashback, ϕ = 1.0.

In inviscid flow, the radial pressure gradient is related to the centripetal acceleration per the relation

$$\frac{\partial p}{\partial r} \sim \frac{\rho u_\theta^2}{r}. \tag{5.4}$$

As a consequence of Eq. (5.4), the near-wall fluid layer in the burnt gas region, where the azimuthal velocity approaches 0 m/s, does not contribute to the centrifugal force; hence, the radial pressure profile is expected to be flat in this region. Beyond the layer in the radial direction occupied by burnt gas with an azimuthal velocity of about 0 m/s, the slope of the pressure increase with radial distance is strongly reduced compared to

unburnt gas ahead of the flame front, both due to the low density and reduced azimuthal velocity. Integrating the velocity profiles in Figure 5.17 according to Eq. (5.4) using an unburnt gas density of 1.2 kg/m³ and a burnt gas density of 0.16 kg/m³ (factor of 7.5 lower) yields a reduction in pressure difference between center body and mixing tube wall of about 10 Pa. Theoretical models solving the integral momentum equations for a rotationally symmetric swirl flame propagating axially and for a circumferentially-propagating, asymmetric flame, respectively, predict a pressure difference between unburnt and burnt gas of the same order [51,55].

The reduced radial pressure gradient may lead to a decrease in absolute static pressure at the outer (mixing tube) wall, to an increase at the center body wall, or a combination of both. Therefore, without a direct measurement of the radial pressure gradient at an instance when a flame tongue swirls by, it remains unclear whether a reduced radial pressure gradient contributes to an increase in absolute pressure near the center body wall and hence to a strengthening of the blockage effect.

5.4 The effect of hydrogen addition on flashback

The equivalence ratio at which flashback occurs decreases with increasing hydrogen content as indicated by the dashed line in Figure 5.1. The increase in flashback propensity with hydrogen content is expected and in line with boundary layer flashback limits in non-swirling pipe or channel flows [17,18], flashback in low-swirl burners [153], flashback in swirl burners without center body [52] and flashback in swirl burner

with central fuel tube [154]. Precise flashback limits are burner specific and hence not the focus in this work. Instead, the effect of hydrogen addition on the flow-flame interaction during the upstream flame propagation is investigated.

The decrease in equivalence ratio (at which flashback occurs when the hydrogen content is increased) is correlated with a significant decrease in the density ratio and unstretched laminar flame speed. As illustrated in Figure 5.1, for a fixed bulk flow rate of 5.0 m/s, CH_4-air flames flashed back at approximately stoichiometric conditions and hence a density ratio of 7.5 and a flame speed of s_L^0 = 0.38 m/s. In contrast, H_2/CH_4-air flames with 75% H_2 by volume flashed back at an equivalence ratio of about $\phi = 0.4$, which corresponds to a density ratio of 4.4 and a computed flame speed of s_L^0 = 0.05 m/s (Section 5.1).

High-hydrogen content flames were found to qualitatively propagate upstream the same way as methane flames, i.e. in form of flame tongues that swirl in the bulk flow direction as they propagate upstream. This finding was discussed in Section 4.3 for a bulk flow velocity of 2.5 m/s and still holds at twice the bulk flow velocity and the conditions covered by the data set investigated in this chapter and summarized in Section 5.1.

5.4.1 Differences in the burnt gas velocity field

The velocity field associated with an H_2/CH_4-air flashback with 50% H_2 at $\phi = 0.5$ is presented in Figure 5.18 in a radial-axial slice. The leading side of a flame tongue is in the field-of-view at the presented instant in time (Figure 5.18a). The axial velocity is

decreased upstream of the flame tongue and a region of negative axial velocity exists in the vicinity of the leading flame tip (Figure 5.18b) similar to the CH_4-air case (Figure 5.10b). On the other hand, the acceleration of the burnt gas in the axial direction is more gradual compared to the CH_4-air flame, which may be attributed to the lower density ratio.

The azimuthal velocity is again decelerated in the burnt gas (Figure 5.18c). However, the reduced azimuthal velocity appears to be higher at any given radial location inside the burnt gas compared to the CH_4-air flame (Figure 5.10c).

The radial velocity component tends to be positive on the unburnt side of the flame front (Figure 5.18d) in agreement with the CH_4-air flame (Figure 5.10d). The burnt gas velocity field, however, is characterized by a radial velocity of about 0 m/s in contrast to the CH_4-air flame, which showed a larger region of negative radial velocity. A statistical evaluation yields that the mean and median radial velocity in the burnt gas is about 0 m/s for flashbacks with 75% and 50% hydrogen, but shifts towards negative values for lower hydrogen contents.

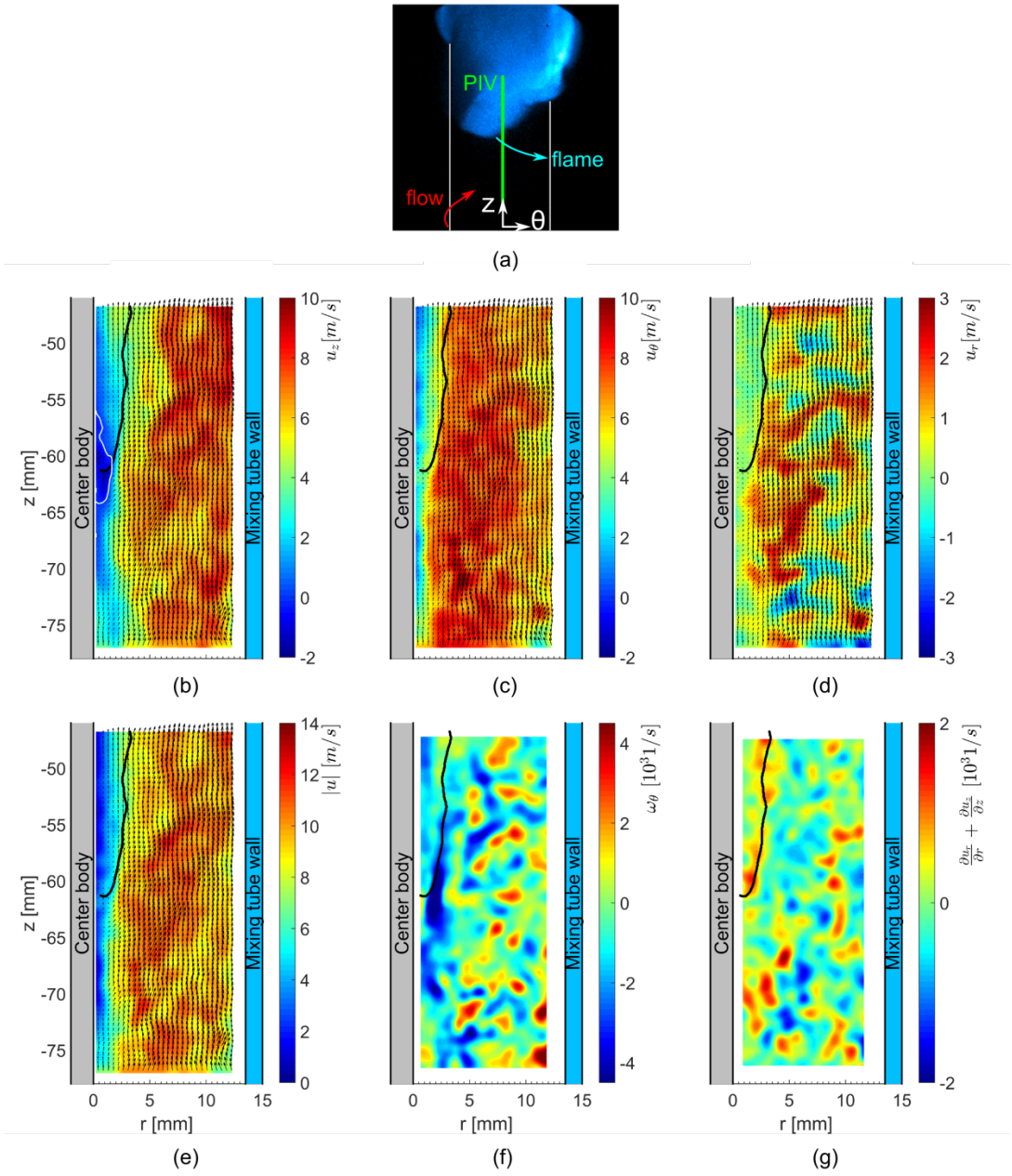

Figure 5.18: H_2/CH_4-air flashback with 50% H_2 by vol. at $\phi = 0.5$. (a) Luminescence image providing the flame tongue location in relation to the laser sheet, (b) axial velocity, (c) azimuthal velocity, (d) radial velocity, (e) velocity magnitude, (f) azimuthal vorticity and (g) in-plane dilatation. Black line: flame front. White line: 0 m/s isoline.

A layer of negative azimuthal vorticity is again found upstream and along the flame front in the vicinity of the flame tip (Figure 5.18f). The magnitude of the azimuthal vorticity in this region is about the same or even higher compared to the CH_4-air flame (Figure 5.10f). The structure and location of this layer of increased negative azimuthal vorticity further supports the argument made in Section 4.5.2 that the production of vorticity by baroclinic torque is not a dominant source.

The location of the flame front is again correlated with a consistently positive in-plane dilatation in the velocity field (Figure 5.18g). However, the magnitude is smaller compared to the CH_4-air flashback, which is reasonable considering that the density ratio is smaller. To explore this effect further, Figure 5.19 shows the measured in-plane dilatation, serving as a proxy for the full 3D dilatation, for a range of hydrogen content, equivalence ratio and bulk flow velocity. The error bars correspond to the standard deviation obtained from three separate runs per condition. The plot captures the expected trend that the dilatation across the flame front increases with an increasing density ratio. For a given hydrogen content, the dilatation consistently increases with an increase in equivalence ratio. The mean dilatation for the stoichiometric CH_4-air flame and the H_2/CH_4-air with 75% hydrogen ($\phi = 0.4$) is measured for both the 2.5 m/s and 5.0 m/s bulk flow velocity. An increase in bulk flow velocity by a factor of 2 does not lead to a significant change in dilatation. However, the uncertainties are too large to comment quantitatively on the effect an increase in reaction rate associated with the higher bulk flow velocity (i.e. more turbulent) case has on the dilatation.

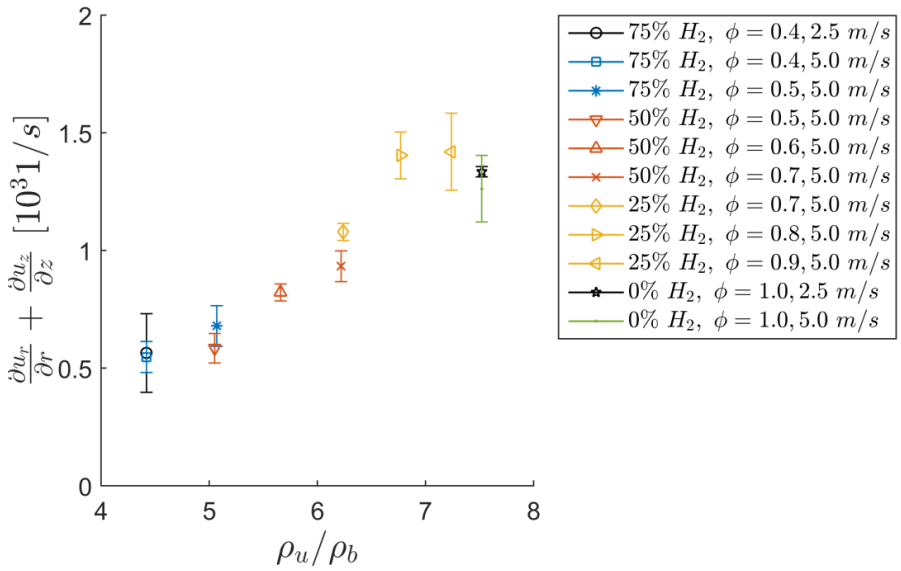

Figure 5.19: 2D-dilatation in the velocity field along the flame front as a function of the density ratio (based on the adiabatic flame temperature) for different hydrogen contents, equivalence ratios and bulk flow velocities. Error bars denote the standard deviation of three separate runs for each condition.

The vector fields in time-z-space are plotted at two radial locations in Figure 5.20 in analogy to the vector plots of a CH_4-air flashback in Figure 5.14. The burnt gas region is again marked by a grey background and the lab-frame propagation direction of the leading side of the flame tongue is indicated by the blue arrow. The velocity field in the unburnt gas of this H_2/CH_4-air flashback qualitatively agrees with all previous findings based CH_4-air flashbacks. In particular, the velocity field upstream of the flame tip and ahead of the leading side of the flame tongue is again characterized by a predominantly swirling motion with a small negative axial velocity component. Furthermore, the azimuthal velocity is again reduced inside the burnt gas of flame tongues.

Despite the similarities with the CH_4-air case, there are some differences. The quantitative differences are best illustrated with the contour plots shown in Figure 5.21. The azimuthal and axial velocity field at $r = 0.9$ mm for a stoichiometric CH_4-air flashback are shown in Figure 5.21a and b, respectively. The same vector field was previously shown without the velocity contours in Figure 5.14b. The flame front is now outlined by the black solid line. The corresponding azimuthal and axial velocity field at the same radial location for the H_2/CH_4-air flashback investigated in this section is shown in Figure 5.21c and d, respectively.

The axial velocity reaches negative values of about -0.5 m/s upstream of the flame tip and ahead of the leading side of the flame tongue in both cases. However, the acceleration of the burnt gas in the axial direction, which is very gradual in both cases, reaches much higher values in the CH_4-air flashback (Figure 5.21b) compared to the H_2/CH_4-air flashback (Figure 5.21d). As an example, about 40 mm downstream of the leading flame tip (which is beyond the field-of-view in Figure 5.21), the axial velocity of the burnt gas of the CH_4-air flashback reaches 20 m/s in contrast to merely 10 m/s for the H_2/CH_4-air flashback. This difference may be attributed to the smaller density ratio of the H_2/CH_4-air flame in addition to the smaller rate at which reactants are consumed.

The deceleration of the burnt gas in the azimuthal direction is not as strong for H_2/CH_4-air flashback compared to the CH_4-air flashback. The final reduced azimuthal velocity is about 1.5 m/s within the core region of the flame at $r = 0.9$ mm (Figure 5.21c).

In contrast, the azimuthal velocity is decelerated to about 0 m/s at the same radial location in the case of the CH_4-air flashback (Figure 5.21a).

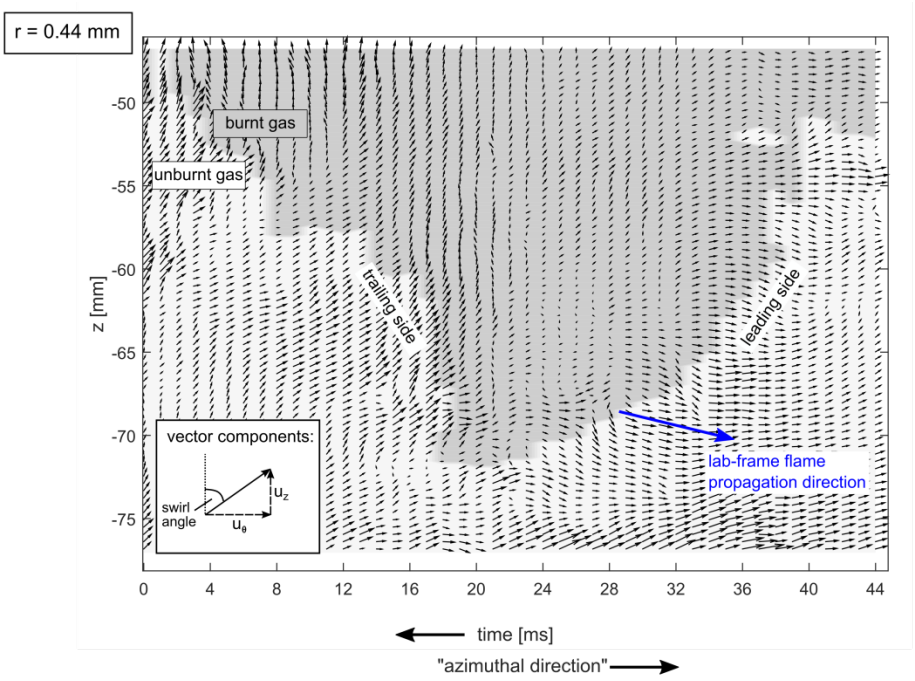

(a)

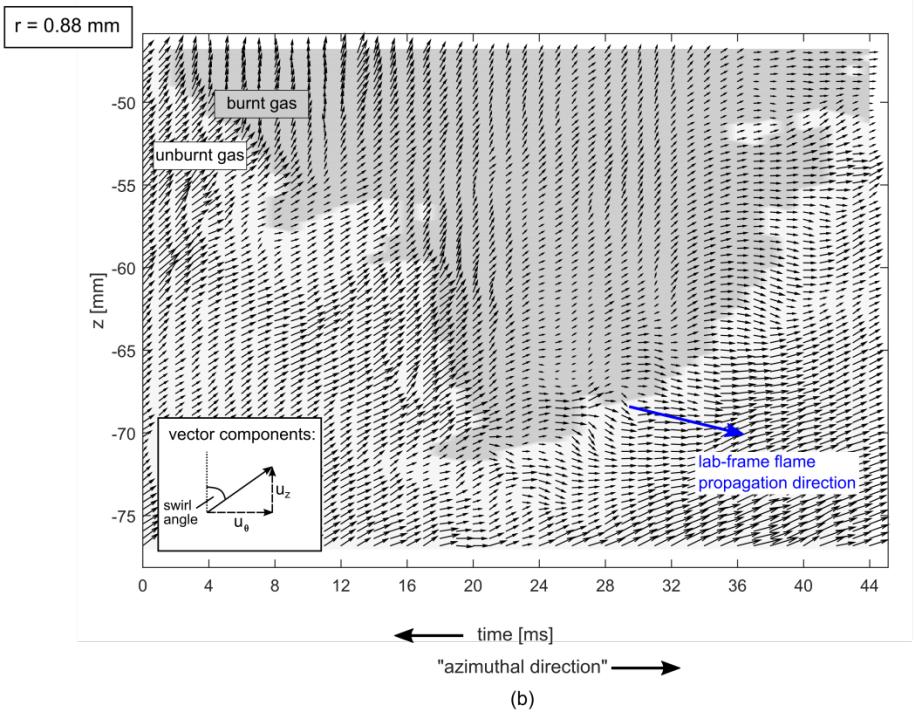

(b)

Figure 5.20: Velocity field in time-z-space at radial locations (a) $r = 0.44$ mm, (b) $r = 0.88$ mm. H_2/CH_4-air flashback with 50% H_2, $\phi = 0.5$.

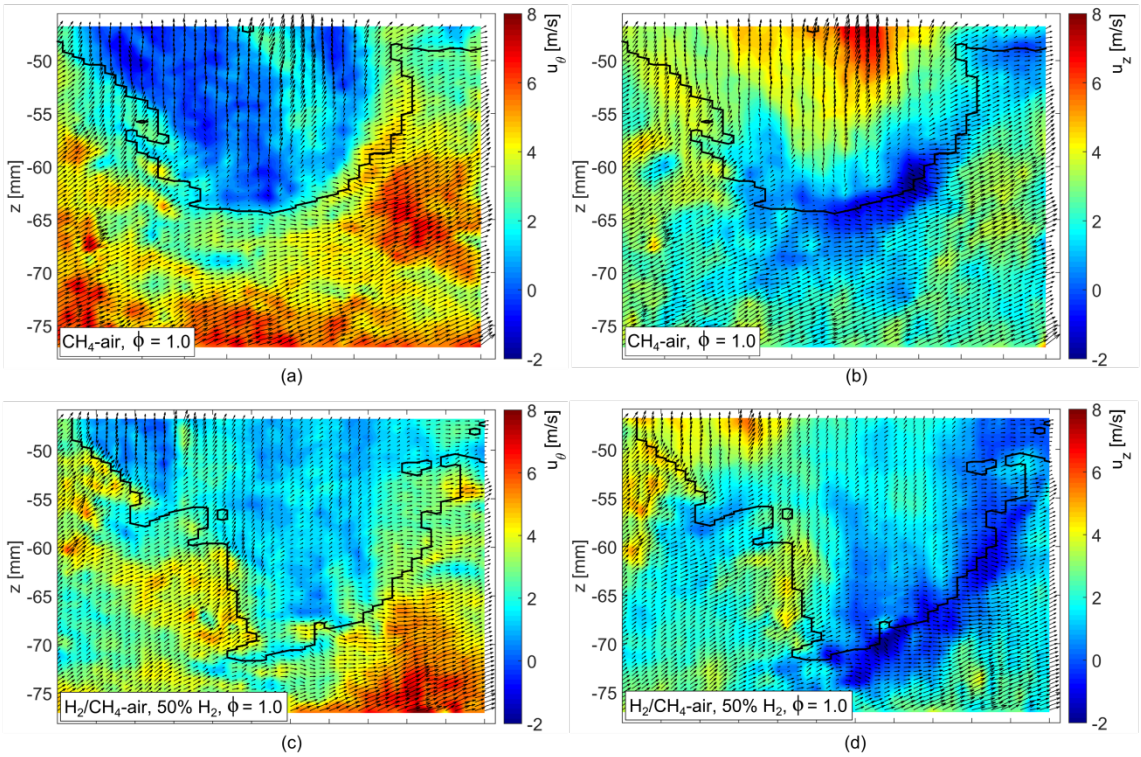

Figure 5.21: Comparison of velocity fields in time-axial plane at $r = 0.9$ mm. (a,b) CH_4-air flashback, $\phi = 1.0$ and (c,d) H_2/CH_4-air flashback with 50% H_2, $\phi = 0.5$. The color map shows the azimuthal (a,c) and axial (b,d) velocity fields. Solid black line marks the flame front.

The change in azimuthal velocity in the burnt gas region with a change in hydrogen content and hence density ratio and flame speed is found to follow a general trend. The median azimuthal velocities in the burnt gas are evaluated at a fixed radial position of $r = 0.9$ mm and plotted for the different hydrogen contents (for the equivalence ratios closest to the flashback limit) in Figure 5.22. The error bars correspond to the standard deviation in the median value from three separate runs for each condition. Figure 5.22 shows the general trend that, at a fixed radial position, the

burnt gas is decelerated to a lower azimuthal velocity with an increase in density ratio. This trend confirms what the comparison of velocity field corresponding to 0% H_2 (Figure 5.21a) and 50% H_2 (Figure 5.21c) had already suggested.

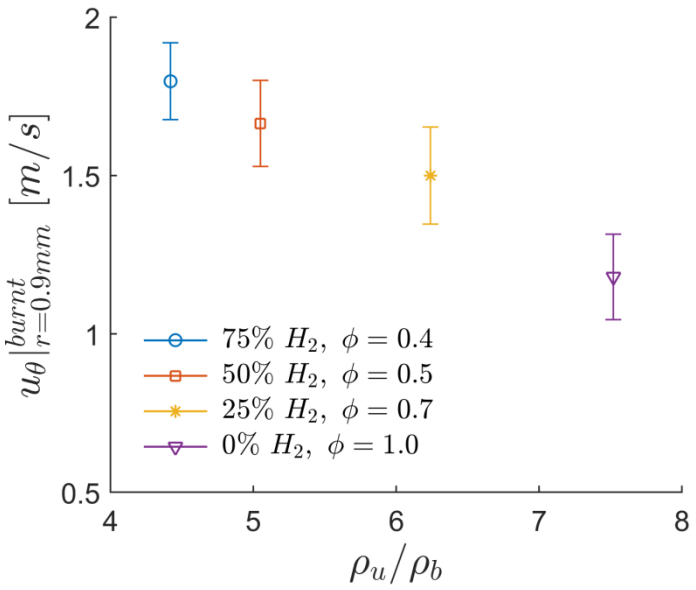

Figure 5.22: Median azimuthal velocity in burnt gas at a fixed radial location of $r = 0.9$ mm for flashbacks ranging from 0% to 75% hydrogen. Error bars denote standard deviation from three different runs for each condition.

The correlation between higher (or less reduced) azimuthal velocity and smaller density ratio supports the argument that the burnt gas velocity field is governed by the constraint imposed by the flow processed along the leading side of the flame tongue as the following discussion shows. This argument was made based on the CH_4-air flashback in Section 5.3.3. In analogy to the previous discussion and Figure 5.16, the actual velocities associated with a flame tongue at $r \approx 1.0$ mm are now evaluated for the H_2/CH_4-air flashback with 50% H_2 ($\phi = 0.5$) as shown in Figure 5.23. The azimuthal

velocity upstream of the trailing side is decelerated to about 3.5 m/s compared to about 3.0 m/s for the CH_4-air flashback. Flame elements along the trailing side are propagating downstream as indicated by the green vector $\boldsymbol{v}_{f,1}$. On the leading side, the unburnt velocity $\boldsymbol{v}_2^u$ (red arrow) has a negative axial component of about -0.5 m/s, which is comparable to the CH_4-air flashback. The azimuthal component is about 4.0 m/s.

The lab-frame flame propagation velocity of the leading side is again approximately known from the high-speed chemiluminescence movies, which suggest that the flame tongues swirl slightly slower with about 4.8 m/s compared to the 5.2 m/s measured for the CH_4-air flashback. The propagation of the flame tongue in the negative axial direction (global flashback speed) is slightly lower (about -0.7 m/s compared to about -1.1 m/s), which is partially attributed to the lower turbulent displacement speed (owing to the low equivalence ratio) of the H_2/CH_4-air flame compared to the CH_4-air The turbulent displacement speed may again be calculated according to Eq. (5.1), which agrees well with the estimate of about 0.5 m/s (Appendix C).

The burnt gas velocity is computed by applying the jump condition Eq. (5.2) and solving Eq. (5.3) for $\boldsymbol{v}^b$. The obtained vector is included in Figure 5.23 (orange vector), which is again motivated by the fact that the computed burnt gas velocity vector on the leading side agrees well with the measured velocity field in the center of the burnt gas region enclosed by the convex-shaped flame tongue. The burnt gas along the leading side of the flame tongue is again accelerated in the negative azimuthal direction and hence imposes a blockage on the burnt gas process by the trailing side, which wants to

accelerate in the positive azimuthal direction. However, the azimuthal component of the burnt gas velocity field is not reduced as much compared to the CH_4-air flame primarily because the density ratio is lower (density ratio of 5 compared to 7.5). The final burnt gas velocity at a radial location of about $r \approx 1.0$ mm has a positive azimuthal component of about 1.5 m/s as discussed previously and shown in Figure 5.20 and Figure 5.21. in contrast to the CH_4-air flashback where the burnt gas is decelerated to an azimuthal velocity of about 0 m/s at the same radial location.

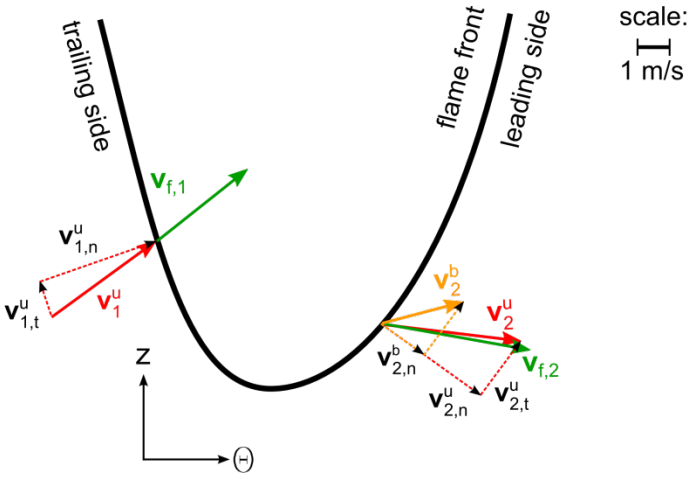

Figure 5.23: Schematic diagram showing the measured velocities associated with flame tongues. Red arrows: Modified unburnt velocity field at $r \approx 1.0$ mm. Green arrows: Lab-frame flame propagation of local flame elements. Orange arrow: Burnt gas velocity. H_2/CH_4-air flashback (50% H_2, $\phi = 0.5$).

The quantitative difference in the azimuthal velocity field in the burnt gas region between the H_2/CH_4-air flashback and the CH_4-air flashback may suggest that the

blockage is not as strong. However, the strength of the blockage effect is measured by the change in momentum it induces, not the change in velocity. Since the burnt gas density of the H_2/CH_4-air flame is higher by a factor of 1.5 compared to the CH_4-air flame, the more moderate deceleration in the azimuthal direction is partially compensated (with respect to the momentum change) by the higher density. The change in azimuthal momentum upstream of the trailing side of a flame tongue is proportional to $\rho^u \cdot \left(u_{\theta,1}^2 - u_{\theta,2}^2\right)$. Inside the burnt gas the momentum change is proportional to $\rho^b \cdot \left(u_{\theta,2}^2 - u_{\theta,3}^2\right)$. The H_2/CH_4-air flame tongue decelerates the azimuthal velocity from about 4 m/s to about 3.5 m/s upstream of the trailing side, and from about 3.5 m/s to about 1.5 m/s inside the burnt gas. The CH_4-air flashback flame tongue decelerates the azimuthal velocity from about 4 m/s to about 3 m/s upstream of the trailing side, and from about 3 m/s to about 0 m/s in the burnt gas. The difference in momentum change is then merely about 30% between the two flames. The strength of the blockage effect therefore appears to be on the same order for the two different flashbacks, which suggests that the azimuthal pressure gradient required to decelerate the flow in the azimuthal direction is on the same order.

5.4.2 The role of the quenching distance

The velocity field measurements have shown that the flame speed and the local velocity vector at the tip and along a portion of the leading side of flame tongues are both pointing in the negative axial direction rather than opposing each other (Figure 4.8, Figure 5.14 and Figure 5.20). Therefore, the quenching distance does not matter

according to the physical picture originally proposed by Lewis and von Elbe [10,11]. In that model, the flame speed and flow velocity oppose each other and flashback occurs when the flame speed exceeds the flow velocity about one quenching distance away from the wall. In contrast, recent studies of boundary layer flashback in non-swirling flows show that during flashback reverse flow pockets formed by convex-shaped bulges reach well above the quenching distance [24,25]. Similarly, in boundary layer flashback of swirl flames, the present work shows that a near-wall layer of fluid is deflected by the flame tongues such that a region of predominantly swirling flow with a small negative axial velocity forms ahead of the flame.

Adding hydrogen to a methane flame generally decreases the quenching distance. However, whereas the quenching distance of a H_2/CH_4-air flame decreases with increasing hydrogen content *for a fixed equivalence ratio*, it increases with decreasing equivalence ratio for a fixed hydrogen content [155]. Experimental data on quenching distances of H_2/CH_4-air flames for a range of hydrogen volume fractions and equivalence ratios is sparse. Different definitions, different experimental methods to measure quenching distances and the dependency of the quenching distance on the flame-wall interaction (e.g. side-wall versus head-on quenching) further complicate the availability of applicable precise, quantitative values. The quenching distance in a head-on quenching configuration for stoichiometric methane-air flames is about 0.2 mm based on wall-normal temperature measurements [156] and flame luminescence images [157]. In the case of side-wall quenching, which is applicable to the flame propagation along the

center body wall in this work, the quenching distance for stoichiometric methane-air flames increases to about 0.35 mm [157]. Alternatively, quenching distances may be determined based on the minimal gap height a flame can propagate through, which leads to larger values. Quenching distances measured and defined that way are about 2.0 mm and 0.65 mm for stoichiometric CH_4-air flames and stoichiometric H_2-air flames, respectively [158,159]. The same measurement technique has been applied to H_2/CH_4-air flames for up to 50% H_2 and equivalence ratios as low as 0.63 [155]. The measured values for a few conditions are listed in Table 5.2. The absolute values are not expected to be applicable for the flames investigated in this work (side-wall quenching), but the trends are expected to hold. The conditions highlighted in bold letters are close to conditions at which flashback occurred in the swirl combustor investigated in the present work at a bulk flow velocity of 5.0 m/s. Despite the increase in hydrogen content, these values suggest that the quenching distance is approximately constant at the conditions when flashback occurs owing to the decrease in equivalence ratio correlated with the increase in hydrogen volume fraction. Assuming that this trend still holds for side-wall quenching, the quenching distance at the flashback limit is about 0.35 mm (corresponding to a stoichiometric CH_4-air flame [157]) for all investigated flames at a bulk flow velocity of 5.0 m/s.

% CH_4	% H_2	ϕ	d_{quench} [mm]
100	**0**	**1.0**	**2.13**
100	0	0.83	2.41
76.9	23.1	0.83	2.07
76.9	**23.1**	**0.71**	**2.46**
52.6	47.4	0.71	1.85
52.6	**47.4**	**0.63**	**2.23**

Table 5.2: Quenching distances for H_2/CH_4-air flames according to [155].

Since the axial momentum flux increases with distance from the center body wall in the boundary layer, the thinner the layer that needs to be deflected for flashback to occur, the weaker the force that a flame tongue is required to exert on the approach flow. A quenching distance that is about the same for the different flames at the conditions at which flashback occurs may suggest that the strength required by the flame tongues to deflect the flow in the negative axial direction is about the same. The force exerted on the approach flow by the different flames may be quantified by evaluating the radial extent (or height above the center body wall) of the region of negative axial velocity. The mean radial extent is plotted for a range of conditions in Figure 5.24. The error bars denote the standard deviation of three separate flashbacks. Note that the peak heights of these regions of negative axial velocity are about 1 to 2 mm as seen previously in the instantaneous velocity fields (e.g. in Figure 5.10 and Figure 5.18).

The sizes of the negative axial-velocity regions are fairly constant across the different H_2/CH_4-air flames, and hence appear to be largely insensitive to variations in

density ratio and flame speed. These data then suggest that the force exerted on the approach flow by the different flames is approximately the same despite the differences in density ratios and flame speeds. The finding that the force exerted on the approach flow is approximately the same for such varying conditions then suggests that the quenching distance determines the adverse axial pressure gradient needed to the deflect the flow in a way that flashback occurs. However, a quantitative comparison shows that the maximum radial extent of the negative axial velocity regions (1 to 2 mm) is significantly larger than the quenching distance (0.35 mm) at conditions when flashback occurs.

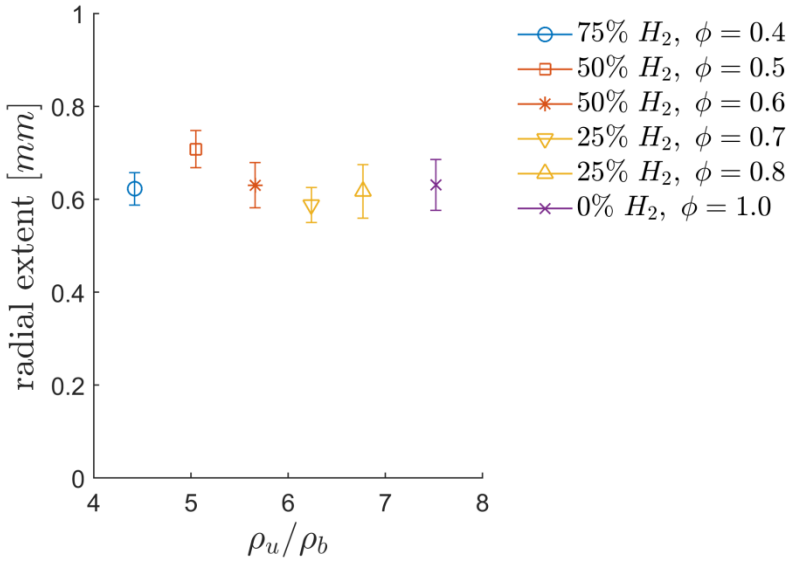

Figure 5.24: Mean radial extend (or height above the wall) of regions of negative axial velocity. Error bars denote standard deviation from three different runs for each condition.

5.5 Summary

Predominantly swirling flow with a region of negative axial velocity that reaches beyond the quenching distance already exists prior to flashback along the center body wall close to the mixing tube exit (Section 5.2). Furthermore, convex shaped flame tongues are found to already penetrate into the mixing tube without initiating sustained upstream flame propagation at conditions close to the flashback limit (Section 5.2.2).

Once the conditions are favorable, flashback occurs in the form of large-scale convex-shaped flame tongues, which significantly deflect the approach flow (blockage effect) allowing them to propagate in the negative axial direction while swirling in the direction of the bulk flow (Chapter 4). Detailed measurements of the planar, three-component velocity in the unburnt *and* burnt gas velocity field (Section 5.3 and Section 5.4) revealed new insights into how gas dilatation leads to a significant blockage effect and hence into the mechanism driving flashback.

In the absence of any confinement, gas dilatation primarily acts on the burnt gas as opposed to the unburnt gas. The burnt gas has a much lower density and hence accelerating it requires less force than accelerating (or decelerating) the high-density unburnt gas. However, if some constraint restricts the expansion and acceleration of the burnt gas, such as in a spherically expanding flame, gas dilatation has no other chance but to exert a significant force on the approach flow, which manifests itself in a more severe blockage effect.

Inside the burnt gas region of flame tongues, the radial velocity is approximately zero (Figure 5.18) or moderately negative (Figure 5.10). At the same time, the radial velocity field in the unburnt gases shows that the flow is pushed towards the outer (mixing tube) wall by the flame front. These observations were explained by the constraint the center body wall imposes on the burnt gas velocity field, i.e., 0 m/s radial velocity at the wall (Section 5.3.2). For the portions of the flame surface that are vertical (i.e. the flame-normal vector is aligned with the radial direction), the acceleration of the burnt gas normal to the flame front and hence towards the center body wall is restricted. Instead, the unburnt gas ahead of the flame front is pushed towards the outer wall, which is correlated with an acceleration in the axial direction similar to boundary layer flashback in (non-swirling) channel flows where blockage near both walls leads to an acceleration of the flow on the center line [26]. In contrast to channel flashback, the flow is also accelerated in the axial direction on the opposite side of the center body, since flame tongues only occupy a portion of the annulus in the azimuthal direction.

An additional constraint is identified, which acts in the azimuthal direction. The acceleration of reactants processed by the leading side of the flame tongues, by geometry, leads to a deceleration in the azimuthal direction. The burnt gas along the leading side hence imposes a blockage effect on the gas processed by the trailing side, which, in the absence of any constraint, would otherwise accelerate in the positive azimuthal direction (Section 5.3.3). The blockage effect is coupled with the formation of an azimuthal pressure gradient. The azimuthal pressure gradient reduces the azimuthal momentum of

the approach flow ahead of the trailing side and the azimuthal momentum inside the burnt gas to fulfill the constraint on the velocity field imposed by the leading side. The reduced azimuthal momentum corresponds to a reduction in azimuthal velocity (Figure 5.21). At the same radial position, the reduction in azimuthal velocity of the burnt gas was found to be less severe for flames with a higher burnt gas density (lower density ratio across the flame front) and lower flame speed (Section 5.4.1). This trend supports the argument that the origin for the blockage effect lies in the gas processed by the leading side of the flame tongues, as the theoretical analysis based on applying the jump conditions showed. Even though the azimuthal velocity in the burnt gas changes with a change in density ratio and flame speed, the change in momentum and hence the strength of the blockage effect was argued to change little between different flames (Section 5.4.1).

The blockage effect due to the constraints on the burnt gas velocity field in the radial and azimuthal direction acts in all directions; hence, it also reduces the axial momentum. The resulting reduction in axial velocity and the deflection of the flow around the leading tip of the flame tongues was discussed in the previous chapter (Section 4.5.2). The velocity field ahead of the flame tip and the leading side of the flame tongue is characterized by a predominantly swirling motion with a small negative axial velocity component. The measurements presented in this chapter further show that the region of negative axial velocity reaches well within the burnt gas (Figure 5.10 and Figure 5.18).

As a consequence of the decelerated axial and azimuthal velocity in addition to a radial velocity of about 0 m/s, a small region *inside* the burnt gas exists at $r \approx 1$ mm where the flow is essentially stagnant in the case of the CH_4-air flashback (Figure 5.14b). However, such a well-defined region of stagnant flow is not found for the H_2/CH_4-air flashbacks with high hydrogen content where, as discussed before, the azimuthal velocity in the burnt gas region is not reduced to 0 m/s (Figure 5.20b). A stagnation region sufficiently offset from the wall hence does not appear to be a prerequisite for flashback to occur.

The thickness of the layer of negative axial velocity was evaluated for the flames with different hydrogen contents (different density ratios and different flame speeds) and found to be approximately constant but larger than the quenching distance. The results suggest that the force exerted on the approach flow at the conditions when flashback occurs is approximately constant for the different flames despite the differences in density ratio and flame speed.

Chapter 6: Summary and Future Work

Boundary layer flashback of swirl flames was investigated experimentally in a new model swirl combustor, which features a mixing tube with an axial swirler and attached cylindrical center body. Flashbacks of lean-premixed H_2/CH_4-air flames with up to 95% H_2 by volume were investigated at atmospheric pressure and bulk flow velocities up to 5.0 m/s. The focus of the present work was on the upstream flame propagation inside the mixing tube, which occurred along the center body wall. The mixing tube wall was made of fused silica to provide the necessary optical access. Stereoscopic PIV at kHz-rate was applied to obtain the time-resolved, planar, three-component velocity field in radial-axial planes. The flame front was detected based on the acquired Mie scattering images. Either oil droplets, which evaporated in the preheat zone, or the sudden change in particle number density were utilized as a marker for the flame front. The chemiluminescence was imaged simultaneously at kHz-rate to provide the flame shape and global flame propagation direction. The luminescence image sequences further provided the location of the flame relative to the laser sheet, which proved to be crucial for an unambiguous interpretation of the planar data in this highly three-dimensional flow.

A technique capable of reconstructing the three-dimensional flame topography was developed as part of the present work. The main features of the technique are summarized in Section 6.1. The focus of the present work was on advancing the understanding of the physical mechanism driving flashback in swirl flame boundary layer

flashback. The findings are summarized in Section 6.2. Each section concludes with suggestions for future work.

6.1 3D flame front detection and velocity field measurement technique

A technique to simultaneously measure the time-resolved 3D flame topography and volumetric velocity field was developed and applied to study the upstream flame propagation along the center body wall inside the mixing tube. The measurement volume was about 30 x 30 x 5 mm^3. Olive oil droplets that vaporize in the preheat zone of the flame were utilized as a marker for the flame front. The droplets were illuminated with a laser at kHz-rate and the Mie scattering was imaged with four high-speed cameras. A tomographic reconstruction was performed to obtain the volumetric particle field. The void regions in the reconstructed particle field, which correspond to burnt gas, were contaminated with reconstruction artifacts (ghost particles). A correlation between particle number density and peak particle intensity evaluated in interrogation volumes was found to reliably discriminate between unburnt and burnt gas despite the ghost particles at the expense of a reduced spatial resolution.

The volumetric velocity in the unburnt gas was measured simultaneously by means of tomographic PIV. The reconstructed void region in the particle field provided an algorithmic mask, which was applied prior to the cross-correlation to prevent ghost particles dominating the cross-correlation in interrogation volumes near the flame surface. The computed volumetric velocity field in turn was utilized to improve the

reconstructed particle field in a second iteration by taking advantage of the time-resolved measurements and the fact that ghost particles do not follow the velocity field. The improved volumetric particle field led to a better reconstruction of the flame surface.

The 3D flame topography was validated against four redundant, simultaneously detected, planar flame fronts based on the same marker (i.e. the location where oil droplets evaporate). The mean error based on the distance between the most probable planar flame front and the 3D flame surface was 0.4 mm. Cusps along the flame front as small as 1 to 2 mm were found to be resolved. The volumetric velocity field was validated against two redundant sets of planar, three-component velocity fields measured by means stereoscopic PIV. The mean error associated with the volumetric velocity field was 0.6 voxels (0.2 m/s).

The present work demonstrates the feasibility of inferring the three-dimensional flame front from a reconstructed field of droplets. The current approach is, however, limited to a simultaneous velocity measurement in the unburnt gas owing to the need of utilizing the vaporization of droplets rather than a change in number density of particles as the marker for the flame front. Furthermore, the spatial resolution of the flame topography is limited by the need to average over a fairly large number of reconstructed droplets owing to the remaining level of ghost particles. Both limitations may be remedied in the future if the technique is combined with a recent advancement in tomographic PIV, which successfully demonstrated the reconstruction of individual particles including their precise location followed by a Lagrangian tracking, as opposed

to a voxel based reconstruction of intensity blobs followed by a cross-correlation [160,161]. Such an approach may lead to a negligible number of ghost particles even for Mie scattering images with high background intensity and hence allow the extraction based on particle number density combined with an increase in spatial resolution of the reconstructed flame front.

The developed technique may also be applied to reconstruct the luminescence from thermographic phosphor particles. A planar technique to simultaneously measure the temperature field and velocity field based on such phosphor particles has recently been demonstrated [94,95]. The luminescence intensity emitted by some thermographic phosphors conveniently disappears at temperatures of about 1000 K [96], which may serve as a marker for a flame front that is closer to the reaction zone compared to the evaporation of olive oil droplets at about 550 K.

6.2 Physics of swirl flame flashback

Flashback was found to occur in the form of large-scale flame tongues swirling along the center body wall. The term “flame tongue” was used in this work to emphasize that flame fronts leading flashback are not axisymmetric but instead have a convex shape (convex toward the unburnt gas) and have a characteristic width on the order of the center body diameter. The spatial scale distinguishes them from smaller-scale flame bulges, which were observed along the trailing side of the flame tongues. Similar small-scale, convex-shaped flame bulges, which counter-propagate into the approach flow in low-

momentum regions, were previously found to lead boundary layer flashback in (non-swirling) channel flows [24,25].

Instead of counter-propagating into the approach flow in the negative streamwise direction, flame-tongues propagate with the bulk flow in the positive azimuthal direction while flashing back in the negative axial direction. The flame tongues strongly modify the approach flow. A region of negative axial velocity in the vicinity of flame tongues was already observed in a previous study [48]. The planar three-component and volumetric velocity measurements in the present work revealed that this region of negative axial velocity, which was previously interpreted as boundary layer separation or flow recirculation, is instead merely the result of a 3D deflection of streamlines. The flow field along the leading side of the flame tongues is found to be characterized by a predominantly swirling fluid motion with a small negative axial velocity component. No stagnation point exists upstream of the leading flame tip.

At the tip and along the leading side of the flame tongue the flame speed acting normal to the flame front and the local velocity vector on the unburnt side both point in the negative axial direction. Flashback is hence not facilitated by an imbalance between an opposing local flow velocity and the flame speed. Instead, flashback is facilitated by the blockage effect that the flame tongues impose on the approach flow.

This blockage effect is attributed to the gas dilatation associated with the heat release. In premixed flames, dilatation has a much stronger effect on the low-density burnt gas than on the unburnt gas unless some constraint on the velocity field limits or

prevents the expansion and hence acceleration of the burnt gas. The effect of gas dilatation on the flow field in the vicinity of the flame tongues was studied in detail based on planar, three-component measurements in the unburnt *and* burnt gas. The measurements suggest two dominating constraints on the burnt gas velocity field. First, the flame was found to push the flow toward the outer (mixing tube) wall, which was attributed to the center body wall imposing a constraint on the radial velocity field by limiting the acceleration of burnt gases in the negative radial direction (i.e., toward the wall). A similar blockage effect in the wall-normal direction was identified in channel flashbacks [26]. Second, the gas processed by the leading side of the flame tongues is accelerated in the negative azimuthal direction, which imposes a constraint on the azimuthal momentum on the unburnt gas upstream of the trailing side and on the burnt gas region. As a result, the azimuthal velocity inside the burnt gas region was significantly reduced.

Adding an increasing amount of hydrogen to a methane-air flame decreased the equivalence ratio at which flashback occurred significantly. For instance, at a bulk flow velocity of 5.0 m/s, a methane-air flame flashback occured at stoichiometric conditions. In contrast, for a H_2/CH_4-air flame with 75% H_2 by volume, flashback occurred at an equivalence ratio of about 0.4 and hence at a substantially lower density ratio and lower flame speed. However, the radial extent of the regions of negative axial velocity, which may be interpreted as a metric for the strength of the blockage effect, was found to be largely independent to variations in hydrogen content and hence density ratio. Existing

data on quenching distances suggests that the quenching distance at the conditions when flashback occurred was also approximately the same for the different H_2/CH_4-air flames. However, a quantitative comparison shows that the maximum radial extent of the negative axial velocity regions is larger than the quenching distance both at the onset and during flashback.

The following future work is suggested based on the findings in the present work. First, the improved understanding of the mechanism driving swirl flame boundary layer flashback may be used to derive improved models and correlations predicting important quantities such as flashback limits and global flame speeds. The findings suggest that the radial profiles of the axial and azimuthal momentum flux play an important role since they determine the strength of the blockage required by the flame tongue to impose on the approach flow and deflect it. The possibility that the knowledge of a global swirl number and bulk flow velocity for a particular burner and operating condition is not sufficient needs to be investigated. Furthermore, the role of the quenching distance was discussed; however, further investigations are needed to identify the proper quantitative measure of a quenching distance relevant for correlations predicting swirl flame boundary layer flashback.

In the present study, fuel and air were fully mixed upstream of the mixing tube to eliminate any effects due to equivalence ratio stratifications. Further studies are needed to better understand the effect of equivalence ratio stratification on flashback, which may be employed as a strategy for improved flashback resistance.

Furthermore, the measurements in the present work were limited to atmospheric pressure and moderate bulk flow velocities. The question remains whether the described mechanism driving swirl flame boundary layer flashback is different at conditions relevant for gas turbine combustors. Measurements of flashback in the same model swirl combustor have already been conducted at pressures up to 5 atm. The flame propagation direction and velocity field showed the same features, which suggests the mechanism is largely unchanged for an increase in pressure and hence Reynolds number by a factor of 5. However, gas turbine combustors operate at much higher pressures (~ 30 atm), much higher bulk flow velocities in the mixing tube (~ 50 m/s) and elevated inlet temperatures (~ 600 K).

Appendices

Appendix A: Flashback Videos

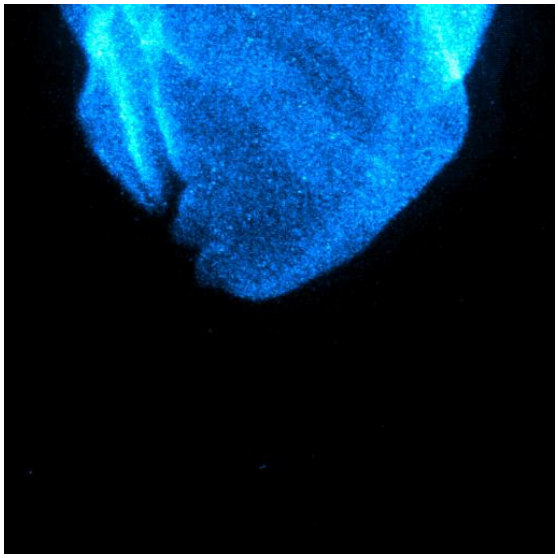

Video 1: Chemiluminescence movie sequence recorded at 4 kHz showing the upstream flame propagation of a CH_4-air flashback ($\phi = 0.8$). Movie corresponds to Figure 4.4a.

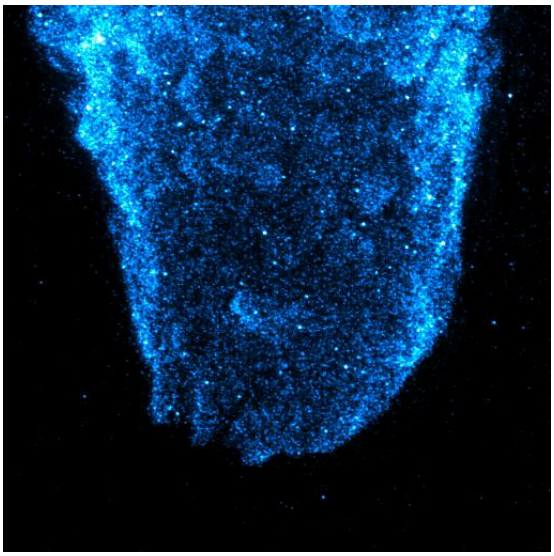

Video 2: Chemiluminescence movie sequence recorded at 4 kHz showing the upstream flame propagation of a H_2/CH_4-air flashback (ϕ = 0.4). Movie corresponds to Figure 4.4b.

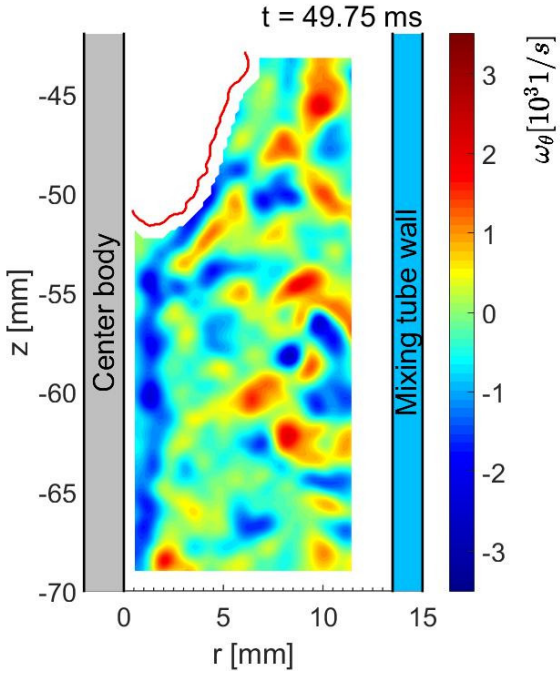

Video 3: Movie sequence showing the azimuthal vorticity field in the vicinity of an upstream propagating flame tongue (red line marks flame front). Temporal resolution: 4 kHz. Movie corresponds to Figure 4.9.

Appendix B: Computed unstretched laminar flames speeds and density ratios for investigated H_2/CH_4-air mixtures

H_2 by *vol.*	ϕ	s_L^0 [m/s]	ρ_u/ρ_b
75%	0.4	0.05	4.4
75%	0.5	0.15	5.1
50%	0.5	0.09	5.1
50%	0.6	0.20	5.7
50%	0.7	0.32	6.2
25%	0.7	0.24	6.2
25%	0.8	0.34	6.8
25%	0.9	0.41	7.2
25%	1.0	0.46	7.6
0%	1.0	0.38	7.5

Table B.1: Investigated H_2/CH_4-air mixtures including computed unstretched laminar flame speeds (using Cantera and GRI3.0 mechanism) and unburnt-to-burnt gas density ratios.

Appendix C: Turbulent displacement speed estimates

The turbulent displacement speeds are estimated for the flame propagation analyses in Section 5.3.3 and Section 5.4.1. The investigated stoichiometric CH_4-air flame has an unstretched laminar flame speed of s_L^0 = 0.35 m/s. The Lewis number is about unity. The flame is hence not responsive to stretch effects. The effect of turbulence on the flame speed is estimated according to [4]

$$s_T = s_L \sqrt{1 + \left(\frac{u'}{s_L}\right)} . \tag{0.1}$$

The turbulent flame speed for the 5.0 m/s bulk flow velocity case is evaluated using the velocity fluctuations in the boundary layer at r = 1.0 mm (u' = 0.65 m/s) instead of the centerline velocity fluctuations. The resulting turbulent flame speed is s_T = 0.74 m/s, which is within in the range of experimental data indicating a turbulent flame speed for stoichiometric CH_4-air flames with rms-velocities of about 0.6 m/s ranging from 0.5 m/s to 1.5 m/s [7].

For a H_2/CH_4-air flame with 50% H_2, flashback occurs at an equivalence ratio of about 0.5. The unstretched laminar flame speed is about s_L^0 = 0.10 m/s. The Lewis number based on the deficient reactants (H_2 and CH_4) is smaller than unity, $Le_{H_2} << 1$ and $Le_{CH_4} < 1$. The diffusivities of H_2 and CH_4 are larger than the diffusivity of oxygen, $D_{H_2} \gg D_{O_2}$ and $D_{CH_4} > D_{O_2}$. Hence, the H_2/CH_4-air flame has a strong response to stretch effects owing to the non-unity Lewis numbers and preferential diffusion [5], which strongly increases the turbulent flame speed even for moderate and strong turbulence [8].

The limited experimental data for very lean H_2/CH_4-air flames ($\phi = 0.5$) with 50% H_2 suggest a turbulent flame speed of about s_T = 0.5 m/s for u' = 0.65 m/s [8,162].

Appendix D: Model swirl combustor and diagnostic setup

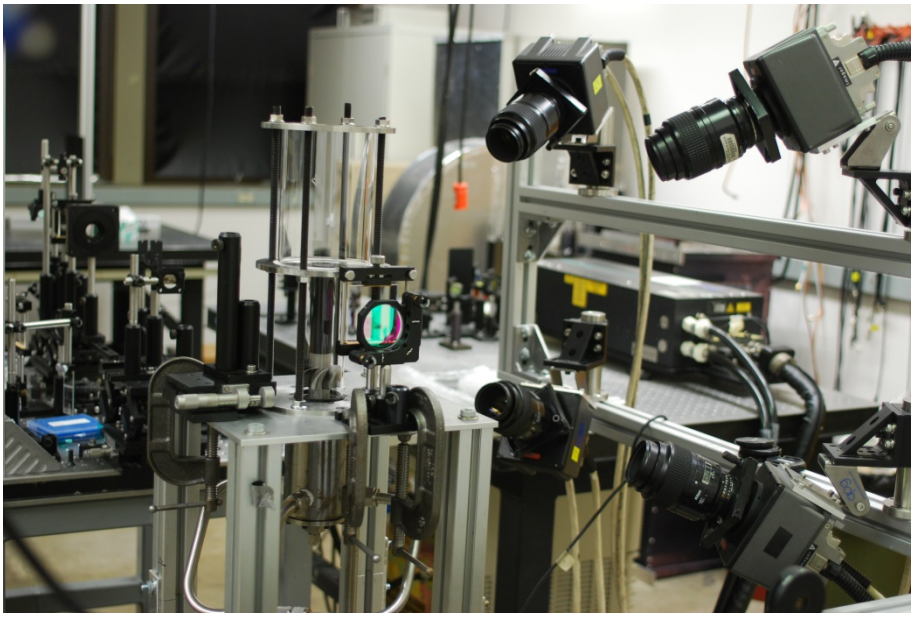

Figure D.1: Model swirl combustor and diagnostic setup for high-speed 3D flame front reconstruction and tomographic PIV.

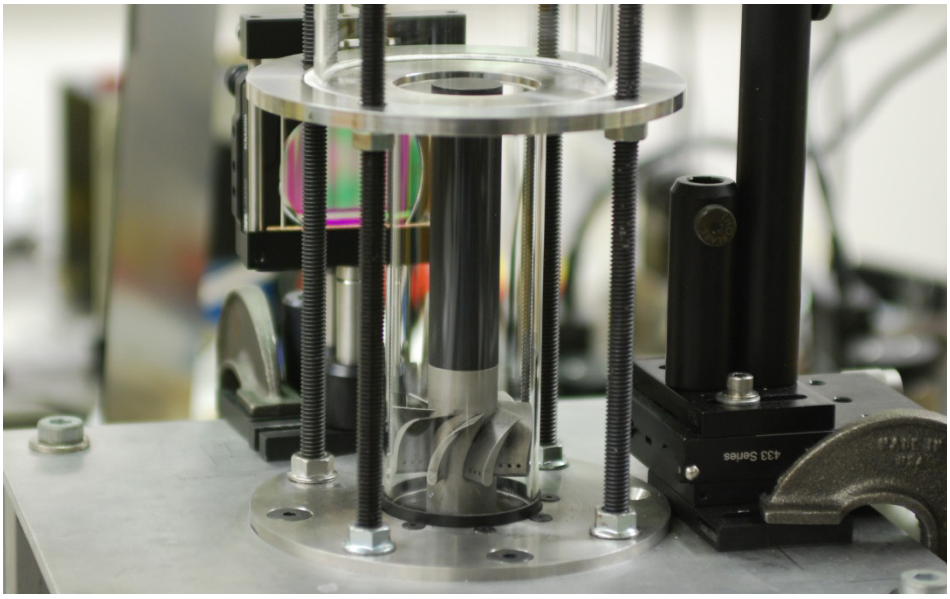

Figure D.2: Mixing tube with axial swirler and attached center body.

Bibliography

[1] S. Taamallah, K. Vogiatzaki, F.M. Alzahrani, E.M.A. Mokheimer, M.A. Habib, A.F. Ghoniem, Fuel flexibility, stability and emissions in premixed hydrogen-rich gas turbine combustion: Technology, fundamentals, and numerical simulations, Appl. Energy. 154 (2015) 1020–1047.

[2] T. Lieuwen, V. McDonell, D. Santavicca, T. Sattelmayer, Burner Development and Operability Issues Associated with Steady Flowing Syngas Fired Combustors, Combust. Sci. Technol. 180 (2008) 1169–1192.

[3] Y. Huang, V. Yang, Dynamics and stability of lean-premixed swirl-stabilized combustion, Prog. Energy Combust. Sci. 35 (2009) 293–364.

[4] C.K. Law, Combustion Physics, 2006.

[5] C.K. Law, C. Sung, Structure, aerodynamics, and geometry of premixed flamelets, Prog. Energy Combust. Sci. 26 (2000) 459–505.

[6] J. Driscoll, Turbulent premixed combustion: Flamelet structure and its effect on turbulent burning velocities, Prog. Energy Combust. Sci. 34 (2008) 91–134.

[7] A.N. Lipatnikov, J. Chomiak, Turbulent flame speed and thickness: Phenomenology, evaluation, and application in multi-dimensional simulations, Prog. Energy Combust. Sci. 28 (2002) 1–74.

[8] A.N. Lipatnikov, J. Chomiak, Molecular transport effects on turbulent flame propagation and structure, Prog. Energy Combust. Sci. 31 (2005) 1–73.

[9] A.N. Lipatnikov, J. Chomiak, Effects of premixed flames on turbulence and turbulent scalar transport, Prog. Energy Combust. Sci. 36 (2010) 1–102.

[10] B. Lewis, G. von Elbe, Stability and structure of burner flames, J. Chem. Phys. 11 (1943) 75–97.

[11] G. von Elbe, M. Mentser, Further Studies of the Structure and Stability of Burner Flames, J. Chem. Phys. 13 (1945) 89.

[12] K. Wohl, Quenching, Flash-Back, Blow-Off - Theory and Experiment, Symp. (Int.) Combust. 4 (1953) 68–89.

[13] L.E. Bollinger, R. Edse, Effect of Burner-Tip Temperature on Flash Back of Turbulent Hydrogen-Oxygen Flames, Ind. Eng. Chem. 48 (1956) 802–807.

[14] B. Fine, Effect of Initial Temperature on Flash Back of Laminar and Turbulent Burner Flames, Ind. Eng. Chem. 51 (1958) 564–566.

[15] L.N. Khitrin, P.B. Moin, D.B. Smirnov, V.U. Shevchuk, Peculiarities of laminar- and turbulent-flame flashbacks, Symp. (Int.) Combust. 10 (1965) 1285–1291.

[16] S.L. Plee, A.M. Mellor, Review of Flashback Reported in Prevaporizing/Premixing Combustors, Combust. Flame. 32 (1978) 193–203.

[17] C. Eichler, G. Baumgartner, T. Sattelmayer, Experimental Investigation of Turbulent Boundary Layer Flashback Limits for Premixed Hydrogen-Air Flames Confined in Ducts, J. Eng. Gas Turbines Power. 134 (2012) 011502.

[18] B. Shaffer, Z. Duan, V. McDonell, Study of Fuel Composition Effects on

Flashback Using a Confined Jet Flame Burner, J. Eng. Gas Turbines Power. 135 (2012) 011502.
[19] Z. Duan, B. Shaffer, V. McDonell, G. Baumgartner, T. Sattelmayer, Influence of Burner Material, Tip Temperature, and Geometrical Flame Configuration on Flashback Propensity of H 2 -Air Jet Flames, J. Eng. Gas Turbines Power. 136 (2013) 021502.
[20] Z. Duan, B. Shaffer, V. McDonell, Study of Fuel Composition, Burner Material, and Tip Temperature Effects on Flashback of Enclosed Jet Flame., J. Eng. Gas Turbines Power. 135 (2013) 121504.
[21] C. Eichler, T. Sattelmayer, Experiments on Flame Flashback in a Quasi-2D Turbulent Wall Boundary Layer for Premixed Methane-Hydrogen-Air Mixtures, J. Eng. Gas Turbines Power. 133 (2011) 011503.
[22] Y.-C. Lin, S. Daniele, P. Jansohn, K. Boulouchos, Turbulent Flame Speed as an Indicator for Flashback Propensity of Hydrogen-Rich Fuel Gases, J. Eng. Gas Turbines Power. 135 (2013) 111503.
[23] V. Kurdyumov, E. Fernández-Tarrazo, J.-M. Truffaut, J. Quinard, A. Wangher, G. Searby, Experimental and numerical study of premixed flame flashback, Proc. Combust. Inst. 31 (2007) 1275–1282.
[24] C. Eichler, T. Sattelmayer, Premixed flame flashback in wall boundary layers studied by long-distance micro-PIV, Exp. Fluids. 52 (2011) 347–360.
[25] A. Gruber, J.H. Chen, D. Valiev, C.K. Law, Direct numerical simulation of premixed flame boundary layer flashback in turbulent channel flow, J. Fluid Mech. 709 (2012) 516–542.
[26] A. Gruber, A.R. Kerstein, D. Valiev, C.K. Law, H. Kolla, J.H. Chen, Modeling of mean flame shape during premixed flame flashback in turbulent boundary layers, Proc. Combust. Inst. 35 (2015) 1485–1492.
[27] M.G. Hall, Vortex Breakdown, Annu. Rev. Fluid Mech. 4 (1972) 195–218.
[28] S. Leibovich, The Structure of Vortex Breakdown, Annu. Rev. Fluid Mech. 10 (1978) 221–246.
[29] M. Escudier, Vortex breakdown: Observations and explanations, Prog. Aerosp. Sci. 25 (1988) 189–229.
[30] O. Lucca-Negro, T. O'Doherty, Vortex breakdown: a review, Prog. Energy Combust. Sci. 27 (2001) 431–481.
[31] J. Fritz, M. Kröner, T. Sattelmayer, Flashback in a Swirl Burner With Cylindrical Premixing Zone, J. Eng. Gas Turbines Power. 126 (2004) 276–283.
[32] M. Kröner, J. Fritz, T. Sattelmayer, Flashback Limits for Combustion Induced Vortex Breakdown in a Swirl Burner, J. Eng. Gas Turbines Power. 125 (2003) 693–700.
[33] M. Kroener, T. Sattelmayer, J. Fritz, F. Kiesewetter, C. Hirsch, Flame Propagation in Swirling Flows—Effect of Local Extinction on the Combustion Induced Vortex Breakdown, Combust. Sci. Technol. 179 (2007) 1385–1416.
[34] Y. Sommerer, D. Galley, T. Poinsot, Large eddy simulation and experimental

study of flashback and blow-off in a lean partially premixed swirled burner, J. Turbul. 5 (2004).
[35] S. Tanimura, M. Komiyama, K. Takeishi, Y. Iwasaki, K. Nakayama, Visualization of flashback in a premixed burner with swirling flow, Sci. China Ser. E Technol. Sci. 53 (2010) 40–45.
[36] G. Blesinger, R. Koch, H.-J. Bauer, Influence of flow field scaling on flashback of swirl flames, Exp. Therm. Fluid Sci. 34 (2010) 290–298.
[37] A. Schönborn, P. Sayad, J. Klingmann, Influence of precessing vortex core on flame flashback in swirling hydrogen flames, Int. J. Hydrogen Energy. 39 (2014) 20233–20241.
[38] E. Tangermann, M. Pfitzner, M. Konle, T. Sattelmayer, Large-Eddy Simulation and Experimental Observation of Combustion-Induced Vortex Breakdown, Combust. Sci. Technol. 182 (2010) 505–516.
[39] C. Mayer, J. Sangl, T. Sattelmayer, Study on the Operational Window of a Swirl Stabilized Syngas Burner Under Atmospheric and High Pressure Conditions, J. Eng. Gas Turbines Power. 134 (2012) 031506.
[40] P. Sayad, A. Schönborn, J. Klingmann, Experimental investigation of the stability limits of premixed syngas-air flames at two moderate swirl numbers, Combust. Flame. 164 (2015) 270–282.
[41] M. Konle, F. Kiesewetter, T. Sattelmayer, Simultaneous high repetition rate PIV–LIF-measurements of CIVB driven flashback, Exp. Fluids. 44 (2008) 529–538.
[42] M. Konle, T. Sattelmayer, Interaction of heat release and vortex breakdown during flame flashback driven by combustion induced vortex breakdown, Exp. Fluids. 47 (2009) 627–635.
[43] F. Kiesewetter, M. Konle, T. Sattelmayer, Analysis of Combustion Induced Vortex Breakdown Driven Flame Flashback in a Premix Burner With Cylindrical Mixing Zone, J. Eng. Gas Turbines Power. 129 (2007) 929–936.
[44] M. Konle, T. Sattelmayer, Time Scale Model for the Prediction of the Onset of Flame Flashback Driven by Combustion Induced Vortex Breakdown, J. Eng. Gas Turbines Power. 132 (2010) 041503.
[45] W.T. Ashurst, Flame Propagation Along a Vortex: the Baroclinic Push, Combust. Sci. Technol. 112 (1996) 175–185.
[46] S. Ishizuka, Flame propagation along a vortex axis, Prog. Energy Combust. Sci. 28 (2002) 477–542.
[47] A. Nauert, P. Petersson, M. Linne, A. Dreizler, Experimental analysis of flashback in lean premixed swirling flames: conditions close to flashback, Exp. Fluids. 43 (2007) 89–100.
[48] C. Heeger, R.L. Gordon, M.J. Tummers, T. Sattelmayer, A. Dreizler, Experimental analysis of flashback in lean premixed swirling flames: upstream flame propagation, Exp. Fluids. 49 (2010) 853–863.
[49] B. Dam, G. Corona, M. Hayder, A. Choudhuri, Effects of syngas composition on combustion induced vortex breakdown (CIVB) flashback in a swirl stabilized

combustor, Fuel. 90 (2011) 3274–3284.
[50] A. De, S. Acharya, Parametric study of upstream flame propagation in hydrogen-enriched premixed combustion: Effects of swirl, geometry and premixedness, Int. J. Hydrogen Energy. 37 (2012) 14649–14668.
[51] N. Karimi, C. Heeger, L. Christodoulou, A. Dreizler, Experimental and Theoretical Investigation of the Flashback of a Swirling, Bluff-Body Stabilised, Premixed Flame, Zeitschrift Für Phys. Chemie. 229 (2015) 663–689.
[52] T. Sattelmayer, C. Mayer, J. Sangl, Interaction of Flame Flashback Mechanisms in Premixed Hydrogen-Air Swirl Flames, J. Eng. Gas Turbines Power. 138 (2014) 1–13.
[53] X. Tian, S. Xing, Y. Cui, A. Fang, C. Nie, CIVB flashback analysis of hydrogen flame based on azimuthal vorticity at mixing zone exit, Sci. China Technol. Sci. 57 (2014) 2466–2474.
[54] D.R. Noble, Q. Zhang, A. Shareef, J. Tootle, A. Meyers, T. Lieuwen, Syngas Mixture Composition Effects upon Flashback and Blowout, in: Proc. GT2006 ASME Turbo Expo 2006 Power Land, Sea Air, Barcelona, Spain, 2006.
[55] N. Karimi, S. McGrath, P. Brown, J. Weinkauff, A. Dreizler, Generation of Adverse Pressure Gradient in the Circumferential Flashback of a Premixed Flame, Flow, Turbul. Combust. (2016).
[56] C. Lietz, M. Hassanaly, V. Raman, Large Eddy Simulation of Flame Flashback in Swirling Premixed CH4/H2-Air Flames, in: 53rd AIAA Aerosp. Sci. Meet., 2015: pp. 17–20.
[57] A.M. Steinberg, J.F. Driscoll, S.L. Ceccio, Three-dimensional temporally resolved measurements of turbulence-flame interactions using orthogonal-plane cinema-stereoscopic PIV, Exp. Fluids. 47 (2009) 527–547.
[58] J. Kerl, C. Lawn, F. Beyrau, Three-dimensional flame displacement speed and flame front curvature measurements using quad-plane PIV, Combust. Flame. 160 (2013) 2757–2769.
[59] P.J. Trunk, I. Boxx, C. Heeger, W. Meier, B. Böhm, A. Dreizler, Premixed flame propagation in turbulent flow by means of stereoscopic PIV and dual-plane OH-PLIF at sustained kHz repetition rates, Proc. Combust. Inst. 34 (2013) 3565–3572.
[60] M. Gamba, N.T. Clemens, O. a Ezekoye, Volumetric PIV and 2D OH PLIF imaging in the far-field of a low Reynolds number nonpremixed jet flame, Meas. Sci. Technol. 24 (2013) 024003.
[61] B. Yip, R.L. Schmitt, M.B. Long, Instantaneous three-dimensional concentration measurements in turbulent jets and flames., Opt. Lett. 13 (1988) 96.
[62] B.S. Thurow, K.P. Lynch, Development of a High-Speed Three-Dimensional Flow Visualization Technique, AIAA J. 47 (2009) 2857–2865.
[63] R. Wellander, M. Richter, M. Aldén, Time resolved, 3D imaging (4D) of two phase flow at a repetition rate of 1 kHz, Opt. Express. 19 (2011) 21508.
[64] J. Weinkauff, M. Greifenstein, A. Dreizler, B. Böhm, Time resolved three-dimensional flamebase imaging of a lifted jet flame by laser scanning, Meas. Sci.

Technol. 26 (2015) 105201.
[65] M.L. Greene, V. Sick, Volume-resolved flame chemiluminescence and laser-induced fluorescence imaging, Appl. Phys. B Lasers Opt. 113 (2013) 87–92.
[66] W.B. Ng, Y. Zhang, Stereoscopic imaging and reconstruction of the 3D geometry of flame surfaces, Exp. Fluids. 34 (2003) 484–493.
[67] K.Y. Cheung, Y. Zhang, Stereo imaging and analysis of a combustion process in a gas turbine combustor, Meas. Sci. Technol. 17 (2006) 3221–3228.
[68] J. Floyd, P. Geipel, A.M. Kempf, Computed Tomography of Chemiluminescence (CTC): Instantaneous 3D measurements and Phantom studies of a turbulent opposed jet flame, Combust. Flame. 158 (2011) 376–391.
[69] J.P. Moeck, J.-F. Bourgouin, D. Durox, T. Schuller, S. Candel, Tomographic reconstruction of heat release rate perturbations induced by helical modes in turbulent swirl flames, Exp. Fluids. 54 (2013) 1498.
[70] N. a Worth, J.R. Dawson, Tomographic reconstruction of OH* chemiluminescence in two interacting turbulent flames, Meas. Sci. Technol. 24 (2013) 024013.
[71] J. Weinkauff, D. Michaelis, A. Dreizler, B. Böhm, Tomographic PIV measurements in a turbulent lifted jet flame, Exp. Fluids. 54 (2013) 1624.
[72] X. Li, L. Ma, Volumetric imaging of turbulent reactive flows at kHz based on computed tomography., Opt. Express. 22 (2014) 4768–78.
[73] X. Li, L. Ma, Capabilities and limitations of 3D flame measurements based on computed tomography of chemiluminescence, Combust. Flame. 162 (2015) 642–651.
[74] W. Xu, A.J. Wickersham, Y. Wu, F. He, L. Ma, 3D flame topography obtained by tomographic chemiluminescence with direct comparison to planar Mie scattering measurements, Appl. Opt. 54 (2015) 2174–2182.
[75] K.R. Gosselin, M.W. Renfro, Reconstruction of three-dimensional chemiluminescence images with a maximum entropy deconvolution algorithm., Appl. Opt. 51 (2012) 1671–80.
[76] J. Weinkauff, J. Köser, D. Michaelis, B. Peterson, A. Dreizler, B. Böhm, Volumetric flame measurements in a lifted turbulent jet flame using tomographic reconstruction of chemiluminescence, in: 17th Int. Symp. Appl. Laser Tech. to Fluid Mech., 2014.
[77] T.D. Upton, D.D. Verhoeven, D.E. Hudgins, High-resolution computed tomography of a turbulent reacting flow, Exp. Fluids. 50 (2011) 125–134.
[78] L. Boyer, Laser Tomographic Method for Flame Front Movement Studies, Combust. Flame. 39 (1980) 321–323.
[79] P.C. Miles, F.C. Gouldin, Simultaneous measurements of flamelet position and gas velocity in premixed turbulent flames, in: Proc. 1987 ASME-JSME Therm. Eng. Jt. Conf., 1987: pp. 187–193.
[80] P.C. Miles, F.C. Gouldin, Mean Reaction Rates and Flamelet Statistics for Reaction Rate Modeling in Premixed Turbulent Flames, Proc. Combust. Inst. 24 (1992) 477.

[81] P.C. Miles, F.C. Gouldin, Premixed Turbulent Flame/Flow Interaction: Simultaneous Measurements of Velocity and Flamelet Position, AIAA J. 36 (1998) 1178–1189.
[82] I. Shepherd, E. Bourguignon, Y. Michou, I. Gökalp, The burning rate in turbulent Bunsen flames, Symp. (Int.) Combust. 27 (1998) 909–916.
[83] B. Renou, A. Boukhalfa, D. Puechberty, M. Trinite, Local scalar flame properties of freely propagating premixed turbulent flames at various Lewis numbers, Combust. Flame. 123 (2000) 507–521.
[84] D.A. Knaus, F.C. Gouldin, Measurements of flamelet orientations in premixed flames with positive and negative markstein numbers, Proc. Combust. Inst. 28 (2000) 367–373.
[85] P. Gopalakrishnan, M.K. Bobba, J.M. Seitzman, Controlling mechanisms for low NOx emissions in a non-premixed stagnation point reverse flow combustor, Proc. Combust. Inst. 31 (2007) 3401–3408.
[86] G. Coppola, B. Coriton, A. Gomez, Highly turbulent counterflow flames: A laboratory scale benchmark for practical systems, Combust. Flame. 156 (2009) 1834–1843.
[87] C. Cohé, C. Chauveau, I. Gökalp, D.F. Kurtuluş, CO2 addition and pressure effects on laminar and turbulent lean premixed CH4 air flames, Proc. Combust. Inst. 32 (2009) 1803–1810.
[88] S. Balusamy, A. Cessou, B. Lecordier, Direct measurement of local instantaneous laminar burning velocity by a new PIV algorithm, Exp. Fluids. 50 (2010) 1109–1121.
[89] S. Kheirkhah, Ö.L. Gülder, Turbulent premixed combustion in V-shaped flames: Characteristics of flame front, Phys. Fluids. 25 (2013) 1–24.
[90] P. Tamadonfar, Ö.L. Gülder, Effects of mixture composition and turbulence intensity on flame front structure and burning velocities of premixed turbulent hydrocarbon / air Bunsen flames, Combust. Flame. 162 (2015) 4417–4441.
[91] A. Upatnieks, J.F. Driscoll, C.C. Rasmussen, S.L. Ceccio, Liftoff of turbulent jet flames - Assessment of edge flame and other concepts using cinema-PIV, Combust. Flame. 138 (2004) 259–272.
[92] A.M. Steinberg, J.F. Driscoll, S.L. Ceccio, Measurements of turbulent premixed flame dynamics using cinema stereoscopic PIV, Exp. Fluids. 44 (2008) 985–999.
[93] S. Pfadler, F. Beyrau, A. Leipertz, Flame front detection and characterization using conditioned particle image velocimetry (CPIV), Opt. Express. 15 (2007) 15444–15456.
[94] B. Fond, C. Abram, A.L. Heyes, A.M. Kempf, F. Beyrau, Simultaneous temperature, mixture fraction and velocity imaging in turbulent flows using thermographic phosphor tracer particles., Opt. Express. 20 (2012) 22118–33.
[95] C. Abram, B. Fond, A.L. Heyes, F. Beyrau, High-speed planar thermometry and velocimetry using thermographic phosphor particles, Appl. Phys. B. 111 (2013) 155–160.

[96] B. Fond, C. Abram, F. Beyrau, On the characterisation of tracer particles for thermographic particle image velocimetry, Appl. Phys. B. 118 (2015) 393–399.
[97] G.E. Elsinga, F. Scarano, B. Wieneke, B.W. Oudheusden, Tomographic particle image velocimetry, Exp. Fluids. 41 (2006) 933–947.
[98] F. Scarano, Tomographic PIV: principles and practice, Meas. Sci. Technol. 24 (2013) 012001.
[99] B. Lecordier, C. Gobin, C. Lacour, A. Cessou, B. Tremblais, L. Thomas, et al., Tomographic PIV study of lifted flames in turbulent Axisymmetric jets of methane ., in: 16th Int. Symp. Appl. Laser Tech. to Fluid Mech., 2012.
[100] B. Coriton, A.M. Steinberg, J.H. Frank, High-speed tomographic PIV and OH PLIF measurements in turbulent reactive flows, Exp. Fluids. 55 (2014) 1743.
[101] B. Coriton, J.H. Frank, High-speed tomographic PIV measurements of strain rate intermittency and clustering in turbulent partially-premixed jet flames, Proc. Combust. Inst. 35 (2014) 1243–1250.
[102] I. Boxx, C.D. Carter, W. Meier, On the feasibility of tomographic-PIV with low pulse energy illumination in a lifted turbulent jet flame, Exp. Fluids. 55 (2014).
[103] E. Baum, B. Peterson, C. Surmann, D. Michaelis, B. Böhm, A. Dreizler, Investigation of the 3D flow field in an IC engine using tomographic PIV, Proc. Combust. Inst. 34 (2013) 2903–2910.
[104] M.P. Tokarev, D.K. Sharaborin, a S. Lobasov, L.M. Chikishev, V.M. Dulin, D.M. Markovich, 3D velocity measurements in a premixed flame by tomographic PIV, Meas. Sci. Technol. 26 (2015) 064001.
[105] P. Petersson, M. Gesnik, J. Olofsson, V. Jaunet, M. Aldén, Volumetric velocimetry in lifted turbulent premixed low-swirl flames, in: 6th Eur. Combust. Meet., 2013.
[106] B.W. van Oudheusden, PIV-based pressure measurement, Meas. Sci. Technol. 24 (2013) 032001.
[107] A. Schröder, R. Geisler, G.E. Elsinga, F. Scarano, U. Dierksheide, Investigation of a turbulent spot and a tripped turbulent boundary layer flow using time-resolved tomographic PIV, Exp. Fluids. 44 (2008) 305–316.
[108] G.E. Elsinga, I. Marusic, Evolution and lifetimes of flow topology in a turbulent boundary layer, Phys. Fluids. 22 (2010) 1–8.
[109] A. Schröder, R. Geisler, K. Staack, G.E. Elsinga, F. Scarano, B. Wieneke, et al., Eulerian and Lagrangian views of a turbulent boundary layer flow using time-resolved tomographic PIV, Exp. Fluids. 50 (2010) 1071–1091.
[110] G.E. Elsinga, C. Poelma, A. Schröder, R. Geisler, F. Scarano, J. Westerweel, Tracking of vortices in a turbulent boundary layer, J. Fluid Mech. 697 (2012) 273–295.
[111] M. Novara, K.J. Batenburg, F. Scarano, Motion tracking-enhanced MART for tomographic PIV, Meas. Sci. Technol. 21 (2010) 035401.
[112] D. Adhikari, E.K. Longmire, Visual hull method for tomographic PIV measurement of flow around moving objects, Exp. Fluids. 53 (2012) 943–964.
[113] Y.J. Jeon, H.J. Sung, Three-dimensional PIV measurement of flow around an

arbitrarily moving body, Exp. Fluids. 53 (2012) 1057–1071.
[114] S. Im, Y.J. Jeon, H.J. Sung, Tomo-PIV measurement of flow around an arbitrarily moving body with surface reconstruction, Exp. Fluids. 56 (2015).
[115] D. Ebi, N.T. Clemens, Time-resolved PIV and flame front imaging of boundary layer flashback in a swirl combustor, in: 17th Int. Symp. Appl. Laser Tech. to Fluid Mech., 2014.
[116] M. Gamba, Volumetric PIV and OH PLIF Imaging in the Far Field of Nonpremixed Jet Flames, The University of Texas at Austin, 2009.
[117] B. Wieneke, Stereo-PIV using self-calibration on particle images, Exp. Fluids. 39 (2005) 267–280.
[118] B. Wieneke, PIV uncertainty quantification from correlation statistics, Meas. Sci. Technol. 26 (2015) 074002.
[119] A. Sciacchitano, D.R. Neal, B.L. Smith, S.O. Warner, P.P. Vlachos, B. Wieneke, et al., Collaborative framework for PIV uncertainty quantification : comparative assessment of methods, (2014) 7–10.
[120] J. Westerweel, Fundamentals of digital particle image velocimetry, Meas. Sci. Technol. 8 (1997) 1379–1392.
[121] K.T. Christensen, The influence of peak-locking errors on turbulence statistics computed from PIV ensembles, Exp. Fluids. 36 (2004) 484–497.
[122] C.J. Sung, C.K. Law, R. L Axelbaum, Thermophoretic Effects on Seeding Particles in LDV Measurements of Flames, Combust. Sci. Technol. 99 (1994) 119–132.
[123] B. Böhm, D. Geyer, A. Dreizler, K.K. Venkatesan, N.M. Laurendeau, M.W. Renfro, Simultaneous PIV/PTV/OH PLIF imaging: Conditional flow field statistics in partially premixed turbulent opposed jet flames, Proc. Combust. Inst. 31 (2007) 709–717.
[124] A. Stella, G. Guj, J. Kompenhans, M. Raffel, H. Richard, Application of particle image velocimetry to combusting flows: design considerations and uncertainty assessment, Exp. Fluids. 30 (2001) 167–180.
[125] S.H. Starner, R.W. Bilger, R.W. Dibble, R.S. Barlow, D.C. Fourguette, M.B. Long, Joint Planar CH and OH LIF Imaging in Piloted Turbulent Jet Diffusion Flames Near Extinction, Symp. (Int.) Combust. 24 (1992) 341–349.
[126] P.H. Paul, H.N. Najm, Planar laser-induced fluorescence imaging of flame heat release rate, Symp. (Int.) Combust. 27 (1998) 43–50.
[127] T. Chew, R. Britter, K. Bray, Laser tomography of turbulent premixed bunsen flames, Combust. Flame. 75 (1989) 165–174.
[128] L.W. Kostiuk, I.G. Shepherd, K.N.C. Bray, Experimental Study of Premixed Turbulent Combustion in Opposed Streams. Part III - Spatial Structure of Flames, Combust. Flame. 118 (1999) 129–139.
[129] G. Amantini, J.H. Frank, A. Gomez, H.G. Im, S. Aggarwal, J.H. Chen, Experiments on standing and traveling edge flames around flame holes, Proc. Combust. Inst. 30 (2005) 313–321.

[130] F. Halter, C. Chauveau, I. Gökalp, D. Veynante, Analysis of flame surface density measurements in turbulent premixed combustion, Combust. Flame. 156 (2009) 657–664.
[131] A. Marshall, J. Lundrigan, P. Venkateswaran, J. Seitzman, T. Lieuwen, Fuel effects on leading point curvature statistics of high hydrogen content fuels, Proc. Combust. Inst. 35 (2015) 1417–1424.
[132] T. Lachaux, F. Halter, C. Chauveau, I. Gökalp, I.G. Shepherd, H. Kobayashi, et al., Flame front analysis of high-pressure turbulent lean premixed methane-air flames, Proc. Combust. Inst. 30 (2005) 819–826.
[133] D. Ebi, N.T. Clemens, Simultaneous high-speed 3D flame front detection and tomographic PIV, Meas. Sci. Technol. 27 (2016) 035303.
[134] B. Wieneke, Volume self-calibration for 3D particle image velocimetry, Exp. Fluids. 45 (2008) 549–556.
[135] C. Atkinson, J. Soria, An efficient simultaneous reconstruction technique for tomographic particle image velocimetry, Exp. Fluids. 47 (2009) 553–568.
[136] K.P. Lynch, F. Scarano, Experimental determination of tomographic PIV accuracy by a 12-camera system, Meas. Sci. Technol. 25 (2014) 084003.
[137] M. Novara, F. Scarano, Performances of motion tracking enhanced Tomo-PIV on turbulent shear flows, Exp. Fluids. 52 (2011) 1027–1041.
[138] K.P. Lynch, F. Scarano, An efficient and accurate approach to MTE-MART for time-resolved tomographic PIV, Exp. Fluids. 56 (2015) 1–16.
[139] G.E. Elsinga, S. Tokgoz, Ghost hunting—an assessment of ghost particle detection and removal methods for tomographic-PIV, Meas. Sci. Technol. 25 (2014) 084004.
[140] J. Westerweel, F. Scarano, Universal outlier detection for PIV data, Exp. Fluids. 39 (2005) 1096–1100.
[141] Ö.L. Gülder, G.J. Smallwood, R. Wong, D.R. Snelling, R. Smith, B.M. Descamps, et al., Flame front surface characteristics in turbulent premixed propane air combustion, Combust. Flame. 120 (2000) 407–416.
[142] K. Christensen, R. Adrian, Measurement of instantaneous Eulerian acceleration fields by particle image accelerometry: method and accuracy, Exp. Fluids. 33 (2002) 759–769.
[143] D. Ebi, N.T. Clemens, Experimental investigation of upstream flame propagation during boundary layer flashback of swirl flames, Combust. Flame. *(in press)*.
[144] N. Syred, A review of oscillation mechanisms and the role of the precessing vortex core (PVC) in swirl combustion systems, Prog. Energy Combust. Sci. 32 (2006) 93–161.
[145] K. Oberleithner, M. Stöhr, S.H. Im, C.M. Arndt, A.M. Steinberg, Formation and flame-induced suppression of the precessing vortex core in a swirl combustor: Experiments and linear stability analysis, Combust. Flame. 162 (2015) 3100–3114.
[146] F. Martinelli, A. Olivani, A. Coghe, Experimental analysis of the precessing vortex core in a free swirling jet, Exp. Fluids. 42 (2007) 827–839.

[147] K. Oberleithner, S. Terhaar, L. Rukes, C. Oliver Paschereit, Why Nonuniform Density Suppresses the Precessing Vortex Core, J. Eng. Gas Turbines Power. 135 (2013) 121506.
[148] M. Bellenoue, T. Kageyama, S. a. Labuda, J. Sotton, Direct measurement of laminar flame quenching distance in a closed vessel, Exp. Therm. Fluid Sci. 27 (2003) 323–331.
[149] J. Sotton, B. Boust, S.A. Labuda, M. Bellenoue, Head-on Quenching of Transient Laminar Flame: Heat Flux and Quenching Distance Measurements, Combust. Sci. Technol. 177 (2005) 1305–1322.
[150] M. Mann, C. Jainski, M. Euler, B. Böhm, A. Dreizler, Transient flame–wall interactions: Experimental analysis using spectroscopic temperature and CO concentration measurements, Combust. Flame. 161 (2014) 2371–2386.
[151] A.P. Kelley, C.K. Law, Nonlinear effects in the extraction of laminar flame speeds from expanding spherical flames, Combust. Flame. 156 (2009) 1844–1851.
[152] T. Lieuwen, Unsteady Combustor Physics, 2013.
[153] D. Beerer, V. McDonell, P. Therkelsen, R.K. Cheng, Flashback and Turbulent Flame Speed Measurements in Hydrogen/Methane Flames Stabilized by a Low-Swirl Injector at Elevated Pressures and Temperatures, J. Eng. Gas Turbines Power. 136 (2013) 031502.
[154] N. Syred, M. Abdulsada, A. Griffiths, T. O'Doherty, P. Bowen, The effect of hydrogen containing fuel blends upon flashback in swirl burners, Appl. Energy. 89 (2012) 106–110.
[155] M. Fukuda, K. Korematsu, M. Sakamoto, On Quenching Distance of Mixtures of Methane and Hydrogen with Air, Bull. JSME. 24 (1981) 1192–1197.
[156] M. Mann, C. Jainski, M. Euler, B. Böhm, A. Dreizler, Transient flame–wall interactions: Experimental analysis using spectroscopic temperature and CO concentration measurements, Combust. Flame. 161 (2014) 2371–2386.
[157] B. Boust, J. Sotton, S. a. Labuda, M. Bellenoue, A thermal formulation for single-wall quenching of transient laminar flames, Combust. Flame. 149 (2007) 286–294.
[158] Z. Liu, N. Il Kim, An assembled annular stepwise diverging tube for the measurement of laminar burning velocity and quenching distance, Combust. Flame. 161 (2014) 1499–1506.
[159] Y. Jung, M.J. Lee, N. Il Kim, Direct prediction of laminar burning velocity and quenching distance of hydrogen-air flames using an annular stepwise diverging tube (ASDT), Combust. Flame. 164 (2015) 397–399.
[160] D. Schanz, A. Schröder, S. Gesemann, D. Michaelis, B. Wieneke, " Shake The Box ": A highly efficient and accurate Tomographic Particle Tracking Velocimetry (TOMO-PTV) method using prediction of particle positions, in: 10th Int. Symp. Part. Image Velocim., 2013.
[161] D. Schanz, A. Schröder, S. Gesemann, " Shake The Box " - a 4D PTV algorithm : Accurate and ghostless reconstruction of Lagrangian tracks in densely seeded flows, in: 17th Int. Symp. Appl. Laser Tech. to Fluid Mech., 2014.

[162] S.S. Shy, Y.C. Chen, C.H. Yang, C.C. Liu, C.M. Huang, Effects of H2 or CO2 addition, equivalence ratio, and turbulent straining on turbulent burning velocities for lean premixed methane combustion, Combust. Flame. 153 (2008) 510–524.